PICOSECOND STUDIES OF THE VIBRATIONAL PREDISSOCIATION OF VAN DER WAALS COMPLEXES

Thesis by

David Haynes Semmes

In Partial Fulfillment of the Requirements

for the Degree of

Doctor of Philosophy

California Institute of Technology

Pasadena, California

1990

(Submitted September 27, 1989)

Acknowledgments

My stay here at Caltech hasn't been as much fun as I'd hoped, but from my point of view it certainly has been productive. I feel that I've matured personally and professionally because of my stay here and I'd like to thank my thesis advisor, Ahmed Zewail, for his help and encouragement.

I'd particularly like to acknowledge my old boss and great friend, Dr. A. R. Ravishankara. Ravi is the one who made science come alive for me and who inspired me to acomplish what I have done here. In addition to all that, he's been a wonderful friend, advisor, and confidant ever since.

I have been very fortunate to share the lab with Spencer Baskin these past years. Spencer has always been patient, friendly, and helpful. Without him, graduate school would have been much more difficult for me.

I'd also like to thank my friends, Bob Smith, Jack Duggan, and Bill Wilson. Without them, finishing graduate school might have been impossible.

Finally, I'd like to thank all my friends at Caltech, expecially in the sub-basement, and all my friends in Pasadena who have shared so much with me these past six years.

The work in this thesis has been made possible through the support of the National Science Foundation in the form of a predoctoral fellowship and in the form of research grants.

Abstract

The vibrational predissociation of several van der Waals complexes of aromatic molecules with rare gas atoms, isolated in a free-jet molecular beam expansion, has been studied using time-resolved spectroscopy. Direct measurements have been made, on a picosecond time scale, of the fluorescence intensity from the initially excited single vibrational level and from the various final vibrational states formed in the dissociation of the complexes. The time-resolved data is analyzed with the aid of different kinetic models and can distinguish between parallel decay paths, sequential paths with intramolecular vibrational redistribution (IVR) preceding vibrational predissociation, and sequential paths with reversible IVR preceding vibrational predissociation. The contribution of the van der Waals modes to the total vibrational state density induces dissipative IVR in the complexes at much lower energies than in the bare aromatic molecule. The measured predissociation rates are compared with rates calculated according to the statistical RRKM theory of unimolecular reactions. Some of the experimental results show mode-selective behavior, while other results suggest statistical behavior.

TABLE OF CONTENTS

Chapter One

Introduction

The intensity, coherence, spectral purity, and short pulse widths of modern lasers have stimulated interest in using these optical properties of lasers to try to induce vibrationally mode specific chemistry in isolated molecules. By selectively exciting particular vibrational motions in a molecule or molecular complex, it may be possible to observe unimolecular dissociation which depends on the dynamics of that particular vibration rather than simply the energy.

Van der Waals complexes have been used as prototypical systems for studying the energy and mode dependence of unimolecular dissociations since it was first demonstrated[1] that the complexes could be easily "synthesized" and characterized in a molecular beam expansion. These complexes are attractive prototypes for studying the details of unimolecular dissociation because van der Waals bonds are weak compared to chemical bonds, and the van der Waals bond is therefore a relatively small perturbation on the system. Since the bond energy is low, the dissociation can be studied in relatively well-characterized regions of the potential energy surface where the energy level structure of the chemical part (as opposed to the van der Waals part) of the complex is relatively sparse and regular, uncomplicated by large anharmonicities and Coriolis couplings. Furthermore, because the binding is through a single, weak van der Waals bond, it is expected that specific dynamical interactions in these complexes may cause the dissociation to be mode-specific. Because of the apparent simplicity of the potential energy surface of these complexes, a tractable theoretical treatment of the dynamics of such systems has been formulated to predict the mode-specific vibrational predissociation rates for these systems (the momentum-gap law[2]). Physically, this law states that the rate is slow when large amounts of internal energy in the complex must be transformed into relative translational energy in the dissociated fragments.

More pragmatically, these complexes are attractive candidates for the study of unimolecular dissociation because vibrations of the complex above the dissociation limit are generally well-characterized and are allowed and intense compared with methods of exciting chemically bound systems, for example, exciting local mode vibrations.

Many spectroscopic studies of van der Waals systems have been carried out since Smalley's seminal work.[1] Considerable progress has been made in the study of the complexes of small molecules, particularly from high resolution infrared spectroscopy.[3] In addition to the structural information that is available from such work, the lifetime can be measured if the homogeneous linewidth of an individual rovibrational transition is resolved. From these experiments, the dynamics of the complexes of many systems of small molecules have been studied and understood according to the momentum-gap law or because of specific dynamical interactions. For example, the lifetime of the complex H_2-HF is 27 ns[3c] (from the measured linewidth) while the lifetime of the complex Ar-HF is less than 0.3 msec[3d] (from time-of-flight measurements). This is understood by observing that a large fraction of the excess energy in the H_2-HF complex can go into rotation if the fragments rotate in opposite senses, while conservation of angular momentum limits the amount of energy that can be deposited into the rotation of the products of the dissociation of Ar-HF. Therefore, a large energy must go into relative translation and the rate is relatively slow according to the momentum-gap law.

Mode-selective lifetimes, lifetimes which depend on the actual vibrational dynamics rather than the ability of the system to dispose of internal energy, have also been observed for complexes of small molecules. The first observation of such a mode-specific lifetime was the measurement of the linewidths of the HF

dimer.[4] The width of the 'internal,' hydrogen bonded HF stretch corresponds to a decay lifetime of 1 ns, compared to 24 ns when the 'free' HF stretch is excited.

The study of the vibrational predissociation of complexes of polyatomic molecules, however, is more difficult. Several complexes of aromatic molecules with rare gas atoms have been studied in the first electronic singlet state. Monitoring the predissociation in an excited electronic state is experimentally advantageous because of the availability of high powered, tunable ultraviolet/visible lasers and because of the sensitivity of fluorescence detection in that region of the spectrum.

Rotational constants for the complexes with aromatic molecules are substantially smaller for these systems and rovibrational resolution is the exception rather than the rule for these larger systems. The geometry of a few aromatic molecule-rare gas complexes have been deduced from rotationally resolved excitation spectra and from rotational coherence experiments.[5] In general, the observations indicate that the rare gas atom is bound $\sim$ 3Å above and below the phenyl rings in both the ground and excited electronic states.

Excitation spectra with only vibrational resolution are more common for these systems.[6] In general, these spectra show resolved bands for each of the vibrations of the molecule in the complex, separated from the corresponding transition in the bare molecule by a few wavenumbers. Low frequency bands assigned to the van der Waals modes are weak when observed and have similar magnitudes in both fluorescence and excitation spectra. Thus, the presence of the rare gas atom is a weak perturbation on the spectrum of the aromatic molecule, and the potential energy surface for the rare gas atom is virtually identical in the two electronic states.

Most of the information on the vibrational predissociation dynamics of these

large complexes comes from experiments in which the fluorescence spectra of various excited levels of the complex are measured.[7] In general, emission is observed from the level of the complex that is initially excited, from levels in the complex reached by intramolecular vibrational redistribution, and from levels of the bare aromatic molecule formed in the dissociation. If the lifetime of the bare molecule is known and a decay scheme is assumed, then rates for the different processes may be calculated from the intensities of the assigned emission bands. In this way, assuming that intramolecular vibrational redistribution and vibrational predissociation each occur only from the initially excited state, vibrational predissociation rates of $\sim$1 ns^{-1} have been calculated for s-tetrazine-argon,[7a] p-difluorobenzene-argon,[7b] and benzene[7c] and deutrobenzene[7d] complexes with helium, neon, and argon. In each of these cases the dynamics leading to the observed vibrational product state distributions is not well understood. The vibrational levels that are excited in the dissociated molecule are only a small subset of those that are energetically accessible in each of those cases. Although the dissociation pathways are very selective, they do not appear to follow momentum or energy-gap propensities, and there is no similarity to collision induced pathways for vibrational relaxation.

To understand the dynamics of these simple unimolecular dissociations more completely, it is important to directly time resolve the disappearance of the initially excited state and the formation of the various product states. In that way, not only are the rates accurately measured, but information on the dynamics leading to the formation of product is available, as will be discussed. It is important to note that such information is not available from measured linewidths. While linewidths, in principle, reflect the population decay rate, they contain no information on intermediate states which may precede the formation of the

final product. Furthermore, while linewidth measurements may be appropriate for high resolution studies of the complexes of small molecules where the total density of states is small compared to the laser bandwidth, it is doubtful that linewidth measurements are accurate for larger complexes where inhomogeneous broadening due to unresolved structure can broaden the width of an experimental transition substantially.

Some recent work on the dissociation of van der Waals complexes has concentrated on direct, time-resolved measurements of the population of initial and final states. Mitchell *et al.*[8a] measured an upper limit of 10 ns for the lifetime of ethylene dimers excited to the $\nu_7 = 1$ level. Jacobson[8b] *et al.* have measured decay rates of several nanoseconds from several excited vibrational levels of p-difluorobenzene-argon using a nanosecond laser. Topp[8c] and coworkers have studied perylene complexes, drawing some conclusions about the effect of the binding of the rare gas on the intersystem crossing rate. Rettschnick and coworkers[8d] have measured intramolecular vibrational redistribution and vibrational predissociation rates from three initial levels in the tetrazine-argon complex, showing the precise redistribution pathways which precede vibrational predissociation in this system.

In Chapter Two the experimental apparatus is described. In Chapter Three the kinetic models which are used to model time resolved data are discussed, along with considerations of how clearly they can be distinguished and how accurately rates can be measured. Particular attention is given to the ability to accurately measure the initial, fast rises and decays in the time-resolved data. Chapter Four is a report of experimental data on time-resolved measurements of the dissociation of complexes of stilbene with helium, neon, and argon. The measured rates are discussed and compared with theoretical models. In Chapter

Five similar work on the complex of anthracene with argon is discussed. In the final chapter, the conclusions of this work are summarized.

REFERENCES

1. R. E. Smalley, D. H. Levy, and L. Wharton, J. Chem. Phys. **64**, 3266 (1976).

2. G. E. Ewing, J. Phys. Chem. **90**, 1790 (1986).

3. (a) R. E. Miller, J. Phys. Chem. **90**, 3301 (1986);
   (b) R. E. Miller, Science **240**, 447 (1988);
   (c) K. W. Jucks and R. E. Miller, J. Chem. Phys. **87**, 5629 (1987);
   (d) Z. S. Huang, K. W. Jucks, and R. E. Miller, J. Chem. Phys. **85**, 6905 (1986).

4. (a) A. S. Pine and W. J. Lafferty, J. Chem. Phys. **78**, 2154 (1983);
   (b) Z. S. Huang, K. W. Jucks, and R. E. Miller, J. Chem. Phys. **85**, 3338 (1986).

5. (a) S. M. Beck, M. G. Liverman, D. L. Monts, and R. E. Smalley, J. Chem. Phys. **70**, 232 (1979);
   (b) W. M. van Herpen, Ph.D. Thesis, Catholic University of Nijmegen (1988);
   (c) J. S. Baskin, Ph.D. Thesis, California Institute of Technology (1989).

6. See, for example, D. O. De Haan, A. L. Holton, and T. S. Zwier, J. Chem. Phys. **90**, 3952 (1989).

7. (a) D. V. Brumbaugh, J. E. Kenny, and D. H. Levy, J. Chem. Phys. **78**, 3415 (1983);

(b) K. W. Butz, D. L. Catlett, G. E. Ewing, D. Krajnovich, and C. S. Parmenter, J. Phys. Chem. **90**, 3533 (1986);

(c) T. A. Stephenson and S. A. Rice, J. Chem. Phys. **81**, 1083 (1984);

(d) R. L. Rosman and S. A. Rice, J. Chem. Phys. **86**, 3292 (1987).

8. (a) A. Mitchell, M. J. McAuliffe, C. F. Giese, and W. R. Gentry, J. Chem. Phys. **83**, 4271 (1985);

(b) B. A. Jacobson, S. Humphrey, and S. A. Rice, J. Chem. Phys. **89**, 5624 (1988);

(c) S. A. Wittmeyer, A. J. Kaziska, A. L. Motyka, and M. R. Topp, Chem. Phys. Lett. **154**, 1 (1989);

(d) M. Heppener and R. P. H. Rettschnick, in *Structure and Dynamics of Weakly Bound Complexes* , Ed. A. Weber (D. Reidel, Dordrecht, 1987), p. 553.

Chapter 2

Experimental

The purpose of this chapter is to describe the apparatus used for this experiment in enough detail that the fundamentals may be understood by someone unfamiliar with this field of chemistry. The apparatus has been described in detail before.[1]

In essence, the experiment is simple to understand: the van der Waals complex, effectively isolated from any outside influence in a free jet molecular beam expansion, is excited to a single, known vibrational level of an excited electronic state by a very short laser pulse. As the complex dissociates to form a rare gas atom and the bare molecule in various lower energy vibrational states, the concentration of the initial "reactant" state and the different "product" states is monitored as a function of time. In this way, one hopes to learn more about the detailed quantum mechanical processes that lead to unimolecular dissociation. The apparatus has three parts. First, a supersonic molecular beam expansion is used to form the weakly bound van der Waals complex and to cool it to a temperature of a few degrees above absolute zero, thus forming most of the weakly bound van der Waals complexes in the lower quantum states. Secondly, a synchronously-pumped, mode-locked, cavity-dumped, frequency-doubled dye laser system is used to generate tunable ultraviolet light in 15 ps long pulses at a 4 MHz repetition rate to excite the complexes in the molecular beam. Lastly, the time-correlated single photon counting technique is used to detect rapid changes in the fluorescence intensity from the excited complex and the dissociated product. Each of these parts of the apparatus will be briefly described in this chapter.

I) Molecular Beam Expansion

A supersonic molecular beam is formed when any gas is expanded through a pinhole from a high pressure to a low pressure such that the ratio of those

pressures exceeds 2.1.[2] When this is the case, the molecules in the expansion are moving faster that the speed of sound in the expansion and are effectively isolated from outside influences such as wall collisions. Beyond the pinhole the translational temperature and collision frequency each decrease rapidly in a predictable way. The microscopic result of the expansion of a monatomic gas is that the random thermal distribution of atomic velocities is converted into a more narrow distribution directed along the line of flow. Thus, the "temperature" of a monatomic gas, determined by the width of its velocity distribution, can be lowered well below its freezing point to only a few degrees Kelvin.[3]

If the expansion gas is a monatomic ideal gas and the flow is isentropic, the temperature, number density, and collision frequency of the molecules in a free jet molecular beam expansion are described by the equations[4]

$$T = T_0[1 + \frac{1}{2}(\gamma - 1)M_{eff}^2]^{-1}$$

$$n = n_0[1 + \frac{1}{2}(\gamma - 1)M_{eff}^2]^{\frac{-1}{\gamma-1}}$$

$$z = \sqrt{2}n\sigma\bar{v}_0[1 + \frac{1}{2}(\gamma - 1)M_{eff}^2]^{-\frac{1}{2}}$$

$$M_{eff} = 3.26(\frac{x}{D} - 0.075)^{.67} - 0.61(\frac{x}{D} - 0.075)^{-.67}$$

where T is the temperature of the gas in the expansion, γ is $\frac{5}{3}$ for a rare gas, M_{eff} is the effective Mach number, n is the number density, z is the collision frequency, σ is the hard sphere collision cross section, $\bar{v}_O$ is the mean molecular velocity in the reservoir, x is the distance the gas has expanded, D is the pinhole diameter, and the subscript zero refers to the conditions in the high pressure reservoir.

For the work described in this thesis, the supersonic expansion has been used to prepare cold van der Waals complexes for spectroscopic study. When a

polyatomic molecule is included as an impurity in the expansion of a monatomic carrier gas, collisions between the two as the mixture flows through the pinhole tend to equilibrate the temperature of the large molecule with that of the monatomic carrier gas. The polyatomic is accelerated to approximately the same speed as the carrier gas, the velocity distribution is similarly sharpened, and internal degrees of freedom are cooled to different degrees, depending on the cross section for collisional relaxation for each motion.[5]

Complex Formation

The theoretical and experimental description of cluster growth in molecular beams has not been quantitatively characterized as has been the description of the expansion of a monatomic gas. Empirical methods have been discussed and have been relied on for the work in this thesis.

Amirav *et al.*[6] have studied the formation of van der Waals complexes of tetracene (T) with argon for between one and seven bound argon atoms. Their data was modeled using the hypothesis that the formation of all TAr_n complexes is due to the three-body collisions

$$T\text{-}Ar_{n-1} + Ar + Ar \rightarrow T\text{-}Ar_n + Ar.$$

Studying the excitation spectra of tetracene seeded in an argon molecular beam expansion, they were able to identify seven transitions red of the origin band of bare tetracene which they attribute to the origin bands of seven complexes with argon, TAr_n, n=1, 7. The intensity of each of these excitation bands as a function of argon backing pressure in the expansion was described by the equation,

$$\frac{[T\text{-}Ar_n]}{[T]} = (Kp^2)^n$$

where K is a constant and p is the pressure in the molecular beam reservoir. Thus, higher argon pressures increase the number of three-body collisions

leading to complex formation and increase the concentration of the complex in the expansion.

In the course of this work, we discovered that the concentrations of the complexes we studied were increased further when only a small amount of the rare gas of interest was mixed with helium rather than using an expansion of the pure rare gas.

Operating Conditions

For the molecular beam system used for the work in this thesis, either of two nozzle assemblies were used. For backing pressures up to $\approx$ 100 psi, an o-ring clamp was used to hold a glass reservoir containing the stilbene or anthracene. The glass reservoir was fused to a 1/16 inch inner diameter glass tube which had been melted, drawn and ground with sandpaper so that the final aperture through which the molecular beam expanded was $\sim$ 50 μ in diameter. This assembly was used for expansions of neon and argon complexes. The concentration of these complexes was found to be largest when the expansion gas contained $\sim$1% neon or argon in helium.

For the higher backing pressures necessary to form helium complexes in the expansion, a metal assembly with nickel gasket seals was used with nickel or molybdenum electron microscopy apertures of between 25 and 50 μ in diameter. With this assembly, backing pressures up to $\sim$800 psi could be used before the background pressure in the chamber rose significantly. Each of the nozzle assemblies could be heated up to 185°C during normal operation. The expansion was interrogated by the laser at a distance from the nozzle corresponding to between 30 and 60 nozzle diameters, at which point the expansion was found to be in a steady-state.

Using these nozzle assemblies the molecular beam was expanded into a

36x12 inch cylindrical stainless steel chamber evacuated with a 12 inch bore, ring jet booster diffusion pump (Edwards 18B4A) with a pumping speed of 4000 L/s ($\leq 10^{-2}$ torr) which was backed with a 150CFM roughing pump (Kinney, Kt-150). The pressure in the chamber with the molecular beam in operation was $\leq$ 1 millitorr.

Under the conditions of the experiments reported in this thesis, the equations above give a final translational temperature of $\sim$ 1K and a collision rate of 10^4/second. The rotational temperature of the complexes was measured by rotational coherence techniques to be $\sim$ 1K under normal operating conditions.[7] Vibrational temperatures are low enough that single vibrational levels can be excited from the vibrationless state, independently of any overlapping sequence transitions from thermally populated levels in the molecular beam. Thus, the apparatus is capable of producing a cold beam of van der Waals complexes of polyatomic molecules with rare gas atoms, effectively isolated on the timescale of the experiments discussed in this thesis ($\leq$ 10ns).

II) Picosecond Laser System

The tunable ultraviolet picosecond laser pulses used in the experiments discussed in this thesis were formed in four distinct steps: (1) The green 514 nm line of an Ar^+ laser is mode-locked to form $\sim$150 ps pulses, (2) the green pulses synchronously pump a dye laser which is (3) cavity dumped to give picosecond pulses ($\sim$ 15ps) in the visible, and (4) frequency doubled into the ultraviolet. Each of these steps will be briefly discussed.

Mode locking is achieved when many longitudinal modes are forced to oscillate with a fixed phase relationship.[8] In this laser system, this is achieved by frequency shifting and diffracting a portion of each longitudinal mode with an acousto-optic modulator, driven at its natural frequency of 40.8 MHz. When

the cavity length of the laser is adjusted so that the longitudinal modes are separated by this same frequency, each mode is forced to oscillate in phase with one another. The result of this coherent superposition of the longitudinal modes is a series of pulses, the width of which is the inverse of the gain envelope. The time between pulses is inversely proportional to the separation between the longitudinal modes. For the experiments in this thesis, the 514 nm line of a Spectra-Physics Model 171 or 2030 Ar^+ laser was mode locked with a model 342A mode-locking system by simultaneously maximizing the height and minimizing the width of the pulses viewed after two reflections off glass plates and viewed with a Spectra-Physics Model 403B high speed photodiode. Typical results were 150 ps (FWHM), 400 mV pulses and a total power output of 0.5 W at 82 MHz.

The green ion laser output is used to synchronously pump a dye laser. The dye solutions used for this work were a 2 x 10^{-3} M solution of R6G in ethylene glycol for the stilbene experiments and a 1.5 x 10^{-3} M solution of DCM in a 3:2 (volume) mixture of ethylene glycol and benzyl alcohol for the anthracene experiments. Synchronous pumping occurs when the length of the dye laser cavity is matched to that of the ion laser. When the cavity lengths are matched, the circulating dye laser pulse stimulates the dye to lase just after a single ion laser pulse has excited it above threshold. Because of the large cross-section for emission of the dye molecules, the excited dye is rapidly stimulated to emit by the circulating dye pulse and the red output is composed of shorter, 15ps wide pulses which are then periodically (4MHz) diffracted out of the cavity by another acousto-optic modulator in a Spectra-Physics model 344 Cavity Dumper. These 15ps pulses of visible light are frequency doubled in 1 cm long crystals of $LiIO_3$. The dye laser cavity length and the fine adjustments of the dye laser

and cavity dumper are then adjusted to maximize the uv output. Typically, this was ~1mW at 4 MHz. These laser pulses were then reflected into the molecular beam chamber and focused onto the expansion, perpendicular to the expansion axis. For the anthracene experiments, tuning the dye laser was accomplished by rotating a three-plate birefringent filter which gives a spectral width in the uv output of 5 cm^{-1}. An ultra-fine tuning etalon was included as a tuning element for the stilbene experiments, narrowing the width to 2 cm^{-1}.

III) Time-correlated Single Photon Counting

Description

The temporal date in this thesis was measured using the time-correlated single photon counting (TCSPC) method. This technique relies on using a stable, high repetition rate excitation source to measure fast changes in fluorescent intensity.

The heart of a TCSPC experiment is a charging capacitor in a time-to-amplitude converter (TAC). A triggering pulse from the laser initiates the charging of this capacitor in addition to optically exciting a fluorescing sample. The fluorescence is focused onto a photomultiplier tube (PMT) and the first detected PMT pulse is used to stop the charging capacitor. Thus, each start-stop cycle corresponds to the detection of a single fluorescent photon and the charge accumulated on the capacitor is proportional to the time between the excitation of the sample and the emission of that single photon. Because only a single fluorescent photon is detected (by stopping the capacitor from charging) for each excitation of the sample, it is necessary that the probability of detecting a photon, for any single excitation, is sufficiently low that all delay times are equally likely to be sampled. The start-stop cycle is repeated thousands of times, until a sufficiently high signal-to-noise histogram of the fluorescent behavior of the

sample is built up. The necessity of having a relatively low detection count rate and of repeating the excitation-detection cycle so many times is not a severe limitation since the excitation source for these experiments operates at a repetition rate of 4 MHz. Most of the data curves in this thesis were collected at a rate of ~1000 detected photons per second, and well defined decay curves could be collected in under 1 hour.

The data in this thesis was collected operating the TAC in the "reverse" mode[9]. Fluorescent photons were detected by one of three PMTs, an Amperex 2020Q, a Hamamatsu R1564U, or a Hamamatsu 2287, depending on the relative importance of a high photocathode quantum efficiency and a small PMT pulse width. The pulses from the PMTs were amplified by 500 MHz Comlin CDC100 video amplifiers, if necessary, shaped and discriminated against by a Tennelec 455 constant fraction differential discriminator and used to start the charging capacitor in an ORTEC 457 TAC. Stop pulses for the TAC were provided by intercepting the red part of the laser beam that was not frequency doubled with a modified[10] Hewlett-Packard 5082 fast photodiode, amplified by a 1.3 GHz Hewlett-Packard 8447 inverting amplifier and shaped and discriminated against as with the PMT pulses. The TAC output was collected by a Traco Northern TN-1706 multichannel analyzer (MCA) operated in the pulse height analysis mode. Dispersed fluorescence spectra were measured by counting the total number of detected fluorescent photons with the MCA as the grating of a 0.5 m monochromator (Spex 1870) was scanned by a microprocessor control (Spex CD2). The data was read, stored and analyzed on a DEC PDP 11/23 computer.

CurveFitting

The temporal data discussed in this thesis was fit as single, double, and

triple exponential decays. To correctly account for the limited temporal resolution of the excitation source and the detection system, the convolution of such decays with the system response function has to be considered. The system response function measures the ability of the detection system to respond to an impulse and was measured by detecting scattered laser light. Thus, when a single exponential decay is measured, an apparent fast risetime is observed because of the width of the excitation source and the limited ability of the PMT and the TCSPC electronics to respond to fast fluorescent signals. This is expressed by the convolution integral

$$I(t) = \int_0^{t'} R(t')D(t-t')dt'$$

where $I(t)$ is the measured fluorescence intensity at a particular time, $R(t)$ is the measured system response function, and $D(t)$ is the actual time dependence of the fluorescence one is trying to measure.

Measured, convoluted decay curves were fit using the nonlinear least squares method with Marquardt's algorithm. The least squares method minimizes the deviation of the measured data from a fit of an assumed functional form, with respect to the parameters of the fit; that is, the method minimizes the chi-squared statistic

$$\chi^2 = \sum_{i=n_1}^{n_2} \frac{[I(t_i) - F(a_1, a_2..., a_k, t_i)]^2}{\sigma_i^2}$$

where $F(a_k, t_i)$ is the assumed functional form of the data, convoluted with the system response function, the a_k are the parameters of the fit that are to be determined, $I(t)$ is again the measured data, n_1 and n_2 are the first and last points of $I(t)$ to be fit and σ_i is the standard deviation for each measured point. In a TCSPC experiment, the probability of detecting some number of photons

(N) in any given time range is given by a Poisson distribution[9] with a standard deviation $\sqrt{N}$, and is approximated by $\sqrt{I(t_i)}$ in calculating χ^2.

The parameters which minimize χ^2 are solved for by successive iteration. The function with the correct, unknown parameters of the fit is considered to be expanded in a Taylor series around an initial estimate for the parameters of the fit, keeping the first order terms. Marquardt's method is then used to calculate better guesses for the parameters until a minimum χ^2 is found. The calculation is discussed in detail in references 9, 11 and 12.

REFERENCES

1. (a)A. H. Zewail, Faraday Disc. Chem Soc. **75**, 315 (1983);
   (b) W. R. Lambert, Ph.D. Thesis, California Institute of Technology (1982).

2. David R. Miller, in *Atomic and Molecular Beam Methods*, ed. G. Scoles (Oxford, New York, 1988).

3. R. E. Smalley, L. Wharton, and D. H. Levy, Accounts of Chem. Res. **10**, 139 (1977).

4. D. M. Lubman, C. T. Rettner, and R. N. Zare, J. Phys. Chem. **86**, 1129 (1982).

5. (a) D. H. Levy, L. Wharton, and R. E. Smalley in *Chemical and Biological Applications of Lasers* Volume VII, ed. C. B. Moore (Academic, New York, 1977);
   (b) D. H. Levy, Ann. Rev. Phys. Chem. **31**, 197 (1980).

6. A. Amirav, U. Even, and J. Jortner, J. Chem. Phys. **75**, 2489 (1981).

7. J. S. Baskin, P. M. Felker, and A. H. Zewail, J. Chem. Phys. **86**, 2483 (1987).

8. (a) Amnon Yariv, *Quantum Electronics* (John Wiley, New York, 1975).

(b) B. Couillaud and V. Fossate-Bellani, Lasers and Applications **IV**, 79, January 1985.

9. Desmond V. O'Connor and David Phillips, *Time-correlated Single Photon Counting* (Academic, London, 1984).

10. G. H. McCall, Rev. Sci. Inst. **43**, 865 (1972).

11. J. N. Demas, *Excited State Lifetime Measurements* (Academic, New York, 1983).

12. P. R. Bevington, *Data Reduction and Error Analysis for the Physical Sciences* (McGraw-Hill, New York, 1969).

Chapter Three

Analysis of Time-resolved Data and Sensitivity of Experiments

The purpose of this chapter is to discuss the functional form of the the time resolved data measured in these experiments and how it can be related to the molecular dynamics of the van der Waals systems studied.

As will be seen in Chapters Four and Five, all the data was fit well by exponential curves, so only rate processes are considered. We consider first-order, unimolecular decays of individual vibrational levels due to intramolecular vibrational redistribution (IVR) to other bound states and decays due to vibrational predissociation (VP) to continuum states of the dissociated fragments.

IVR[1] is the process that occurs when *coupled* vibrational states are excited and detected. For example, if a single normal-mode vibrational state with absorption strength were coupled by anharmonicities or Coriolis interactions with a small number of "dark" states and excited coherently so that each of the individual molecular eigenstates were simultaneously excited at t=0, then the population in the absorbing state would flow into and out of the dark modes which are also part of the molecular eigenstates. Lahmani has shown[2] (for the analogous process of intersystem crossing) and Felker has experimentally verified[3] that IVR amongst a large number of coupled levels may be modeled by kinetic rate equations when the excitation is coherent and the emitting states (but not the eigenstates) are spectrally resolved. In the limit of many coupled levels, the population in the initially excited state would decay exponentially with a rate proportional to the width of the distribution of beat frequencies and the population in the "redistributed" states would increase with that same rate. Our data will be modeled in this way.

Vibrational predissociation is similar to IVR, except that the "final" states are continuum states of the recoiling fragments. Thus population evolves from an initial zero-order bound state of the molecular complex into a coordinate

for which the energy of the system is above the dissociation energy. Fano has shown[4] (for the analogous process of autoionization) that when a discrete zero order state is coupled to a continuum and prepared coherently, it will dissociate into the continuum with a rate proportional to the strength of the coupling between the zero-order discrete state and the zero-order continuum states. It is therefore appropriate to model VP as a first-order kinetic process.

I. Kinetic Models

A.) Parallel and Sequential Kinetics

As the simplest possible mechanism, first consider the kinetics if the initially excited state were to directly decay by several paths. For example, suppose IVR formed a metastable state of the complex which fluoresced and, simultaneously, VP formed the molecular part of the complex in a lower vibrational state which also fluoresced:

$$\begin{array}{ccccc} & & A^* + R & \xrightarrow{k_f} & A + R \\ & \overset{k_{vp}}{\nearrow} & & & \\ A\text{-}R^*_{initial} & & & & \\ & \underset{k_{ivr}}{\searrow} & & & \\ & & A\text{-}R^*_{final} & \xrightarrow{k_f} & A\text{-}R \end{array}$$

where A is an aromatic molecule, R is a rare gas atom, and the star indicates electronic excitation. (For simplicity, the fluorescent decay rates of the initial and intermediate states will be ignored at this point. Also, we will assume $k_f \ll k_{ivr}$ or k_{vp}). Solution of the kinetic equations for this mechanism gives

$$[A\text{-}R^*_i(t)] = [A\text{-}R^*_i(0)]e^{-(k_{ivr}+k_{vp})t}$$

$$[A^*(t)] = [A\text{-}R^*_i(0)]\frac{k_{vp}}{k_{vp}+k_{ivr}-k_f}\left(e^{-k_f t} - e^{-(k_{ivr}+k_{vp})t}\right)$$

and

$$[A\text{-}R_f^*(t)] = [A\text{-}R_i^*(0)]\frac{k_{ivr}}{k_{vp}+k_{ivr}-k_f}\left(e^{-k_f t} - e^{-(k_{ivr}+k_{vp})t}\right).$$

Therefore, the only difference in the two channels reflecting the individual rates appears in the relative proportion of the two products. When these equations are integrated to give the total product state distribution (PSD), the fraction of redistributed complex formed, for example, is proportional to $k_{ivr}/(k_{ivr}+k_{vp})$.

If more decay channels are open to the intial state, the form of the kinetic equations is the same: the temporal evolution of the initial state is a single exponential with the total decay rate and each product state population evolves as a biexponential rising with the same rate. The amount of each product formed is determined by the ratio of the rate for that channel to the total rate.

In contrast, the temporal results are different in functional form if the decay processes occur sequentially. For example, if IVR preceeded VP and the bare molecular product fluoresced (again ignoring the fluorescence rates of the complex levels for simplicity)

$$A\text{-}R^*_{initial} \xrightarrow{k_{ivr}} A\text{-}R^*_{final} \xrightarrow{k_{vp}} A^* + R \xrightarrow{k_f} A + R,$$

a general result is that each state involved in the dissociation process would have a temporal behavior described by a sum of exponentials, one for each rate process which preceeded it and another for its decay rate[5]. In the given example,

$$[A\text{-}R_i^*(t)] = [A\text{-}R_i^*(0)]e^{-k_{ivr}t}$$

$$[A\text{-}R_f^*(t)] = \frac{k_{ivr}}{k_{vp}-k_{ivr}}[A\text{-}R_i^*(0)]\left(e^{-k_{ivr}t} - e^{-k_{vp}t}\right)$$

$$[A^*] = \frac{k_{ivr}k_{vp}}{(k_f-k_{vp})(k_f-k_{ivr})}[A\text{-}R_i]_0\left\{e^{-k_f t} + \frac{k_f-k_{vp}}{k_{vp}-k_{ivr}}e^{-k_{ivr}t} + \frac{k_f-k_{ivr}}{k_{ivr}-k_{vp}}e^{-k_{vp}t}\right\}.$$

The emission of the bare molecule, (which has a relatively long lifetime in these experiments) *would be a triple exponential* with a risetime equal to the slower of the two rates and with the faster rate appearing in an additional, weak decay. In this case, the amplitudes of each component of the triexponential are not equal in magnitude as they are for the biexponentials that are observed if the kinetics are parallel, but are functions of k_{ivr}, k_{vp}, and k_f.

For sequential IVR and VP then, the result is different in form from the result when the two processes occur in parallel from the initially excited state. The risetime of product fluorescence may be equal to *or slower* than the decay time of the initial state. In either case, the temporal behavior of the final product is no longer biexponential (although it appears to be if the temporal resolution is too slow to resolve the fast, additional decay.)

A priori, there is no reason to assume the dissociation mechanism will be as in either simple case, rather than involving some of each simple mechanism. For example, after redistribution to a level including excited van der Waals modes, predissociation could occur to different final states with different rates:

$$
\begin{array}{lcll}
 & & A_1^* + R & \xrightarrow{k_f} \quad A_1 + R \\
 & \overset{k_{vp1}}{\nearrow} & & \\
A\text{-}R^*_{initial} \xrightarrow{k_{ivr}} & A\text{-}R^*_{final} & & \\
 & \underset{k_{vp2}}{\searrow} & & \\
 & & A_2^* + R & \xrightarrow{k_f} \quad A_2 + R
\end{array}
$$

In this case the kinetic behavior of the states involved would be similar to that if predissociation occurred to only a single state; that is, triexponentials would be observed for the final states. As discussed for parallel kinetics, however, k_{vp1} and k_{vp2} would always be observed in the rates as the sum. Again, the only effect of

those individual rates would be in the product state distributions. The amount of product from the first channel, for example, would be nearly proportional to $k_{vp1}/(k_{vp1}+k_{vp2})$, strictly proportional for $k_f \ll k_{ivr}$ and k_{vp}.

The most general mechanism involving these ideas would be if the initial state were to redistribute to a number of states, each of which could independently predissociate:

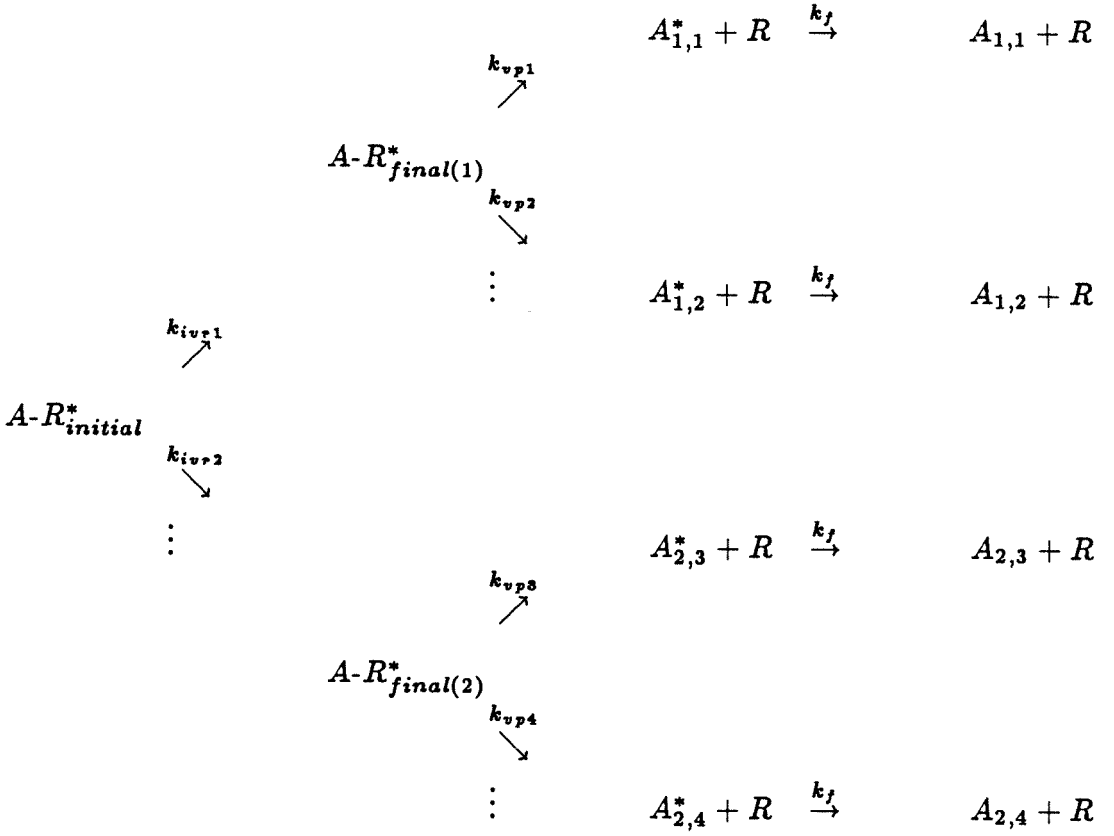

As with the simple parallel decay mechanism, the decay rate of the initial state is equal to the sum of IVR rates into the different channels and each channel will have a PSD proportional to the ratio of the rate into that channel to the total rate. As with the simple sequential mechanism, the temporal behavior of each dissociated product will be triexponential which will rise with the slower of the VP rate out of the intermediate state which preceeded it and the total IVR rate out of the initially excited state. What is new in this mechanism is

that *different product states of the bare molecule may have different risetimes*, reflecting different total rates of predissociation, if the redistribution rate out of the initially excited state is comparatively fast.

Integrating these equations to find the product state distribution and taking k_f to be small compared to k_{ivr} and k_{vp}, one finds that the contribution of the initial, the redistributed, and the dissociated state to the fluorescence spectrum is proportional to its lifetime, and when several channels are open, to $\approx k_i / \sum_i k_i$.

Our conclusions on the role of IVR in the dissociation process are based on this analysis. They are:

(1) If the product fluorescence is a biexponential with a risetime equal to the decay time of the initially excited state, then only a single process may be inferred, though it may consist of any number of parallel channels. The reaction mechanism may still have more than one step, but only the first is resolvable.

(2) If more than one rate is observed, the reaction mechanism must have more than one step, i.e., IVR precedes VP. This could occur by observing (a) a single triexponential for a single stilbene product; (b) two stilbene products with different risetimes reflecting different VP rates from different intermediate states and unresolvable fast third components; (c) a product stilbene decay that has a risetime (VP) slower than the decay of the initially excited state (IVR).

B) Reversibility

A further complication that must be investigated is the possibility of reversible IVR. If there is a single decay path, but the first step is reversible,

$$A\text{-}R^*_{initial} \overset{k_{\pm ivr}}{\rightleftharpoons} A\text{-}R^*_{final} \overset{k_{vp}}{\rightarrow} A^* + R \overset{k_f}{\rightarrow} A + R$$

solution of the appropriate kinetic equations gives

$$[A\text{-}R_i^*(t)] = \frac{[A\text{-}R_i^*(0)]}{(k_{ivr}-k_{fast})^2 + k_{ivr}k_{-ivr}} \left\{ k_{ivr}k_{-ivr}e^{-k_{fast}t} + (k_{ivr}-k_{fast})^2 e^{-k_{slow}t} \right\}$$

$$[A\text{-}R_f^*(t)] = \frac{k_{ivr}(k_{fast}-k_{ivr})}{(k_{ivr}-k_{fast})^2 + k_{ivr}k_{-ivr}} [A\text{-}R_i^*(0)] \left(e^{-k_{slow}t} - e^{-k_{fast}t} \right)$$

$$[A^*] \propto e^{-k_f t} + \frac{k_f - k_{slow}}{k_{slow}-k_{fast}} e^{-k_{fast}t} + \frac{k_f - k_{fast}}{k_{fast}-k_{slow}} e^{-k_{slow}t}$$

where

$$k_{fast} = \frac{1}{2}(k_{ivr}+k_{-ivr}+k_{vp}) + \frac{1}{2}\sqrt{(k_{ivr}+k_{-ivr}+k_{vp})^2 - 4k_{ivr}k_{vp}}$$

$$k_{slow} = \frac{1}{2}(k_{ivr}+k_{-ivr}+k_{vp}) - \frac{1}{2}\sqrt{(k_{ivr}+k_{-ivr}+k_{vp})^2 - 4k_{ivr}k_{vp}}.$$

The functional form of the equation for the dissociated product is identical to the form of the equation for sequential kinetics. Therefore, by measuring the temporal behavior of the dissociated product, the presence or absence of reversibility in the redistribution step cannot be distinguished. Measurement of the decay of the initial state, however, can, in general, distinguish between the paths with and without reversible redistribution, since the effect of the reversibility is to add another decaying component to the temporal behavior of the initial state. The relative amplitude of the fast and slow components of the decay of the initial state cannot be expressed in terms of k_{fast} and k_{slow}, however, nor can it be expressed simply if $k_{ivr}=k_{-ivr}$.

If two products are formed and the IVR steps are reversible,

$$A\text{-}R^*_{initial} \overset{k_{\pm ivr1}}{\rightleftharpoons} A\text{-}R^*_{final(1)} \overset{k_{vp1}}{\rightarrow} A^*_{1,1} + R \overset{k_f}{\rightarrow} A_{1,1} + R$$

$$A\text{-}R^*_{initial} \overset{k_{\pm ivr2}}{\rightleftharpoons} A\text{-}R^*_{final(2)} \overset{k_{vp2}}{\rightarrow} A^*_{2,2} + R \overset{k_f}{\rightarrow} A_{2,2} + R$$

a 5 x 5 matrix must be diagonalized to solve for the time dependence of the different states. This was done numerically for many different values of the rates. In general the temporal evolution of the initial state will be described by the sum of two decaying exponentials and that of the products will be described by the sum of four exponentials. From the numerical calculations it was found that the additional exponential components are obvious when τ_{-ivr} is on the same order of magnitude as τ_{ivr} or τ_{vp} and are apparent when τ_{-ivr} is several times slower. Furthermore, even if the two forward IVR rates differ by a factor of ten, the four-exponentials for each of the two products become very similar. Unlike the case without reversible redistribution, different products do not have different risetimes. As will be shown in Chapters Four and Five, the data in this thesis is accounted for without these complications suggesting that the IVR we observe is irreversible.

C. Radiative Rates of Intermediates

The radiative decay rates of the initial and redistributed states of the complexes were assumed to be the same as the radiative rate of the bare aromatic molecule at the same energy. Because fluorescence occurs in parallel to IVR and VP, fluorescence does not change the form of the final equations, it only increases the measured rates. Because these radiative rates are so much slower than the IVR and VP rates that were measured, including the radiative rates in the analysis hs the effect of correcting the measured IVR and VP rates by <10%.

II. Effect of Experimental Inaccuracies

In order to critically evaluate the measured data, we discuss in this section the validity of choosing the functional form of the fit and the accuracy with which the lifetimes can be measured. Our evidence for the validity of the fit is based on two practical observations. First, in the fluorescence of the resonantly

excited bare aromatic molecule, we have a "standard" single exponential with which we can compare other temporal data. Secondly, we will show that our data was collected to a high enough signal-to-noise that data which have additional, fast components can be distinguished from data that do not.

Data is fit to the most simple exponential form possible, evaluating the "goodness" of the fit with the calculated reduced χ^2 parameter and by inspecting the residual of the data for consistent errors.

The reduced χ^2 parameter, χ^2_r, is calculated simply by dividing the χ^2 parameter, discussed in Chapter 2, by the number of degrees of freedom in the fit, i.e., the number of parameters in the fit subtracted from the number of points fit minus one.[6] If a single decay is repeatedly measured and fit to the correct form, the evaluated χ^2_r parameters should be distributed according to the χ^2 distribution.[6] The probability of any single χ^2_r being greater than 1.10 is only 1.5%. The χ^2_r of a single fit, therefore, only indicates if the fit is statistically unlikely to be the correct fit. Experimentally, excellent fits are achieved with χ^2_r below 1.1 and nearly all the data in this thesis have fits with lower values of χ^2_r.

The residual of a fit is a plot of the number of standard deviations a single point is from that point of the calculated fit. Since the number of detected photons for a particular time range should follow a Poisson distribution, the probability of any single point being more than 3σ away from the correct fit is $<0.1\%$. More important for this work, a plot of the residual reveals consistent errors as will be shown in the next section.

The resolution with which additional decay components can be identified and the accuracy with which the lifetimes can be fit is evaluated using "synthesized" data and is discussed in the next section.

A. Convolution Effects-Experimental Considerations

The convoluted rise in any measured temporal data depends sensitively on the width, shape, and position of the system response function and also contains most of the signal due to fast rising or decaying lifetime components. Therefore, for this work it was important to measure the correct response, that is, the response that corresponds to the measured temporal data, and also for the response to remain stable during the measurement of a decay curve.

Most critical is the precise way in which laser light is scattered to measure the system response function and signal is focused onto the photomultiplier to measure the temporal data. In preliminary experiments we observed a shift as large as $\sim 2/3$ of the full width at half maximum (fwhm) in the peak of the response, changing only the alignment of the molecular beam and the collection optics. This shift is likely due to transit time effects from detecting the light scattered onto different parts of the multichannel plate PMT cathode. Before we could consistently and accurately measure the rising part of the temporal data, convoluted with the system response function, it was necessary to align the molecular beam and detection optics so that an accurate response, not shifted with respect to the temporal data or distorted in shape, could be consistently measured.

In addition, for the stilbene experiments it was necessary to discriminate against rotational coherence effects[7] in order to accurately measure the convoluted rises of temporal data. To measure data insensitive to the polarization of the sample in the expansion due to the polarization of the excitation source, the plane of the laser polarization was rotated so that equal amounts of fluorescence were detected parallel and perpendicular to the initial laser polarization. For the signal-to-noise levels of the data in this thesis, this was sufficient to discriminate against rotational coherence effects, and it was not necessary to detect

fluorescence at the magic angle (and thus lose signal from having to introduce a polarizer into the collection optics.) Finally, for the stilbene experiments it was necessary to keep the temperature of the stilbene in the molecular beam reservoir near or below the melting point of stilbene. At higher temperatures resonantly excited stilbene fluorescence appeared to have a fast (~20ps) rising component.

Taking these problems into consideration, single exponential decays of resonantly excited fluorescence from the bare molecule could consistently be fit from the sharp, convoluted rise to the end of the decay (see Figure 1). Such a single exponential decay was collected and fit at the beginning and end of each day, a control experiment. In addition, the system response function was monitored periodically throughout each day so that drifts and changes in its shape were recognized.

Figure 2 shows the difference between single and double exponential fits of the fast rise in the fluorescence from bare, vibrationless stilbene formed after exciting stilbene-He at 95 cm^{-1}. Note the different scales in the residuals of the two fits. Identical response functions of fwhm = 82 ps were measured before and after this data. The single exponential fit is shifted 26 ps with respect to the measured response so that the fit intersects the middle of the measured rise of the data, entirely missing experimental data points before and after. This systematic error also appears clearly in the residual.

In a similar way, Figure 3 compares double and triple exponential fits to the temporal data for the fluorescence vibrationless stilbene formed after exciting stilbene-Ne at 198 cm^{-1}. Identical system response functions were measured directly before and after this data, as were well-fit decays of resonantly excited bare stilbene. Again, the incorrect fit alternately deviates from the experimen-

tal data and is shifted from the measured response substantially (32 ps) so as to minimize the effect of the unaccounted for fast lifetime. Furthermore, although the eight fit parameters of the triexponential were treated as entirely independent, the ratios of the amplitudes of the fast lifetime components to the amplitude of the fluorescent decay, -1.34 and 0.36, are the same within experimental error as those calculated from the lifetimes using the equations for the sequential mechanism discussed in Section I.A, -1.33 and 0.33.

During the course of the experimental work described in this paper, the two decays plotted in Figures 2 and 3 were measured, respectively, four and six times, independently, on different days, under different conditions of laser power, total pressure, etc. The standard deviation of each of the measured lifetimes and amplitude ratios for the repeated measurements of those decays were all under 10%. This figure gives the most realistic estimate of the error in the measured lifetimes and amplitudes. In the text, the average of the measured lifetimes will be reported.

Simulated Data

In addition to the spread of values actually measured for a particular lifetime, additional estimates of the experimental accuracy can be made using "synthetic" data. Synthetic data was created by calculating the intensity as a function of time for a particular set of parameters, convoluting it with a measured experimental response, and adding Poisson noise calculated with a random number generator. By then fitting this data with an incorrect functional form or with a shifted or broadened response, the effect of these errors and the accuracy of the fitted parameters could be estimated.

a) Resolution

Figure 4 shows a simulated double exponential curve with parameter similar

to those of the data of Figure 2, with ~3000 detected photons at the maximum, fit as single and double exponential curves, respectively. As with the experimental data discussed in the previous section, the effect of the unaccounted for fast lifetime is to dramatically shift the data with respect to the measured response and to introduce a consistent error in the residual of the fit. On the basis of figure 3, we take ~20 ps to be the limit of our resolution for a risetime with a response function of fwhm = 80 ps and 3000 counts at the maximum. With the same response, simulated triple exponential data shows that 40 ps is approximately the fastest third decay component that can be measured if the risetime is 232 ps and $A_{fast}/A_{fluor} = .19$ as would be the case if the data were described by a triple exponential as in Section I.A or I.B.

Double and triple exponential decay curves synthesized using a variety of parameters similar to the parameter of the data in Figure 2 fit to within less than 5% of the correct lifetimes.

b) Experimental Errors

The greatest source of experimental error is due to drifting responses due to jitter in the timing electronics. The effect of a response that drifts over the course of the measurement of a decay curve is that the true response is broadened and shifted from the measured response. The immediate effect in the fit of such data is that a shift is calculated for the fit of the data with the respect to the response. This shift is evident in the simulated data for a drift of ~1/3 of the fwhm of the response. A "bad" fit is not discerned from the value of χ_r^2 and the residual until the response has drifted approximately ~3/4 of the fwhm of the response. Figure 5 shows that a good fit can be obtained, even for relatively large drifts of the position of the response compared to the fwhm. The data in Figure 5 was simulated from a response artifically drifted by 1/2 of the fwhm

of the response and fit with the response that was not artifically drifted. The 'drifted' response was shifted in time by 1/4 of the fwhm and broadened by 1/10 of the fwhm. In the course of the experiments discussed in this thesis, the measured shifts in the measured response were generally less than 1/10 of the fwhm and broadening was rarely observed.

In this chapter we have shown that under the conditions of the experiments discussed in this thesis, single, double and triple exponential decays with lifetimes as short as ~20 ps can be accurately and reproducibly measured.

REFERENCES

1. P. M. Felker and A. H. Zewail, in *Advances in Chemical Physics*, Volume LXX, Part 1, Ed. I. Prigogine (John Wiley, New York, 1988).

2. F. Lahmani, A. Tramer, and C. Tric, J. Phys. Chem. **60**, 4431 (1974).

3. P. M. Felker, Ph.D. Thesis, California Institute of Technology (1984).

4. U. Fano, Phys. Rev. **124**, 1866 (1961).

5. S. W. Benson, *The Foundations of Chemical Kinetics* (McGraw-Hill, New York, 1960).

6. (a) J. N. Demas, *Excited State Lifetime Measurements* (Academic Press, New York, 1983).
   (b) Desmond V. O'Connor and David Phillips, *Time-correlated Single Photon Counting* (Academic Press, London, 1984).
   (c) P. R. Bevington, *Data Reduction and Error Analysis for the Physical Sciences* (McGraw-Hill, New York, 1969).

7. J. S. Baskin, P. M. Felker, and A. H. Zewail, J. Chem. Phys. **86**, 2483 (1987).

Figure Captions

Figure 1. Fluorescence decay of resonance emission from bare stilbene excited to the vibrational level $36^2 37^2$, fit as a single exponential decay (τ_f=2.6ns) convoluted with the system response function. The full width at half maximum of the measured system response function, Δ, was 82ps. For this fit, χ_r^2=1.09.

Figure 2. Single and double exponential fits of the emission from bare, vibrationless stilbene formed in the dissociation of stilbene-He 37^2. Δ=82ps and χ_r^2=3.64 and 1.04, respectively.

Figure 3. Double and triple exponential fits of the emission from bare, vibrationless stilbene formed in the dissociation of stilbene-Ne 25^1. Δ=76ps and χ_r^2=1.96 and 0.93, respectively.

Figure 4. Single and double exponential fits of computer simulated data with a fast (20ps) risetime. Δ=76ps and χ_r^2=0.94 and 1.38, respectively.

Figure 5. Computer simulated data illustrating the effect of a drifting response on the fast, convoluted rise of measured temporal data. The parameters of the simulation are discussed in the text. For this single exponential fit using the same response as above, χ_r^2=1.09, and the shift of the fit is 19ps.

Figure 1

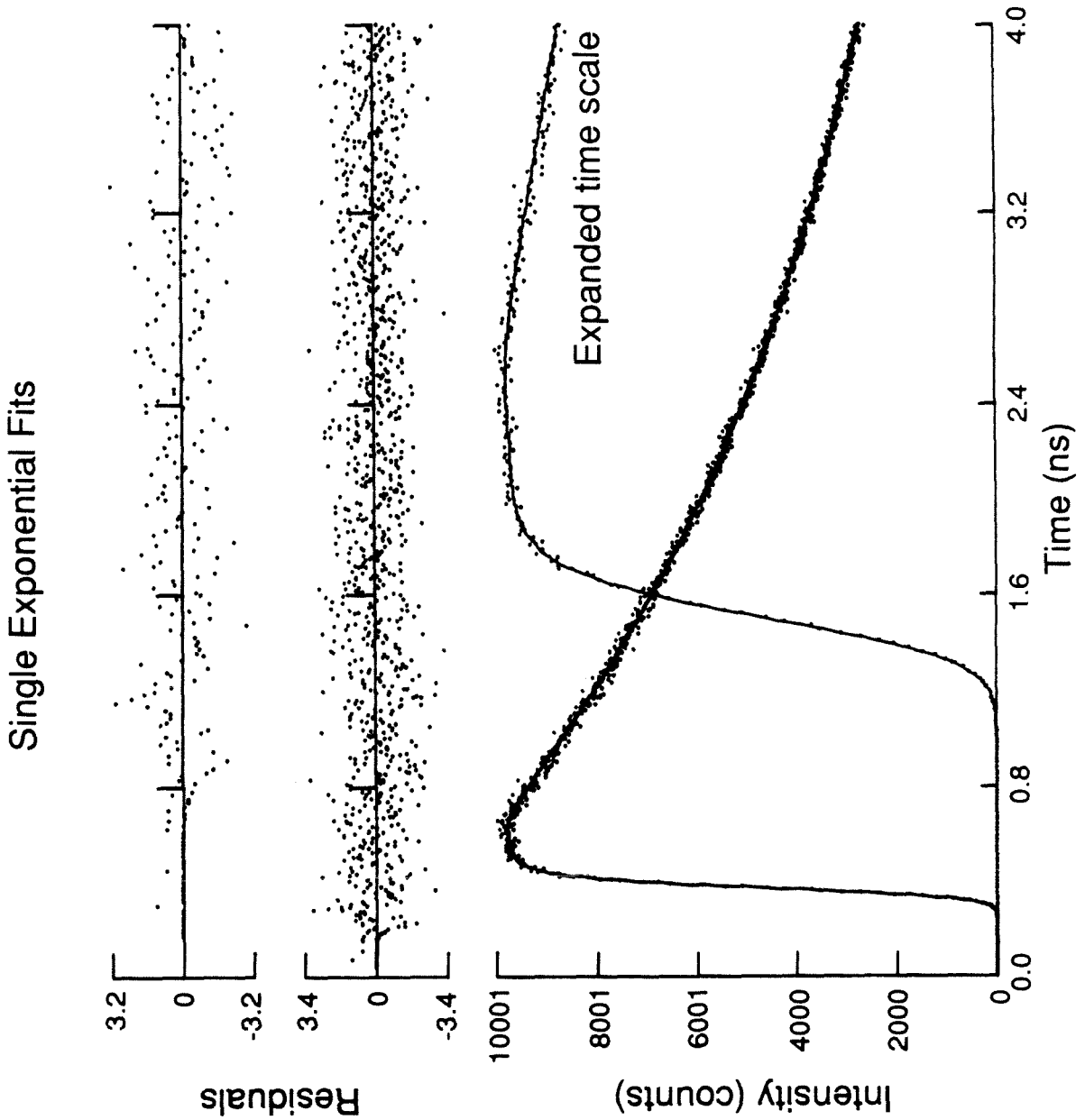
Single Exponential Fits
Residuals
3.2
0
-3.2
3.4
0
-3.4
Intensity (counts)
10001
8001
6001
4000
2000
0
Expanded time scale
0.0
0.8
1.6
2.4
3.2
4.0
Time (ns)

Figure 2

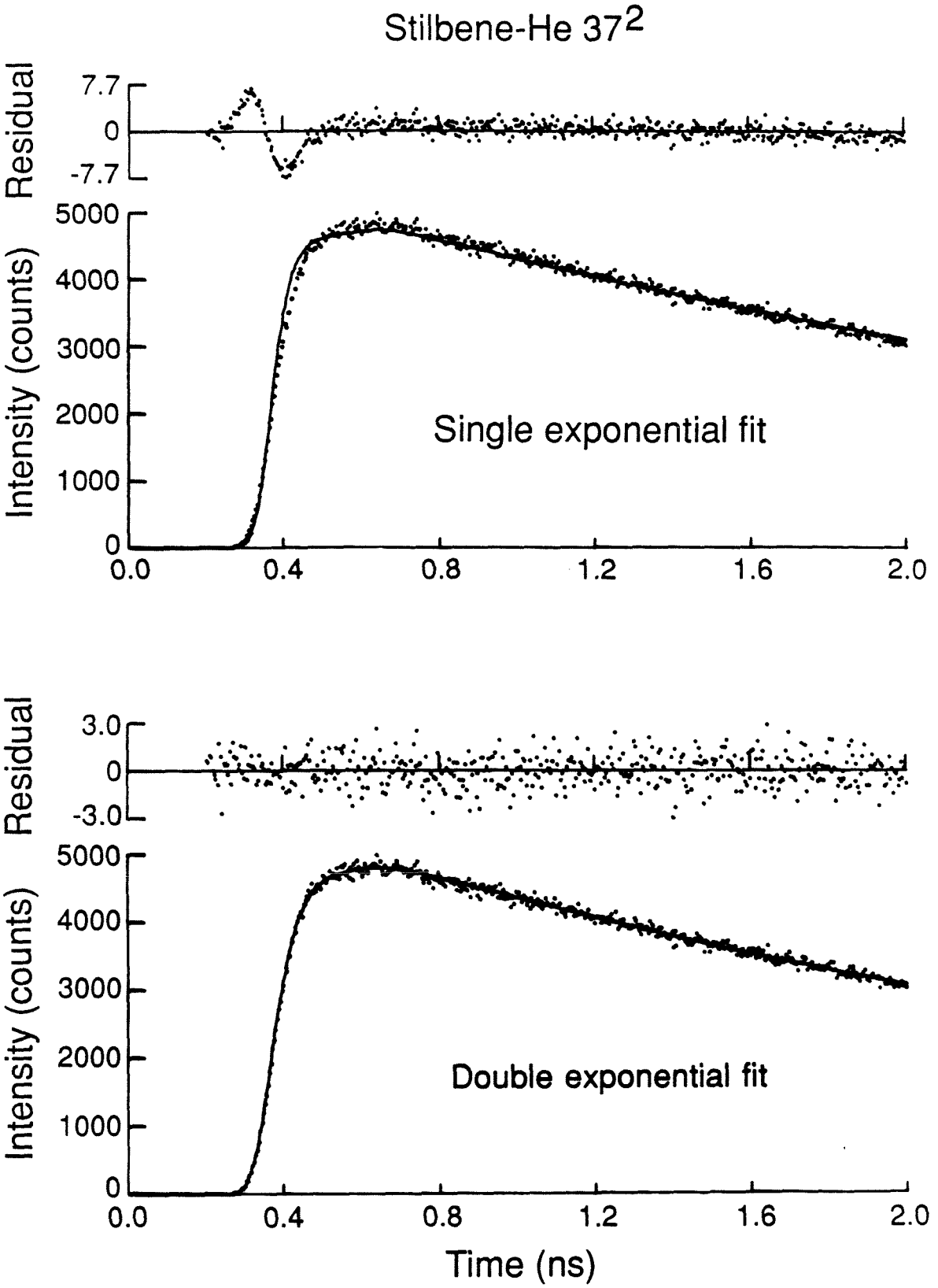
Stilbene-He 37²
Residual
7.7
0
-7.7
Intensity (counts)
5000
4000
3000
2000
1000
0
Single exponential fit
0.0
0.4
0.8
1.2
1.6
2.0
Residual
3.0
0
-3.0
Intensity (counts)
5000
4000
3000
2000
1000
0
Double exponential fit
0.0
0.4
0.8
1.2
1.6
2.0
Time (ns)

Figure 3

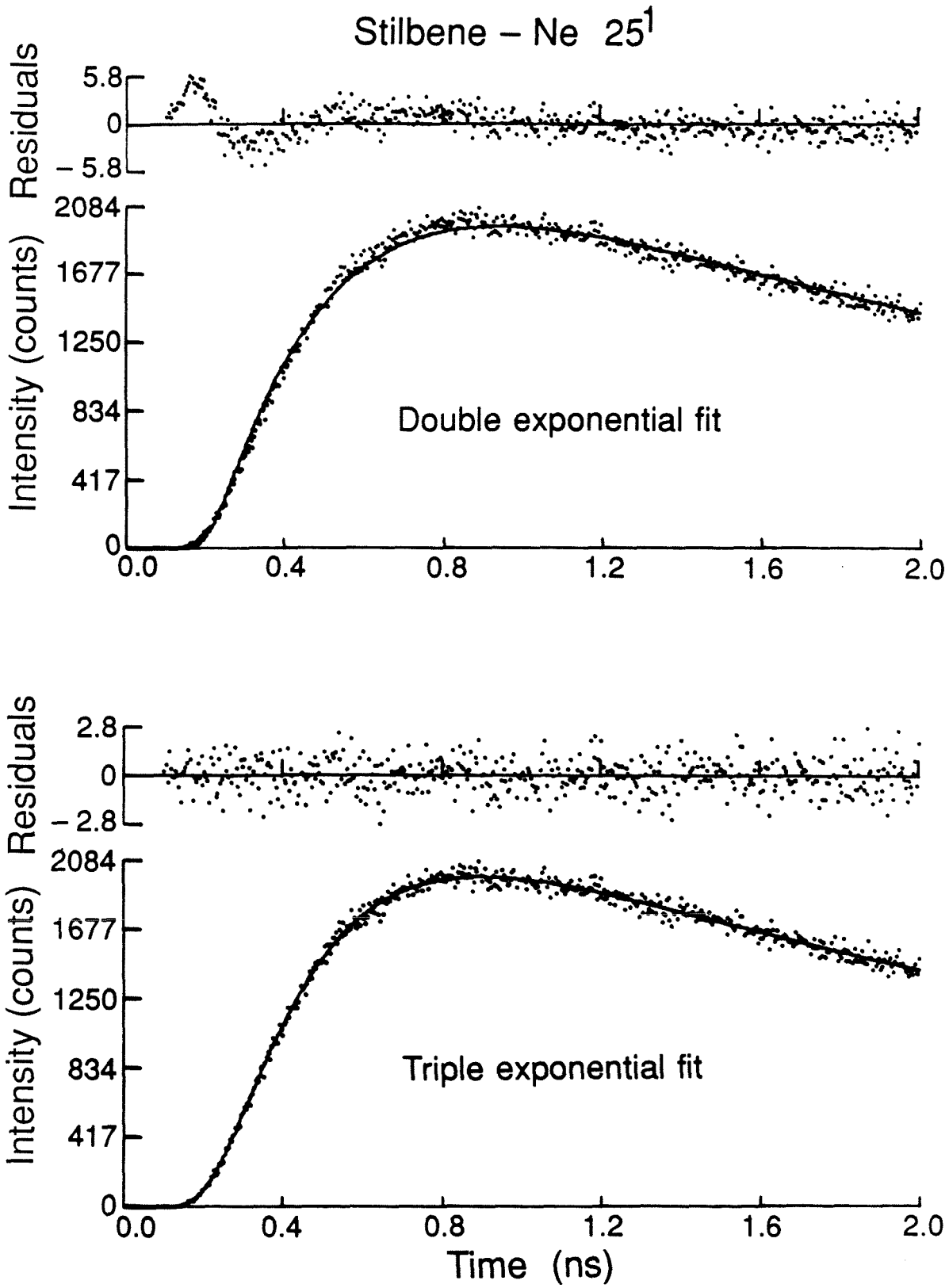
Stilbene – Ne 25[1]
Residuals
5.8
0
– 5.8
Intensity (counts)
2084
1677
1250
834
417
0
Double exponential fit
0.0
0.4
0.8
1.2
1.6
2.0
Residuals
2.8
0
– 2.8
Intensity (counts)
2084
1677
1250
834
417
0
Triple exponential fit
0.0
0.4
0.8
1.2
1.6
2.0
Time (ns)

Figure 4

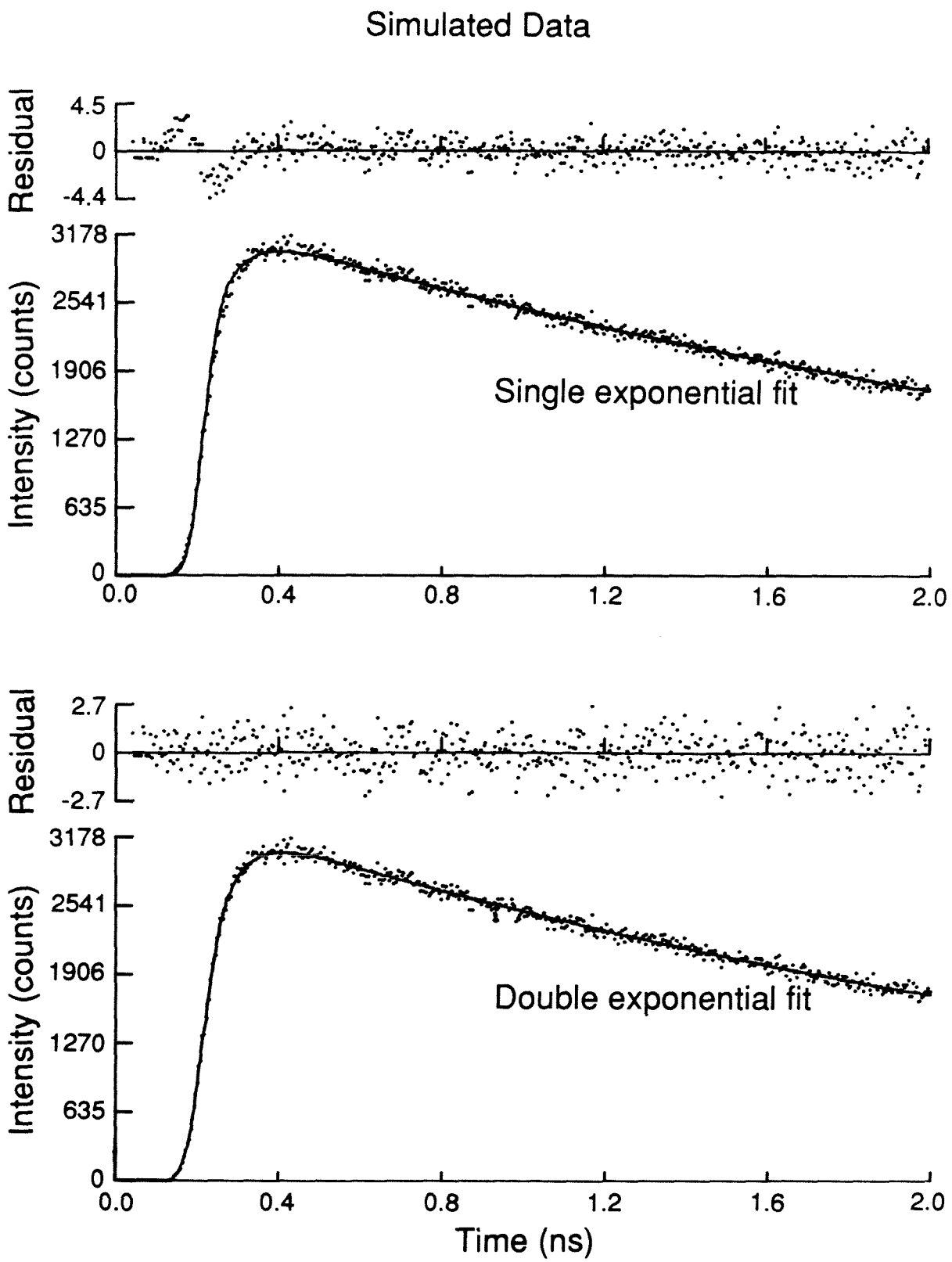
Simulated Data
Residual
4.5
0
-4.4
3178
2541
1906
1270
635
0
Intensity (counts)
Single exponential fit
0.0
0.4
0.8
1.2
1.6
2.0
Residual
2.7
0
-2.7
3178
2541
1906
1270
635
0
Intensity (counts)
Double exponential fit
0.0
0.4
0.8
1.2
1.6
2.0
Time (ns)

Figure 5

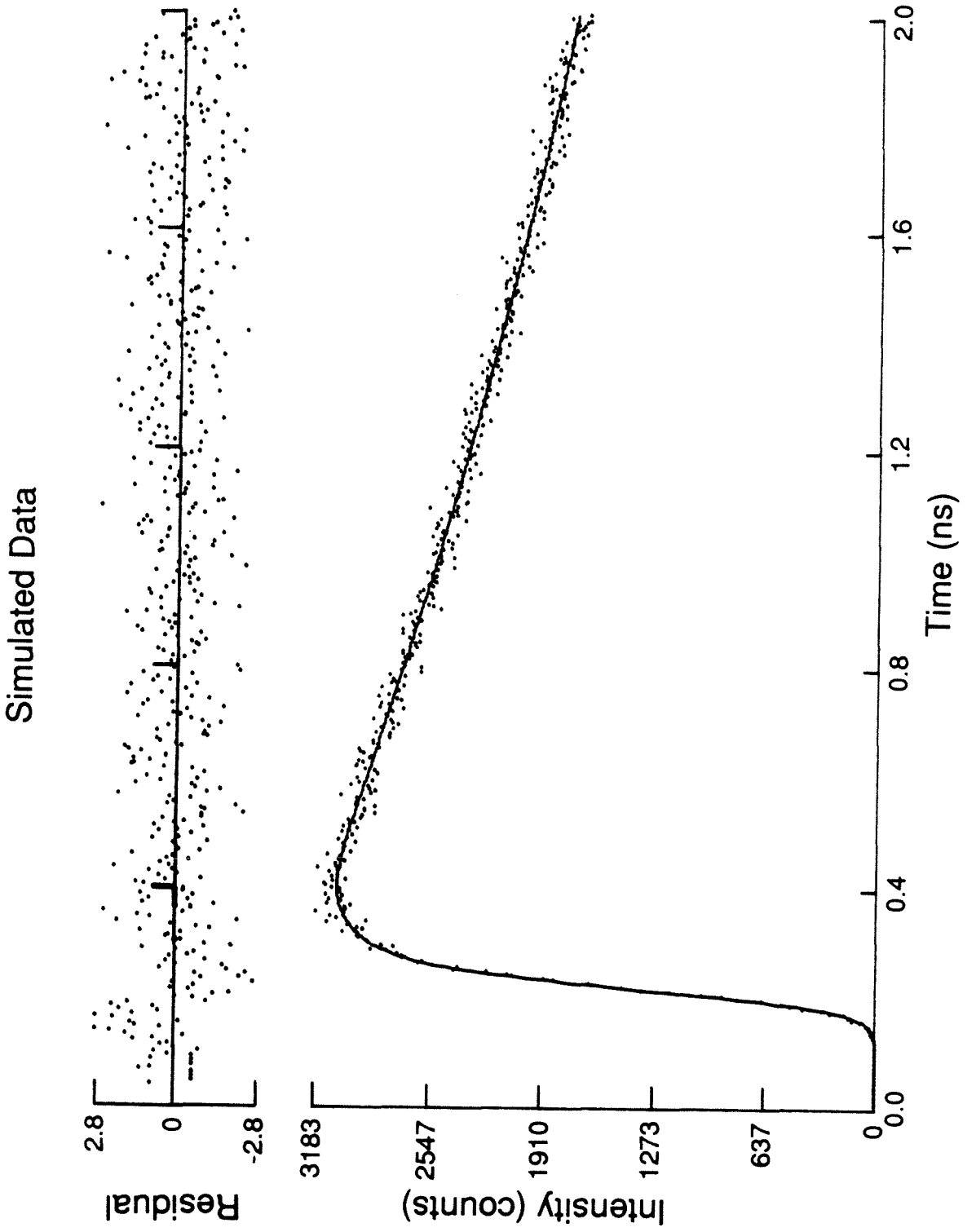
Simulated Data
Residual
2.8
0
-2.8
Intensity (counts)
3183
2547
1910
1273
637
0
0.0
0.4
0.8
1.2
1.6
2.0
Time (ns)

Chapter Four

Vibrational Predissociation in van der Waals Complexes of *t*-Stilbene

I. Introduction

In this chapter the results of time-resolved experiments on the dissociation of stilbene-He, stilbene-He_2, stilbene-Ne, and stilbene-Ar are presented and discussed in terms of the kinetic models developed in the last chapter. The magnitude of the measured lifetimes are then compared with theoretical expectations.

These complexes with stilbene are good choices for studying the dissociation of van der Waals systems for a number of reasons. The free-jet excitation spectra of trans-stilbene[1] and its van der Waals complexes[2] have been published. The spectrum of the helium complex shows a mode selective line broadening. The dynamics due to IVR[3] and other radiationless processes[4] have been throughly characterized. The stoichiometry and geometry of the complexes have been determined by sub-Doppler measurements[5] of the rotational constants of the isolated complexes. Finally, recent spectroscopic studies[6] have throughly characterized the low energy vibrational structure of t-stilbene.

The spectroscopy of the vibrational structure of jet-cooled S_1 trans-stilbene has been studied before.[1,6] The electronic origin is at 3101.4Å. To the blue there are major absorptions at 83, 95, and 198 cm^{-1} that are important in this work, hot band (sequence bands from thermally populated low energy levels) absorptions at 26 and 39 cm^{-1}, and combinations and overtones of all these bands. The upper levels reached in these transitions are assigned to ν_{25}, an in-plane bend at 198 cm^{-1}; ν_{36}, an out-of-plane bend of the phenyl rings with respect to the ethylene double bond at 35 cm^{-1}; and/or ν_{37}, an antisymmetric torsion of the phenyl rings around the ethylene-phenyl bond at 47.5 cm^{-1}.

The dynamics of jet-cooled S_1 stilbene has also been studied before, by time resolved spectroscopy. The fluorescence lifetime is 2.7 ns for every excitation

band below 1200 cm^{-1}, the barrier to isomerization.[4] IVR is not observed until 396 cm^{-1},[3b] and there is no evidence for any other radiationless transition.

Calculations[7] suggest the existance of two other vibrational modes with vibrational frequencies under 200 cm^{-1}, another torsion of the phenyl rings at 131 cm^{-1}, and an 88 cm^{-1} bend, neither of which have been observed experimentally.

The geometric structure of the complexes of stilbene studied in this work have been studied experimentally by measuring the purely rotational coherence[5] and the high resolution, rotationally resolved excitation spectrum.[8] For each 1:1 complex, the average position of the rare gas atom is between 3.0 and 3.45Å above the plane of one phenyl ring, displaced towards the center of the stilbene molecule between 0.1 and 0.5 Å.

II. Experimental

Complexes of stilbene-neon and stilbene-argon were formed in continuous supersonic jet expansions by passing ~100psi of a mixture of a small percentage of neon or argon in helium over stilbene heated to ~125°C in a Pyrex tube through a 50 to 80μ pinhole and into a vacuum chamber held at less than 1 milltorr. To form a sufficient concentration of stilbene-helium, it was necessary to increase the backing pressure to as high as 800psi of helium and to use a stainless steel high pressure nozzle assembly with a 25μ pinhole.

The complexes formed in these expansions were excited with tunable UV pulses of light ~ 15 ps (fwhm) long and ~ 2 cm^{-1} (fwhm) broad. These pulses were the doubled output of a cavity-dumped dye laser (R6G in ethylene glycol) synchronously pumped by a mode-locked Ar^+ laser.

The laser-induced fluorescence from the sample in the jet expansion was focused onto the slit of a 1/2m monochromator, detected and time resolved

by either a Hamamatsu R1564U or R2287U microchannel plate photomultiplier tube with associated photon counting electronics. The system response function measured with the Hamamatsu R2287U was generally broader, but more stable in position and width than that of the R1564U. The temporal system response function was measured by moving the molecular beam nozzle assembly into the path of the laser beam and detecting the scattered light. This response function was generally recorded before and after each decay and usually had a full width at half maximum of about 80 ps.

III. Results

A. Complexes with Helium

Stilbene-He: Excitation bands corresponding to excited stilbene transitions in the stilbene-He complex have been observed 6 cm^{-1} to the red of the corresponding bare stilbene transition for each transition of the molecule.[2] Seven of these bands, all overtones and combinations of ν_{25}, ν_{36}, and ν_{37} have been studied in these experiments.

0_0^0 : The fluorescence spectrum of vibrationless S_1 stilbene has been observed[1] and assigned[6] as primarily involving progressions of ν_{37} built on each member of a progression in ν_{25}. The frequency of each member in the ν_{37} progressions, however, depend on the transition with which it combines, apparently because of the large anharmonicity of ν_{37}. The stilbene-He origin fluorescence spectrum is very similar. Each member of the ν_{25} progression is shifted 6 cm^{-1} to the red, just as the complex bands are shifted 6 cm^{-1} to the red in the excitation spectrum. The ν_{37} progressions, however, are shifted between 3 and 6 cm^{-1} to the red and have different intensity distributions.

The fluorescence decay is a fit by a single exponential, the lifetime of which is equal to the lifetime of bare stilbene at this energy (2.7 ns).[4] Time resolved

polarization anisotropy experiments identify the emitter as stilbene-He.[5] Thus, exciting the vibrationless complex, no unusual dynamical behavior is observed.

83 and 95 cm^{-1}: Figure 1 shows the fluorescence spectra from the S_1 + 83 and the S_1 + 95 cm^{-1} vibrational levels of the complex and from exciting the red and blue edges of those bands. In both cases, the minor product is produced by loss of one quantum of ν_{37} and is formed unresolvably fast. The vibrationless stilbene is formed in 42 ps after exciting the complex at 95 cm^{-1} (see again Figure 2 in Chapter 3) and in 36 ps after exciting the complex at 83 cm^{-1}, independently of the precise excitation wavelength. The rises in these temporal data are compared with each other in Figure 2.

198 cm^{-1}: The complex 198 cm^{-1} absorption band overlaps with the bare stilbene 2 x 95 cm^{-1} band. Dispersed fluorescence spectra recorded under identical conditions except for the backing pressure of the molecular beam are shown in Figure 3, traces a and b. None of the bands which result from exciting the complex (those that grow at higher backing pressures) can be assigned to known S_1 states.[10,2c] The fluorescence intensity from various weak bands, including the resonant band at the laser wavelength, decay with a 159 ps lifetime and various stronger bands have that risetime, with no resolvable third component (Figure 4).

280 and 292 cm^{-1}: These broad[2] absorption bands are assigned as the combinations 198 + 83 cm^{-1} and 198 + 95 cm^{-1}. Both complex bands overlap with bands in bare, vibrationally cold stilbene. Figure 5 shows the fluorescence spectra of these overlapping bands at 280 cm^{-1} with backing pressures of 600 and 200 psi helium, a normalized difference spectrum, and a spectrum of bare stilbene at 198 cm^{-1}. It is evident that the bands due to absorption of the complex are from bare stilbene in the 198 cm^{-1} state. From the complex ex-

cited to 280 cm^{-1}, that single product is formed in $\sim$ 18 ps. As discussed in Chapter 3, the limit of the temporal resolution is $\sim$ 20 ps. Figure 6 compares the residuals for the single exponential best fit and for the double exponential best fit for this data. Since no systematic error was observed in the convoluted rise of the fluorescent decays of resonantly excited bare stilbene when this data was measured, this is evidence for a fast rise in the fluorescence decay of the stilbene 25^1 formed. The vibrational product state distribution from the complex excited to 292 cm^{-1} depends on the precise excitation wavelength, as at 95 cm^{-1}. Product formed by the loss of a single quantum of ν_{37} is formed unresolvably fast while stilbene at 198 cm^{-1} is formed in $\sim$ 22 ps.

396 cm^{-1}: The complex 25_0^2 absorption band overlaps with the bare stilbene $25_0^1 37_0^4$ band (Figure 7). As at 198 cm^{-1}, the emission bands due to the the complex cannot be assigned to known complex or stilbene bands. The resonant complex fluorescence decays in 58 ps and several of the more intense complex lines have the same risetime with no apparent third component (Figure 8).

Stilbene-He_2: Bands in the excitation spectrum of stilbene-He_2 have been identified[2] 12 cm^{-1} to the red of the corresponding stilbene transitions at the origin and the fundamental and overtones of ν_{25}. Such transitions have not been observed for stilbene transitions in the complex corresponding to combinations and overtones of ν_{36} and ν_{37}. The only stilbene-He_2 excitations studied are at 198 cm^{-1}, the stilbene ν_{25} band, and 396 cm^{-1}, its overtone.

198 cm^{-1}: The fluorescence spectrum of stilbene-He_2 at 198 cm^{-1}, not complicated by overlapping absorptions, is shown in Figure 9. Bands assigned to the major product, vibrationless stilbene, and the minor products, 36^1 and 37^1 stilbene, are indicatied in the figure along with the band due to resonant emission. A 90 ps decay of the initially excited state was measured as was a

well fit triexponential decay of the stilbene origin fluorescence (Figure 10). The triexponential included a decaying component with a 42 ps lifetime in addition to the 2.7 ns fluorescence decay and 94 ps risetime, with the amplitudes of the three components related to the measured lifetimes as was discussed in Chapter 3. However, this decay was equally well fit (as judged by the value of χ_r^2) as a biexponential with a 115 ps risetime, but a 30 ps shift with respect to the measured response. A similar shift was found when triexponentials with those parameters were simulated and fit as biexponentials as discussed in Chapter 3.

The measured decay of fluorescence from the state 37^1 depends markedly on the spectral resolution, presumably because of underlying complex emission. At high resolution (8 cm^{-1}) a low signal-to-noise measurement of the time-resolved fluorescence from this level is best fit with a partial risetime (the ratio of the amplitude of the two components is $\sim$-0.4 rather than -1.0) of 140 ps. Figure 11 shows this data and the residuals of the best biexponential fit with a 90 ps risetime and the best biexponential fit.

396 cm^{-1}: The fluorescence spectrum of stilbene-He_2 excited to 25_0^2, again not complicated by overlapping bands, is shown in Figure 12. Most of the fluorescence is from stilbene excited with one quantum of ν_{25} which is formed with the same rate as the decay rate of the resonant fluorescence, 1/34 ps, with no detectable third component in the temporal profile (see data with fast decay and fast rise in Figure 13). Vibrationless stilbene, a minor product, was previously reported and fit as a biexponential with a 118 ps risetime.[10] We have repeated this measurement to a signal-to-noise more than three times larger and have fit the data, not as a biexponential, but as a triexponential with rising components of both 48 and 243 ps (see data labeled "slower rise" in Figure 13.) While it is doubtful that we have accurately resolved the time evolution of this

weak, broadened band in the fluorescence spectrum, details of the dynamics leading to origin stilbene can still be deduced from the presence of the strong, long risetime. (Emission from the product $25^1 37^1$ is far too weak to accurately measure the time evolution of formation for that state.)

B. Complexes with Neon and Argon

Excitation spectra[2] and rotational constants[5] of stilbene-neon and stilbene-argon have been measured. Transitions in the complex to the vibrationless and 198 cm^{-1} states are observed 16 and 63 cm^{-1} to the red of the corresponding stilbene transition for the neon and argon complexes, respectively. An additional band in the spectrum of the argon complex at -40 cm^{-1} with respect to the stilbene transitions is assigned to a transition in the van der Waals modes.[2c]

Stilbene-Ar

198 and 396 cm^{-1}: The stilbene-argon absorptions at 198-63, 198-40, and 396-63 cm^{-1} with respect to the stilbene origin all give rise to broad, red-shifted, origin-like fluorescence (Figure 14). The resonant fluorescence decays in 250, 159, and 60 ps, respectively, for these bands, and double-exponential decays with the same fast risetimes are measured in the broad part of the spectrum (see Figure 15).

594 cm^{-1}: At this energy the primary product is bare, vibrationless stilbene (Figure 16). At low (8Å) resolution, the time evolution of the fluorescence from that product is well fit by a biexponential with a partial risetime (the ratio of the amplitudes is -0.7 rather than -1.0) of 125 ps (Figure 17). An "internal timing"[11] analysis of the fluorescence spectrum (i.e., relating fluorescence yields to decay lifetimes) indicates that the initial stilbene-Ar vibrational state population decays in <16 ps.

Stilbene-Ne

198 cm^{-1}: The spectrum from the neon complex excited to the level 25^1 shows that the primary product is vibrationless stilbene and that stilbene in the states 36^1 and 37^1 are minor products (Figure 18). The resonant fluorescence from the complex decays in 233 ps (Figure 19). The emission from the bare, vibrationless stilbene is well fit as a triexponential with a 233 ps rising component and a 63 ps decaying component in addition to the long, fluorescence decay (Figure 19 and Figure 3 of Chapter 3). Amplitudes of the the three components are related to the measured lifetimes as was discussed in Chapter 3.

As is the case with the minor products of other complexes, it is difficult to spectrally resolve the weak emission of minor products and consequently the measured kinetic parameters depend on the spectral resolution. The most highly resolved (spectral resolution, R = 0.48 Å) emission from bare stilbene in the 37^1 state could be fit as a double exponential with only a 207 ps risetime. With less spectral resolution (R = 0.96 Å), the fluorescence from this state was fit with a partial risetime (i.e., the ratio of amplitudes was -0.5, not -1.0) of 195 ps. These data curves are plotted in Figure 20 and show the change in the rising component of this emission as the spectral resolution is changed. Since product fluorescence should rise no faster than the decay of the initially excited state (233 ps), it appears this emission is still insufficiently resolved to measure kinetic parameters for this state.

396 cm^{-1}: The fluorescence spectrum of stilbene-Ne excited to the second overtone of ν_{25} is shown in Figure 21. Bands due to vibrationless stilbene and stilbene 25^1 are marked. Temporal data for some of the more intense bands in the spectrum were recorded with low (4.8-1.6 Å) resolution. All had partial risetimes of 116 ps, the same as the decay lifetime of the resonant fluorescence (Figure 22).

IV. Discussion

A. Separation of IVR and VP

The temporal data for stilbene-neon excited to 198 cm^{-1} offers the clearest and the most convincing proof we have that IVR is preceeding VP despite the fact that there is no hint of IVR in the time-integrated (i.e., spectral) results. A triexponential with clearly resolved lifetimes is measured in the fluorescence from the product stilbene, and a matching decay of fluorescence from the initially excited state is also observed. Sequential VP, of course, cannot account for the multistep dissociation of this 1:1 complex. From this data we can identify 255 ps (correcting for k_f) as the total rate of dissipative IVR from the initially excited chemical vibrational level of the complex and 65 ps (correcting for k_f) as the total VP rate of the intermediate state that precedes the formation of vibrationless stilbene. In the next two sections we will discuss these two rates in some detail, comparing them with theoretical expectations.

B. IVR and the van der Waals Vibrational State Density

In bare stilbene, dissipative IVR is not observed until 1237 cm^{-1} and no IVR is observed at only 198 cm^{-1} of excess energy. It is perhaps surprising that the weak binding ($D_0 \leq$ 198-48 cm^{-1}) of a rare gas atom can affect the relaxation dynamics of this in-plane vibrational mode so drastically.

Two parameters are necessary to quantify IVR, coupling strengths and vibrational state densities. Felker et al.[3] have directly measured coupling strengths of ~1.0 GHz in bare stilbene by measuring beat frequencies in the fluorescence decays of single vibrational levels. The calculated vibrational state density at energies where dissipative IVR is observed is $>$ 150 per cm^{-1} per symmetry class (accounting for the symmetry restrictions in the coupling). To discuss the role of IVR in these experiments, therefore, we need to consider the effects of

the van der Waals modes on the vibrational state density of these complexes. Our method is similar to Ewing's.[12c]

Models of the van der Waals potential between rare gas atoms and aromatic molecules have exclusively been based on two body interaction potentials between the rare gas atom and each atom of the aromatic molecule.[13] Baskin and Zewail have[5a] used structural data on these complexes to evaluate approximately the validity of these calculated potentials in determining rotational constants. Qualitative agreement is found between the experimentally determined structure and that calculated from a sum of two-body potentials in which the aromatic and aliphatic carbons are characterized by different parameters. We used this potential to calculate the density of van der Waals vibrational states. These potentials have double minima, one above each phenyl ring, with a substantial barrier ($\sim$1/4 D_e) between them.

The three coordinates involving motion of the rare gas atom were assumed to be the stretching motion of the atom towards and away from the phenyl ring, a bending motion parallel to the line on which the double minima occur and a bending motion perpendicular to that line. Plots of the vibrational potential energy along these three coordinates are shown in Figure 23 for stilbene-Ar along with the fits of these curves to a Morse potential and two $1/\cosh^2$ x potentials, respectively, each of which is determined by a well depth and a range parameter.[14] Only a single well of the double minimum potential was fit for the purpose of calculating the vibrational state density. Vibrational frequencies and anharmonicities for these van der Waals modes were then calculated from the range parameter of the fit and the experimental upper limit of the dissociation energy. These parameters are listed in Table 1.

Treating each coordinate as separable would lead to dissociation only when

the energy in any single coordinate exceeded D_0. By adding appropriate cross-anharmonicities (e.g., $g_{xy} = 2\sqrt{(g_{xx}g_{yy})}$, where g_{xx}, for example, is the anharmonic constant for the x-coordinate), however, the expression for the van der Waals vibrational energy can be made to reflect dissociation whenever the total energy exceeds D_0. To calculate the energies of the different van der Waals modes, therefore, we used the expression

$$\begin{aligned} E_{vdw} = {} & \omega_x(n_x + \frac{1}{2}) + \omega_y(n_y + \frac{1}{2}) + \omega_z(n_z + \frac{1}{2}) \\ & - g_{xx}(n_x + \frac{1}{2})^2 - g_{yy}(n_y + \frac{1}{2})^2 - g_{zz}(n_z + \frac{1}{2})^2 \\ & - g_{xy}(n_x + \frac{1}{2})(n_y + \frac{1}{2}) - g_{xz}(n_x + \frac{1}{2})(n_z + \frac{1}{2}) - g_{yz}(n_y + \frac{1}{2})(n_z + \frac{1}{2}) \end{aligned}$$

where the ω's are the vibrational frequencies, the g's are the anharmonic constants, and the n's are vibrational quantum numbers. This expression was used to directly count the number and density of bound levels in the van der Waals well.

Knowing the vibrational level structure of stilbene from earlier spectroscopic work and normal mode calculations and having determined the approximate vibrational state density for the van der Waals modes, Figure 24 shows the vibrational energy level diagram of stilbene below 200 cm^{-1} and the resultant total density of bound vibrational states as a function of excess vibrational energy for stilbene-He. The total vibrational state density of stilbene-neon and stilbene-argon were calculated in the same way and plots of those functions are shown in Figure 25.

The vibrational state density of stilbene-neon at 198 cm^{-1}, 330 per cm^{-1} can be compared to the state density at which dissipative IVR is observed in bare stilbene (150 per cm^{-1}). According to the theoretical work of Lahmini[15], the intramolecular dephasing of a bound state (as is the case for IVR) approaches

a single exponential form more closely as the number of coupled levels increases and the decay rate of the dephasing is given by a golden-rule type expression. Thus, comparing state densities for the bare molecule and the complex and assuming for the moment that the coupling strengths are similar ($\sim$1.0 GHz^3), we would expect the IVR dephasing in the complex to be more nearly dissipative (i.e., no or fewer recurrences) and the decay rate to be $\sim 2\pi\bar{V}^2\rho = 1/14$ps. Thus, the IVR observed in stilbene-neon is qualitatively consistent with previous observations for these approximate values of V and ρ.

C. Vibrational Predissociation-Comparison with Theory

From the temporal profile of the fluorescence from the dissociated vibrationless stilbene formed when stilbene-neon is excited to 198 cm^{-1}, we can identify 65 ps (corrected for k_f) as the total VP rate from some redistributed level at 198 cm^{-1}. The decay of the initial state identifies 255 ps as the IVR rate. We can compare this experimental rate with rates calculated according to statistical rate theories[16] and according to the momentum-gap law.[12]

Classical RRK theory gives

$$k = A\left(\frac{E - D_0}{E}\right)^{S-1}$$

where E is the energy of the undissociated molecule, D_0 the dissociation energy, S the number of oscillators in the molecule, and A is the frequency of the van der Waals stretch (e.g., the reaction coordinate). Taking the IVR to be complete so that all eight modes up to and including the 198 cm^{-1} mode take part in the dissociation, and taking 150 cm^{-1} as D_0, we calculate a predissociation lifetime at 198 cm^{-1} of 20 ns for stilbene-Ne, orders of magnitude different from the experimental value. The equation above can be derived by assuming that a classical treatment of harmonic vibrations is adequate to calculate vibrational state densities. The corresponding state density for stilbene-Ne at 198 cm^{-1} is

given by

$$\frac{E^{S-1}}{(S-1)!\prod_{i=1}^{S} h\nu_i} = 0.40cm^{-1}$$

where E and S are as before, h is Planck's constant, and ν_i is the frequency of the i^{th} oscillator. Comparing this value of the vibrational state density with the value calculated by directly counting anharmonic levels, it is clear that the classical treatment of molecular vibrations is completely inappropriate for discussion of the dissociation of van der Waals complexes at low energies.

RRKM rate constants are given by the expression

$$k(E) = \frac{N^{\dagger}(E)}{\hbar\rho(E)}$$

where $k, E, \hbar$, and ρ are as before and $N^{\dagger}$ is the number of levels in the transition state. The van der Waals stretching mode of the stilbene complex was assumed to be the reaction coordinate. For simplicity, all other modes were assumed the same in the transition state as in the excited complex. Harmonic frequencies of 40.0, 9.0 and 8.0 were used in the calculation for the van der Waals modes (compare with Table 1). The RRKM rates were calculated by directly counting harmonic vibrational levels as discussed by Khundkar *et al.*[16b] Some rates were calculated with anharmonicities included for the van der Waals modes to evaluate the accuracy of the calculation.

The VP lifetime for stilbene-neon at 198 cm^{-1} calculated from RRKM theory using a harmonic count of vibrational levels is 75 ps and increases to 97 ps when anharmonic levels are counted, taking D_e (which determines the anharmonicities in this model) to be 250 cm^{-1}. Including cross-anharmonicities also, but counting only the bound states below the dissociation limit, the calculated lifetime is 239 ps.

Our experimental VP rate of 65 ps can also be compared to theoretical expectations according to the momentum-gap law. As developed by Ewing,[12] this law can be derived by separating the matrix element in Fermi's Golden Rule into a factor involving the van der Waals states and a factor involving the chemical vibrations. For a slowly changing van der Waals potential, the van der Waals factor in the matrix element is a Frank-Condon overlap integral between the initial van der Waals state and the outgoing plane wave function for the predissociated atom. The factor involving the chemical vibrations in the matrix element is similar to an infrared transition matrix element and is fully allowed for $\Delta\nu = 1$, and less allowed for $\Delta\nu = 2,\ 3$, etc. Those different factors, momentum gap and vibrational changes, determine the momentum-gap rate, but the relative importance of each cannot be judged without explicitly calculating matrix elements and overlap integrals for the potential energy surface of the complex. For an initial state with excited van der Waals modes (particularly the stretch) however, Ewing[12c] has shown that the energy gap may be compensated for, in a sense, since the greater number of nodes in the van der Waals vibrational wavefunction can maximize the overlap integral with a relatively high energy plane wave eigenfunction for the translational state of the final fragment.

Ewing has simplified these results to give[12c]

$$k_{vp} = 10^{13} e^{[-\pi(\Delta n_t + \Delta n_v)]}$$

$$\Delta n_t = \frac{\sqrt{2\mu\Delta E}}{2a\hbar} - v_z$$

where Δn_v is the change in chemical vibrational quantum numbers, Δn_t is the change in the "translational quantum number," μ is the reduced mass of the fragments, ΔE is the final relative translational energy of the fragments, a is the Morse potential range parameter, $\hbar$ is Planck's constant, and v_z is

the vibrational quantum number for the van der Waals stretching mode. Since 37^1 stilbene is a product of the dissociation of stilbene-neon 25^1, ΔE can be no less than 48 cm^{-1} if all the available energy goes into translation. Taking this value of ΔE, the range parameter ($1.3 Å^{-1}$) calculated from the van der Waals potential and taking $\Delta n_v = 1$ since low Δn channels are favored in the experimental product state distributions, this equation gives VP rates of between 21 ns and 3.1 ps depending on whether the van der Waals stretching mode is in the $v_z = 0,\ 1,\ 2,\ or\ 3$ state. If ΔE=10 cm^{-1}, these same rates vary between 445 and 6 ps. Clearly, even the simplest calculation of the rate according to the momentum-gap law is not accurate without more knowledge of the intermediate state. General statements will be made, however, in a later section when different rates are compared.

D. Product State Distributions

When more than one product is formed in the dissociation, the experimental PSDs give information on rate processes that occur in parallel. According to the model presented in Chapter 3, the time resolved data can determine whether the parallel process occurs in the IVR step or the VP step. If different VP lifetimes are measured, as is the case for stilbene-He_2 25^1 and 25^2, then different intermediate states are formed in the IVR step, are predissociating independently, and the PSD can be used to calculate individual IVR rates. Conversely, if identical triexponentials are measured for different final states, it is likely that the different products are formed in the VP step and the PSD would be determined by the individual VP rates (since, *a priori*, one would not assume identical VP rates from different intermediate states).

Different VP rates were resolved for stilbene-He_2 25^1 and 25^2. For stilbene-Ne and stilbene-Ar the signal was insufficient to accurately measure temporal

data for minor products at the high spectral resolution necessary to isolate individual bands. Assuming, therefore, similar dissociation paths, i.e., IVR to different states which VP independently, the IVR rates for all of these excitations were calculated by taking the relative emission intensities to be proportional to the relative rates while the total rate (including a fluorescence rate assumed to be the same as that of the bare molecule) was measured. These individual IVR rates are shown in Table 2. This table does not include stilbene-He data since the PSDs observed from that complex either depended on the precise excitation frequency within the inhomogeneous absorption band or could not be assigned.

E. Comparison of Linewidths and Measured Lifetimes

The stilbene-He complex is the only large polyatomic-rare gas van der Waals complex that has been studied by measuring both excitation linewidths[2] and by directly time-resolving the population of reactants and products. The bands in the excitation spectrum of the stilbene-Hecomplex at 83 and 95 cm^{-1} are unusually broad compared to other complex bands, having a full width at half maximum of $\sim$3 cm^{-1}. If homogeneous, this width corresponds to a lifetime of $\sim$ 2ps. In these time resolved experiments, however, we measured product rise times of 36 and 42 ps, respectively, for those two transitions. It is apparent that the broad absorption lines do not accurately reflect the dissociation rates.

Originally, both our work[10] and the work of Zwier and co-workers[2] suggested that the broad lines in the excitation spectrum could be due to fast IVR out of the initially excited state, preceeding dissociation. However, the dependence of the PSD on the precise excitation wavelength reported here for the 83 and 95 cm^{-1} bands and reported by Zwier[2c] for the 95 cm^{-1} band show that the absorption bands are inhomogeneously broadened. The identity of the states within the inhomogeneous width and the time scale for energy flow between them

is still not clear.[17]

F. Mode Specificity

In these experiments, we have directly observed a vibrational mode dependence in the unimolecular dissociation of a large polyatomic system, stilbene-He. The dissociation from modes involving ν_{36} and ν_{37} is considerably faster than from modes of the higher energy vibration, ν_{25}.

A number of possible explanations for this behavior can be considered:

(1) The IVR rate is mode dependent because changes in the displacements of the normal coordinates of ν_{36} and ν_{37} cause large changes in the van der Waals potential energy (these bending coordinates in stilbene have large components along the van der Waals stretch). Weber and Rice[18] hypothesize that this is the reason for the unusual activity of mode 16a in the dynamics of S_1 tetrazine-Ar. As in that case, the *vibrational* shifts of complex bands including ν_{36} and ν_{37} in the excitation spectrum[2b] are different from the vibrational shifts of other bands, though the difference is small.

(2) The VP rate is mode dependent because of a low energy gap propensity. The rate from mode 25 could be slow compared to the rate from the lower energy modes because the stilbene molecules excited to the unassigned product mode must be translationally hot to compensate for the large gap in energy (or relative momentum) between the initial and final states of the reaction.

(3) Both ν_{36} and ν_{37} and the van der Waals vibrations have large amplitudes compared to most chemical vibrations. This will have the effect of increasing the coupling strength and making higher-order anharmonicities more important for both IVR and VP.

(4) The similarity of the frequencies of ν_{36} and ν_{37} to the van der Waals stretching mode would decrease $\Delta\nu_n$ and thus increase the strength of the

interaction of these modes for either the IVR or VP.

The nature of these levels in the neon and argon complexes is more poorly understood. Zwier reported[2a] the absence of bands involving ν_{36} and ν_{37} in the excitation spectra of these complexes, suggesting they were so broadened by IVR that they could not be detected. This was consistant with our observation of weak, broad fluorescence, independent of the precise (i.e., ± 10 cm^{-1}) excitation wavelength in the region of the excitation spectrum where these bands would be expected. Zwier's latest work,[2c] however, tentatively identifies narrow bands with unusual shifts with these transitions.

Mode specific rates are also observed in two cases for the VP rates of different products from different, isoenergetic, redistributed levels of the complex. Stilbene-He_2 excited to 25^2 yields 25^1 and 0^0 stilbene with different rates. According to the kinetic scheme in Chapter 3, these different rates reflect different VP rates from different intermediate states. Since the identity of these intermediate states is unknown, however, these rates cannot be compared even qualitatively with predictions according to the momentum gap law, as has been discussed for stilbene-Ne 25^1. In contrast to the two VP rates measured for stilbene-He_2 25^2, it is interesting that the higher energy product of the dissociation of stilbene-He_2 25^1 is formed more slowly than the lower energy product. In both cases, the product formed with the faster rate differs from the initial state by the smaller number of vibrational quanta, not by the smaller energy gap.

G. Other Complexes

The results for the other excitations and other clusters support these conclusions about IVR and VP in the dissociation process directly or indirectly. For example, the data for the three excitations of ν_{25} (25_0^1, 25_0^2, and 25_0^3) in stilbene-

Ar strongly suggest the dissociation is a two-step process, that IVR precedes VP. At 25^1 and 25^2, rates of irreversible IVR of 1/250 ps and 1/60 ps, respectively, are measured from the broad fluorescence (itself the *spectral* signature of dissipative IVR). At 25^3, where the IVR rate is apparently too fast to resolve, narrow bands assigned to bare, vibrationless stilbene have a 125 ps rise which we attribute to the total VP lifetime from some redistributed level. Both the RRKM and the momentum gap theories predict a longer decay lifetime for this reaction compared to the decay lifetimes calculated for stilbene-Ne 25^1. These lifetimes are listed in Table 3.

For the 25^2 excitation of stilbene-Ne, only one rate, the decay rate of the initially excited state, was actually resolved. A comparison of this rate with other IVR rates for the neon and argon complexes studied and the fact that the calculated RRKM rate (Table 3) is significantly faster than the RRKM rate for 25^1 excitation suggests that the dynamics of this level is only faster than the dynamics for the 25^1 level, not different. Note also that the congestion in the red part of the dispersed fluorescence spectrum is likely to conceal any different behavior in the temporal profile of fluorescence from vibrationless stilbene.

For the 25^1 excitation of stilbene-He_2, not only was a triexponenetial decay of the fluorescence from vibrationless stilbene measured, but a different risetime was measured for the product 37^1 stilbene. Each of these observations is evidence for IVR preceeding VP.

The detailed dynamics from the different excitations of the stilbene-He complexes are the least clearly understood of the systems we have studied. Without knowing the decay rate of the initially excited state, it is not clear whether or not IVR is occuring from these levels. One possibility is that the states which predissociate to form 37^1 and 0^0 stilbene are separated by $\sim$1 cm^{-1} but

both derive their absorption strength from the zero-order state, stilbene-He 37^2. In this case, IVR would necessarily precede VP with our laser. On the other hand, recent work by Zwier[17] on stilbene-H_2 and p-methylstilbene-H_2 suggests that the broadening may be from unresolved vibrational structure in the van der Waals modes. In this case, the initially excited states could independently predissociate, without IVR, also consistant with our results.

Excitation of 25^1 and 25^2 in the stilbene-He complex yields an unassignable spectrum with no third component in the temporal profile of the fluorescence. However, very fast VP rates are calculated (see Table 4) for this complex according to both RRKM theory (because of the small value of D_0) and according to the momentum gap law (because of the small reduced mass of the complex). It is doubtful that the decay rates measured are due to direct VP from the initially excited chemical vibrational level when those channels are not observed for the other complexes studied.

V. CONCLUSIONS

This chapter includes experimental results of the direct, time-resolved measurements of the population of both the products and initial states in the unimolecular dissociation of the van der Waals complexes of stilbene with helium, neon, and argon excited to combinations and overtones of ν_{25}, ν_{36}, and ν_{37}.

We have studied the time resolved dynamics of 14 excited vibrational levels of these complexes. The time-resolved data for the complexes stilbene-Ne, stilbene-Ar, and stilbene-He_2 clearly show that vibrational redistribution precedes vibrational predissociation even though there is no evidence of redistribution in the spectral data. We have measured fluorescence spectra and lifetimes for six levels of stilbene-He, but have not been able to resolve any experimental evidence for a multistep dissociation for that complex. The measured lifetimes

do show, however, that the dissociation for that complex is highly mode-specific.

Dissipative IVR is observed at much lower energies in the complexes than in the bare molecule. A calculation of the density of vibrational states for the van der Waals modes can account for this observation when anharmonicities are included for the van der Waals modes.

We report five vibrational predissociation lifetimes from unknown, redistributed levels of the excited complex. In each case, the lifetime according to simple momentum gap law calculations depends so strongly on the unknown, final translational energy of the fragments and the (unknown) level of chemical and van der Waals vibrational excitation in the intermediate state, that no conclusion on the validity of the momentum gap law can be made. In two cases, different VP lifetimes were measured for different redistributed levels of a particular excitation. In each case the product formed more rapidly differed from the initial state by a smaller number of vibrational quanta, not a smaller energy gap.

Predissociation rates calculated according to RRK theory are off by orders of magnitude because of errors in counting states. Statistical RRKM theory, of course, cannot account for different VP rates to different product states from isoenergetic levels. Simple RRKM calculations do, however, account for the magnitude of the observed VP rates for the major channels of the dissociation for stilbene-He_2 25^1, stilbene-Ne 25^1, and stilbene-Ar 25^3. For other excitations where dissociation occurs, we observe no resolvable VP rates, which is also consistant with the calculated RRKM rates. We emphasize that the agreement with RRKM is only for certain *vibrational predissociation* rates. IVR was often found to be the slower step.

REFERENCES

1. J. A. Syage, P. M. Felker, and A. H. Zewail, J. Chem. Phys. **64**, 3266 (1976).

2. (a) T. S. Zwier, E. Carrasquillo, M., and D. H. Levy, J. Chem. Phys. **78**, 5493 (1983);
   (b) C. A. Taatjes, W. B. Bosma, and T. S. Zwier, Chem. Phys. Lett. **128**, 127 (1986);
   (c) D. O. DeHaan, A. L. Holton, and T. S. Zwier, J. Chem. Phys. **90**, 3952 (1989).

3. (a) P. M. Felker, W. R. Lambert, and A. H. Zewail, J. Chem. Phys. **82**, 3003 (1985);
   (b) J. S. Baskin, unpublished work.

4. J. A. Syage, P. M. Felker, and A. H. Zewail, J. Chem. Phys. **81**, 4706 (1984).

5. (a) J. S. Baskin and A. H. Zewail, J. Phys. Chem., in press (1989);
   (b) P. M. Felker and A. H. Zewail, J. Chem. Phys. **86**, 2460 (1987);
   (c) J. S. Baskin, P. M. Felker, and A. H. Zewail, J. Chem. Phys. **86**, 2483 (1987).

6. (a) T. Suzuki, N. Mikami, and M. Ito, J. Phys. Chem. **90**, 6431 (1986);
   (b) L. H. Spangler, R. van Zee, and T. S. Zwier, J. Phys. Chem. **91**, 2782 (1987).

7. A. Warshel, J. Chem. Phys. **62**, 214 (1975).

8. W. M. van Herpen, Ph.D. Thesis, Catholic University of Nijmegen (1988).

9. J. S. Baskin, D. H. Semmes, and A. H. Zewail, J. Chem. Phys. **85**, 7488 (1986).

10. D. H. Semmes, J. S. Baskin, and A. H. Zewail, J. Am. Chem. Soc. **109**, 4104 (1987).

11. (a) D. V. Brumbaugh, J. E. Kenny, and D. H. Levy, J. Chem. Phys. **78**, 3415 (1983);
(b) K. W. Butz, D. L. Catlett, G. E. Ewing, D. Krajnovich, and C. S. Parmenter, J. Phys. Chem. **90**, 3533 (1986);

12. (a) G. E. Ewing, J. Chem. Phys. **72**, 2096 (1980);
(b) G. E. Ewing, Faraday Disc. Chem. Soc. **73**, 325 (1982);
(c) G. E. Ewing, J. Phys. Chem. **90**, 1790 (1986).

13. S. Leutwyler and J. Jortner, J. Phys. Chem. **91**, 5558 (1987).

14. I. I. Goldman and V. D. Krivchenkov, *Problems in Quantum Mechanics* (Pergamon, London, 1961).

15. F. Lahmani, A. Tramer, and C. Tric, J. Chem. Phys. **60**, 4431 (1974).

16. (a) P. J. Robinson and K. A. Holbrook, *Unimolecular Reactions*, (Wiley, New York, 1972);
(b) L. R. Khundkar, R. A. Marcus, and A. H. Zewail, J. Phys. Chem. **87**, 2473 (1983).

17. See, however, T. S. Zwier, J. Chem. Phys. **90**, 3967 (1989).

18. P. M. Weber and S. A. Rice, J. Phys. Chem. **92**, 5470 (1988).

Table 1

Calculated van der Waals frequencies and anharmonicities

(in wavenumbers)

Stilbene-Ar

ω_x=8.06	g_{xx}=0.032	g_{xy}=0.073	
ω_y=9.21	g_{yy}=0.042	g_{xz}=0.334	D_0=478[a,b]
ω_z=42.00	g_{zz}=0.87	g_{xy}=0.381	

Stilbene-Ne

ω_x=6.34	g_{xx}=0.058	g_{xy}=0.133	
ω_y=7.26	g_{yy}=0.076	g_{xz}=0.604	D_0=150[a]
ω_z=32.96	g_{zz}=1.57	g_{xy}=0.691	

Stilbene-He

ω_x=9.14	g_{xx}=0.267	g_{xy}=0.611	
ω_y=10.46	g_{yy}=0.349	g_{xz}=2.78	D_0=48[a]
ω_z=47.56	g_{zz}=7.22	g_{xy}=3.17	

a) Experimental upper limit

b) At this energy, a broad, weak absorption appeared to lead to vibrationless stilbene.

Table 2

Observed product state distributions and lifetimes

Energy	Product State	$\tau_{ivr}(ps)^a$	$\tau_{vp}(ps)$	PSD
stilbene-He_2				
198 cm^{-1}	0^0	129	43	72%
	36^1	621	?	15%
	37^1	716	~140	13%
396 cm^{-1}	0^0	236	243	~15%
	25^1	45	<20	77%
	25^137^1	443	?	8%
stilbene-Ne				
198 cm^{-1}	0^0	445	65	56%
	36^1	850	?	30%
	37^1	1821	?	14%
396 cm^{-1}	0^0	379	?	32%
	25^1	209	<20	58%
	25^137^1	1212	?	10%

stilbene-Ar

198 cm^{-1}	?	276	-	-
198+23 cm^{-1}[b]	?	169	-	-
396 cm^{-1}	?	61	-	-
594 cm^{-1}	0^0	<20	125	~80%
	37^1	<20	?	~20%

a) These lifetimes are calculated from measured IVR rates (corrected for k_f) and the product state distributions.

b) The band in the excitation spectrum at -40 cm^{-1} with respect to the 198 cm^{-1} band in bare stilbene.

Table 3

Calculated and observed vibrational predissociation lifetimes

	τ_{vp}(observed)	τ_{vp}(RRKM)	τ_{vp}(momentum-gap)[a]
Stilbene-Ne 198 cm^{-1}	65 ps	75 ps (D_0=150 cm^{-1})[b]	40 ps
		12 (D_0=100 cm^{-1})	
Stilbene-Ne 396 cm^{-1}	<20?[c]	8.4 (D_0=150 cm^{-1})[b]	(independent of initial energy)
Stilbene-Ar 594 cm^{-1}	125	146 (D_0=396 cm^{-1})[d]	1200
		1400 (D_0=500 cm^{-1})	
Stilbene-He_2 198 cm^{-1}	43	42 (D_0=96 cm^{-1})	2
Stilbene-He_2 396 cm^{-1}	<20?[c]	7 (D_0=96 cm^{-1})	

Stilbene-He 83 cm^{-1}	e	12 (D_0=48 cm^{-1})	0.3
Stilbene-He 95 cm^{-1}	e	10	
Stilbene-He 198 cm^{-1}	e	3	
Stilbene-He 396 cm^{-1}	e	2	

a) Taking ΔE=50 cm^{-1}, v_z=2, Δn_v=1.

b) Experimental upper limit for D_0.

c) No lifetime attributable to VP was resolved.

d) Experimental lower limit for D_0.

e) For this complex, IVR and VP lifetimes could not be distinguished.

Figure Captions

Figure 1. Dispersed fluorescence spectra (spectral resolution, R=0.5Å) from exciting the maximum, the red edge, and the blue edge of the broad stilbene-He 37_0^2 and $36_0^1 37_0^1$ absorption bands.

Figure 2. Risetimes in the fluorescence of product in the reactions:

stilbene-He 37^2 →stilbene 37^1 + He τ <20ps

stilbene-He 37^2 →stilbene 0^0 + He τ =43ps

stilbene-He $36^1 37^1$ →stilbene 0^0 + He τ =34ps

R=0.5Å and Δ=56 ps for the 0^0 data. For the 37^1 data, R=3.2Å and Δ=80 ps. χ_r^2equals 1.01, 1.05, and 1.01, respectively, for the three fits.

Figure 3. Dispersed fluorescence spectra (R=0.2Å) of overlapping emission from stilbene-He 25^1 and stilbene 37^4 with molecular beam backing pressures of 600 and 300 psi helium (traces a and b, respectively). The excitation wavelength is marked in trace a. Trace c, emission due to absorption of the complex, was obtained by subtracting trace b from trace a, normalizing the intensity so that the peak at 3088.9Å is completely attributed to absorption of bare stilbene. Trace d shows the intensity of the fluorescence from the complex that would be expected from the measured lifetimes if the complex spectrum is shifted 6 cm^{-1} from the spectrum of the bare molecule.

Figure 4. Temporal data for the decay (τ=160ps, χ^2_r=1.09) of stilbene-He 25^1 fluorescence at 3094.8Å and the rise (τ=173ps, χ^2_r=1.10) in the fluorescence (λ=3096.4Å) of the stilbene formed. R=0.3 and 0.2Å, respectively, and Δ=82ps. The data for the decay of stilbene-He is fit with an additional 2.3 ns decay with an amplitude smaller by a factor of 20. At the excitation wavelength the amplitude of the long component is smaller by a factor of about 100. The residual identified by a "D" is for the data with a fast decaying component and the residual identified by an "R" is for the data with a fast rising component.

Figure 5. Dispersed fluorescence spectra (R=0.5Å) of overlapping emission from stilbene-He $25^136^137^1$ and stilbene 36^137^5 with molecular beam backing pressures of 600 and 200 psi helium (traces a and b, respectively). The excitation wavelength is marked in trace a. Trace c, emission due to absorption of the complex, was obtained by subtracting trace b from trace a, normalizing the intensity so that the bluest major peak is completely attributed to absorption of bare stilbene.

Figure 6. Risetime in the fluorescence of product in the reaction:

stilbene-He $25^136^137^1$ $\rightarrow$stilbene 25^1 + He

R=0.8Å and Δ=90 ps. The best fit is a biexponential with a 18 ps risetime, with χ^2_r=1.08. The best single exponential fit (shown) rises slightly faster than the data.

Figure 7. Dispersed fluorescence spectra (R=0.5Å) of overlapping emission from stilbene-He 25^2 and stilbene $25^1 37^4$ and the normalized difference spectrum.

Figure 8. Temporal data for the decay (τ=60 ps, χ_r^2=1.01) of stilbene-He 25^2 fluorescence at 3064.3Å and the rise (τ=56 ps, χ_r^2=0.97) in the fluorescence (λ=3077.2Å) of the stilbene formed. R=0.8Å and Δ=84 ps. The pressure in the molecular beam was 600 psi. The long component in the data for the fast decay is unchanged at low backing pressure.

Figure 9. Dispersed fluorescence spectrum (R=0.5Å) of stilbene-He_2 25^1. The band at 3124.1Å has not been assigned.

Figure 10. Temporal data for the decay (τ=90 ps, χ_r^2=1.06) of stilbene-He_2 25^1 fluorescence at 3083.6Å and a triple exponential fit (τ_{ivr}=94 ps, Amplitude IVR/Amplitude fluorescence =A_{ivr}/A_f=-1.99, τ_{vp}=42 ps,
A_{vp}/A_f=0.97, χ_r^2=1.00) for the fluorescence of the vibrationless stilbene formed.

Figure 11. Temporal data for the product of the reaction:
stilbene-He_2 25^1 $\rightarrow$stilbene 37^1 + 2He
fit with a 90 ps rise, χ_r^2=1.12. The best fit, with τ=140 ps, has χ_r^2=0.92. R=0.8Å and Δ=84 ps.

Figure 12. Dispersed fluorescence spectrum (R=0.5Å) of stilbene-He_2 25^2. The peak at 3095.5Å has not been assigned.

Figure 13. Temporal data for the decay (τ=36 ps, χ_r^2=1.03) of stilbene-He_2 fluorescence at 3064.9Å and the rise τ=30 ps, χ_r^2=0.99 in the fluorescence (λ=3082.5Å) of the stilbene 25^1 formed. The data to the right is vibrationless stilbene fluorescence and has a strong (A_{vp}/A_f=
-0.481) slowly rising (τ=243 ps) component in the fit (χ_r^2=1.04).

Figure 14. Dispersed fluorescence (R=0.8Å) of stilbene-Ar excited to 25^1X^n (i.e., 198-40 cm^{-1}). The lower trace was recorded under identical conditions, except for the small leak of argon into the molecular beam expansion.

Figure 1. Temporal data for the decay (τ=158 ps, χ_r^2=1.09) of stilbene-Ar 25^1X^n fluorescence at 3089.7Å and the rise (τ=157 ps, χ_r^2=1.01) of emission in the broad part (λ=3127.0Å) of the spectrum.

Figure 16. Dispersed fluorescence spectrum (R=0.5Å) of stilbene-Ar 25^3. An asterisk marks the excitation wavelength.

Figure 17. Temporal data for the product of the reaction:

stilbene-Ar 25^3 $\rightarrow$stilbene 0^0 + Ar

R=8.0Å and Δ=88 ps. The best fit is a biexponential with a 125 ps risetime, χ_r^2=1.01.

Figure 18. Dispersed fluorescence spectrum (R=0.5Å) of stilbene-Ne 25^1. An asterisk marks the excitation wavelength.

Figure 19. Temporal data for the decay (τ=233 ps, χ_r^2=1.04) of stilbene-Ne 25^1 fluorescence at 3096.0Å and a triple exponential fit (τ_{ivr}=233 ps, A_{ivr}/A_f=-1.34, τ_{vp}=65 ps, A_{vp}/A_f=0.36, χ_r^2=0.93) for the fluorescence of the vibrationless stilbene formed.

Figure 20. Dependence on spectral resolution of the temporal data for the weak stilbene 37^1 band at 3097.7Å in Figure 18. For the decay with the faster (τ=195 ps) rise, R=1.0Å, Δ=88 ps, A_{ivr}/A_f=-0.50, and χ_r^2=1.08. For the decay with the slower (τ=207 ps) rise, R=0.5Å, Δ=112 ps, A_{ivr}/A_f=-0.92, and χ_r^2=1.10.

Figure 21. Dispersed fluorescence spectrum (R=0.5Å) of stilbene-Ne 25^2. An asterisk marks the excitation wavelength.

Figure 22. Temporal data for the decay (τ=111 ps, χ_r^2=1.07) of stilbene-Ne 25^2 fluorescence at 3077.9Å and for the rise (τ=119 ps, χ_r^2=1.03) of fluorescence from stilbene 25^1. The decay of resonance fluorescence at the excitation wavelength has nearly no long-time component, but could not be fit due to a contribution from scattered laser light.

Figure 23. Sections of the van der Waals potential energy surface between stilbene and argon along the van der Waals normal coordinates and

the fits sections to a Morse potential and two $1/\cosh^2 x$ potentials.

Figure 24. Vibrational energy level diagram for stilbene and stilbene-He. To the right of each "stilbene-like" vibrational level in the complex is a plot of the total density of vibrational levels in the complex, including van der Waals levels. The sharp peaks in the state density occur as the energy in the van der Waals modes approach D_0.

Figure 25. The total density of vibrational states in stilbene-Ne and stilbene-Ar including the full anharmonicity of the van der Waals modes.

Figure 1

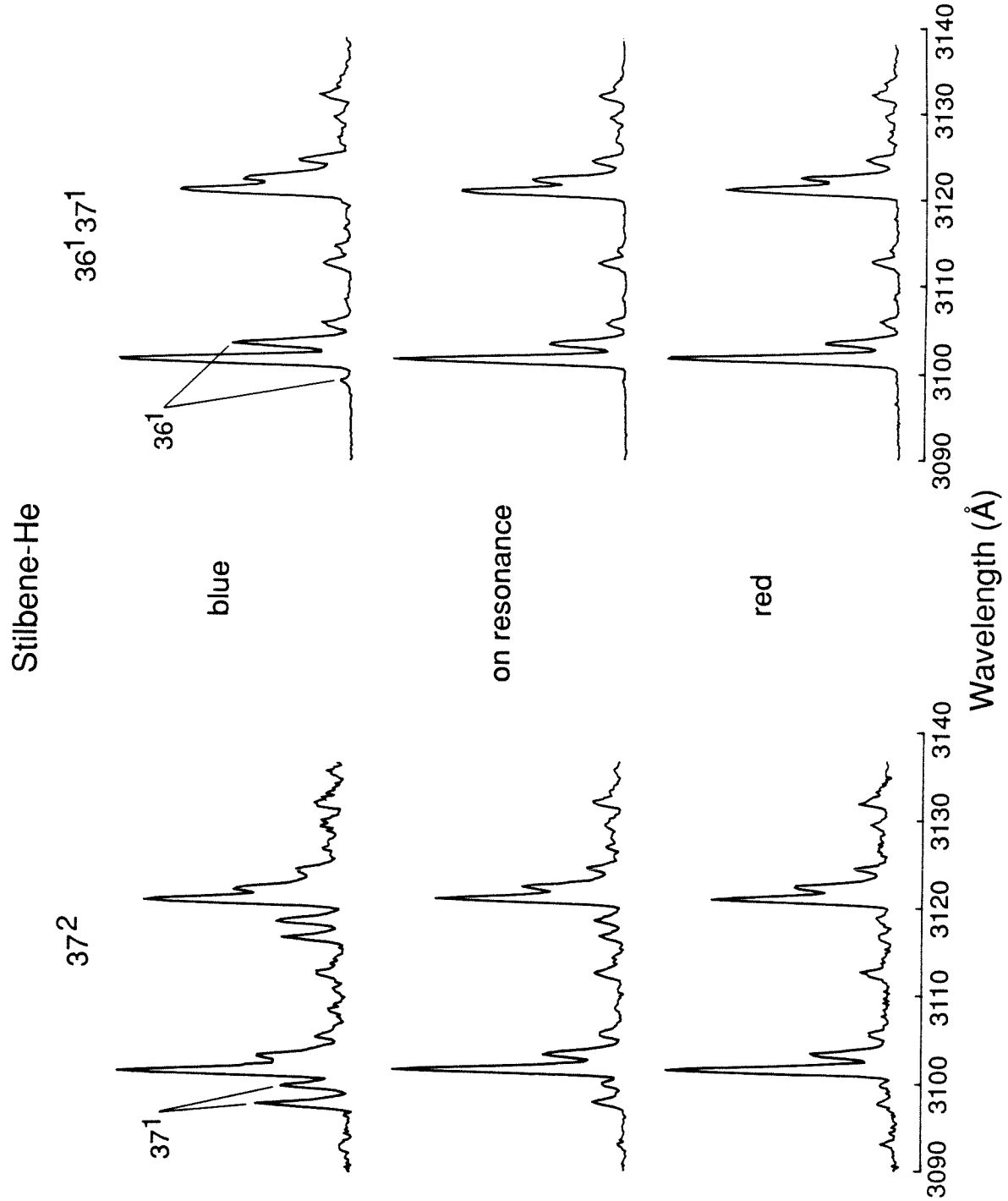
Stilbene-He
37^2
37^1
blue
36^1
$36^1 37^1$
on resonance
red
3090 3100 3110 3120 3130 3140
Wavelength (Å)

Figure 2

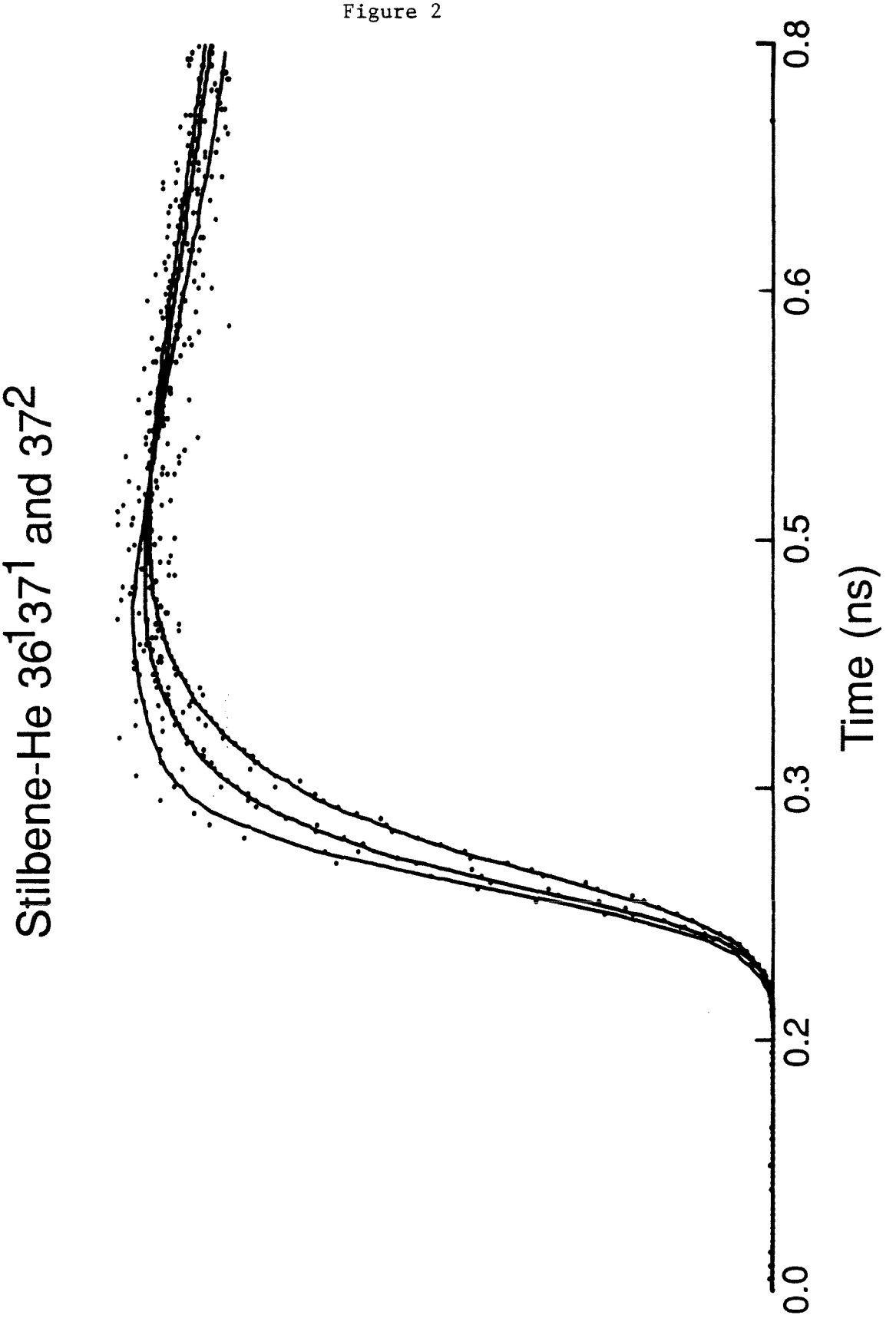

Figure 3

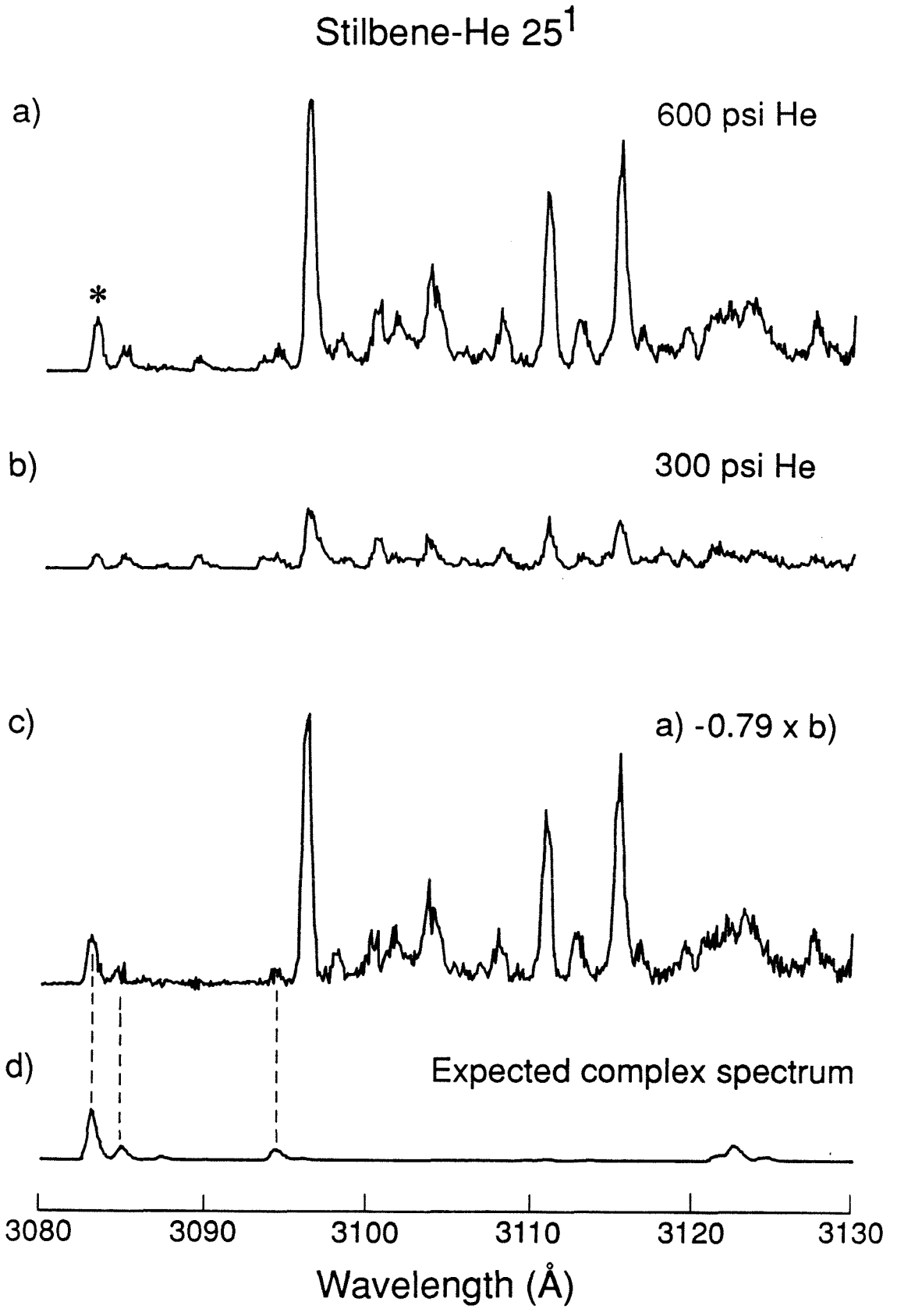
Stilbene-He 25[1]
a)
600 psi He
*
b)
300 psi He
c)
a) -0.79 x b)
d)
Expected complex spectrum
3080
3090
3100
3110
3120
3130
Wavelength (Å)

Figure 4

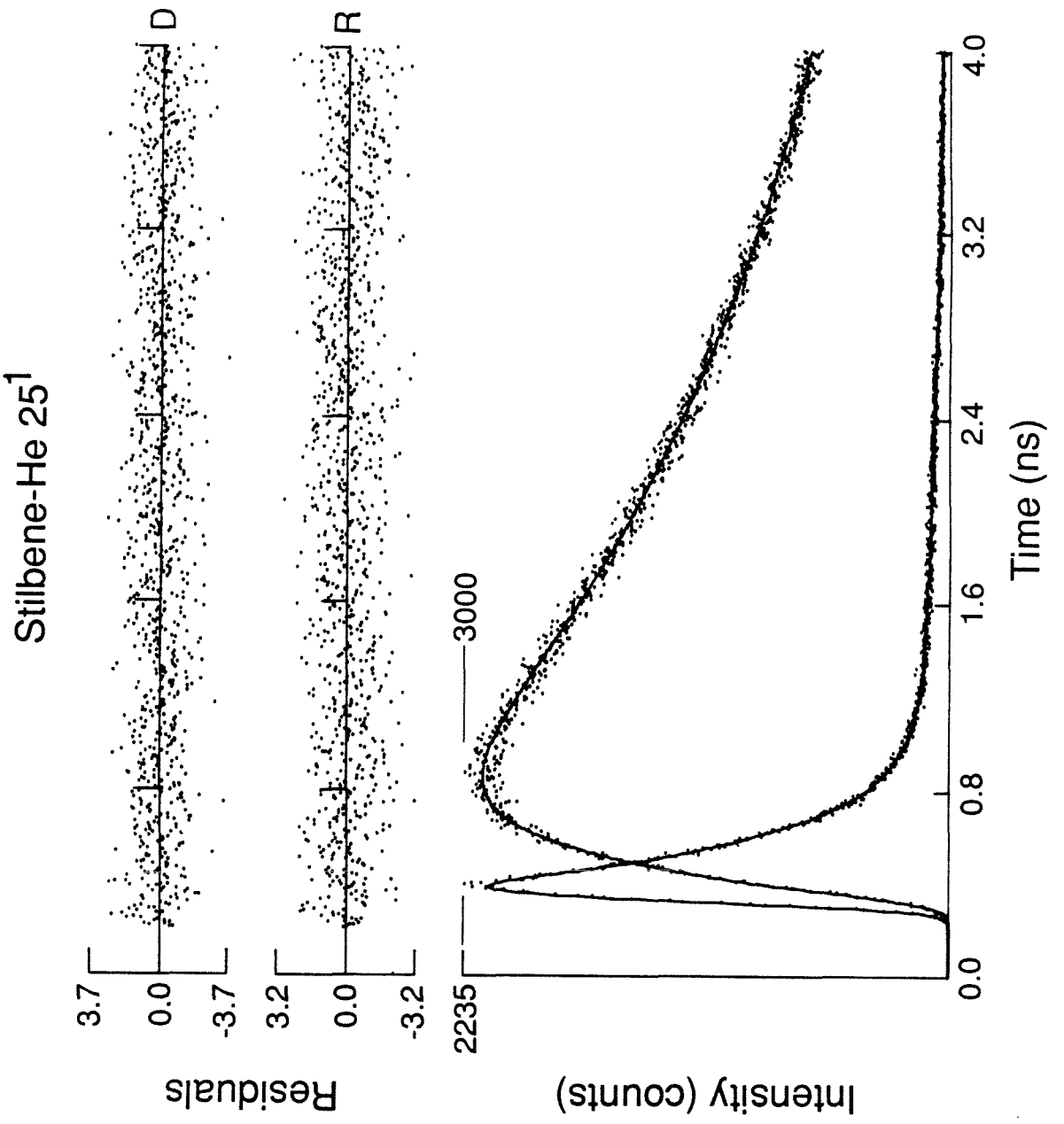
Stilbene-He 25[1]
D
R
3.7
0.0
-3.7
3.2
0.0
-3.2
Residuals
3000
2235
0.0
0.8
1.6
2.4
3.2
4.0
Intensity (counts)
Time (ns)

Figure 5

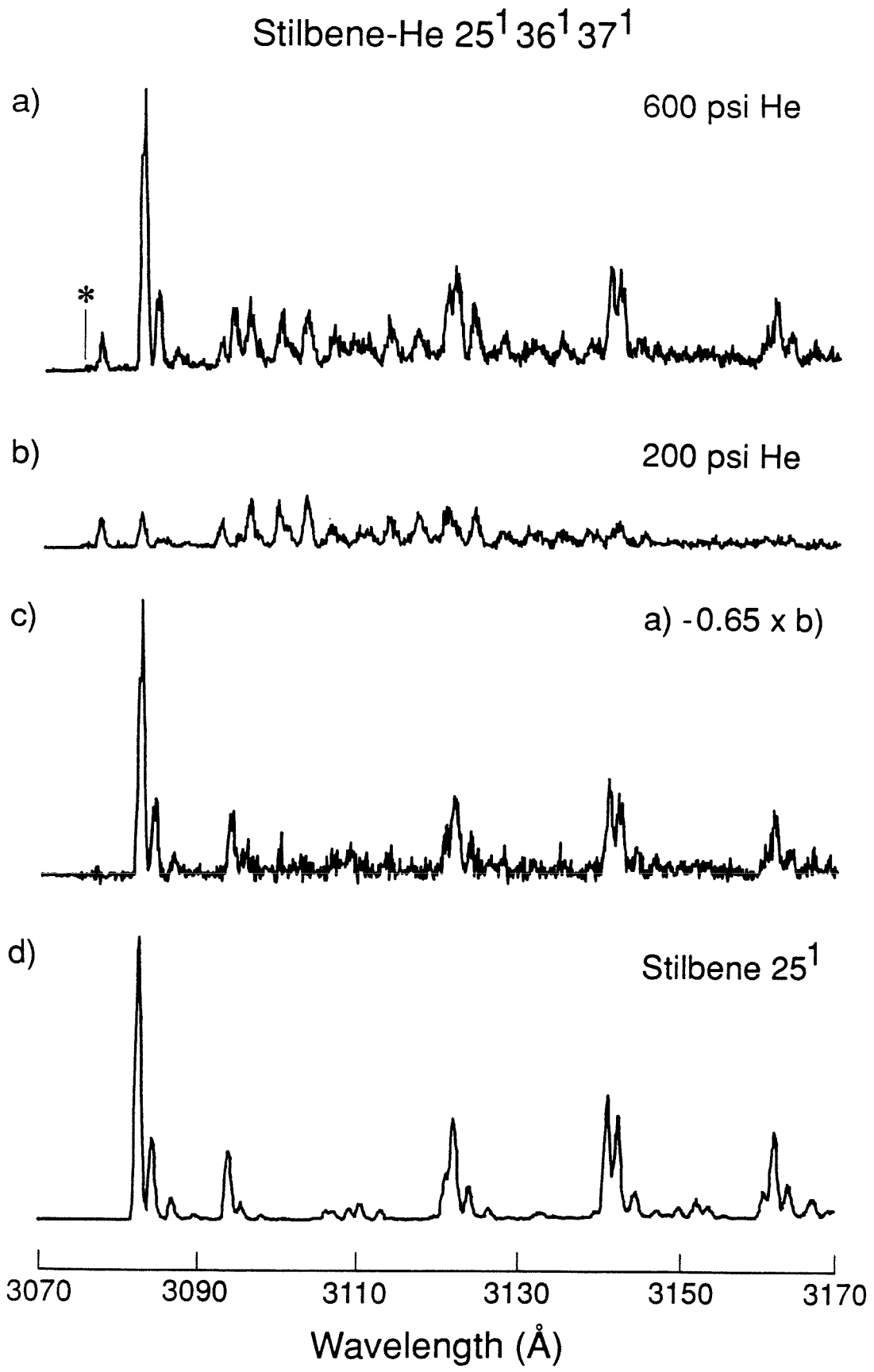
Stilbene-He $25^1 36^1 37^1$
a)
600 psi He
*
b)
200 psi He
c)
a) -0.65 x b)
d)
Stilbene 25^1
3070
3090
3110
3130
3150
3170
Wavelength (Å)

Figure 6

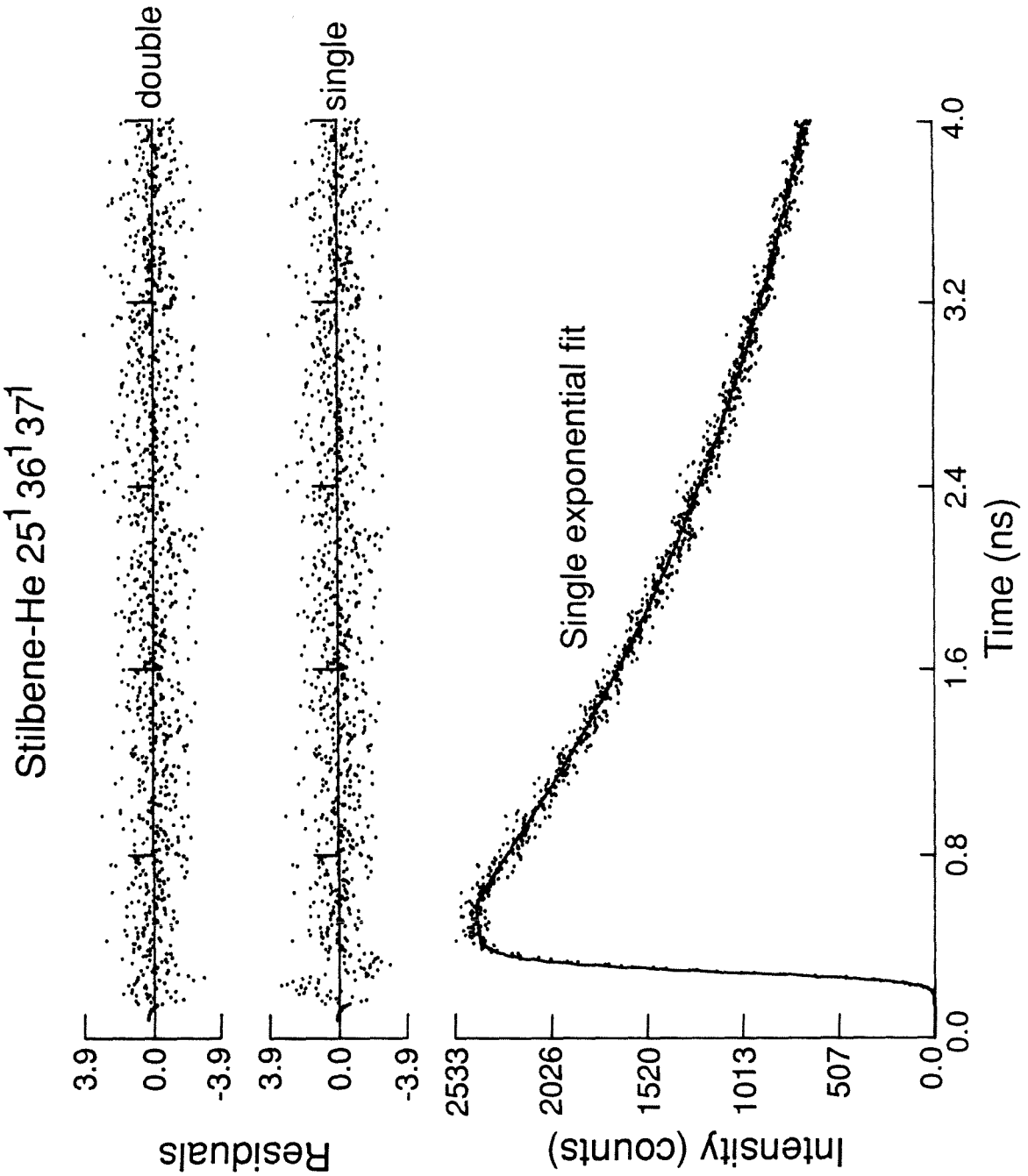
Stilbene-He 25¹ 36¹ 37¹
double
single
Residuals
3.9
0.0
-3.9
Single exponential fit
Intensity (counts)
2533
2026
1520
1013
507
0.0
0.8
1.6
2.4
3.2
4.0
Time (ns)

Figure 7

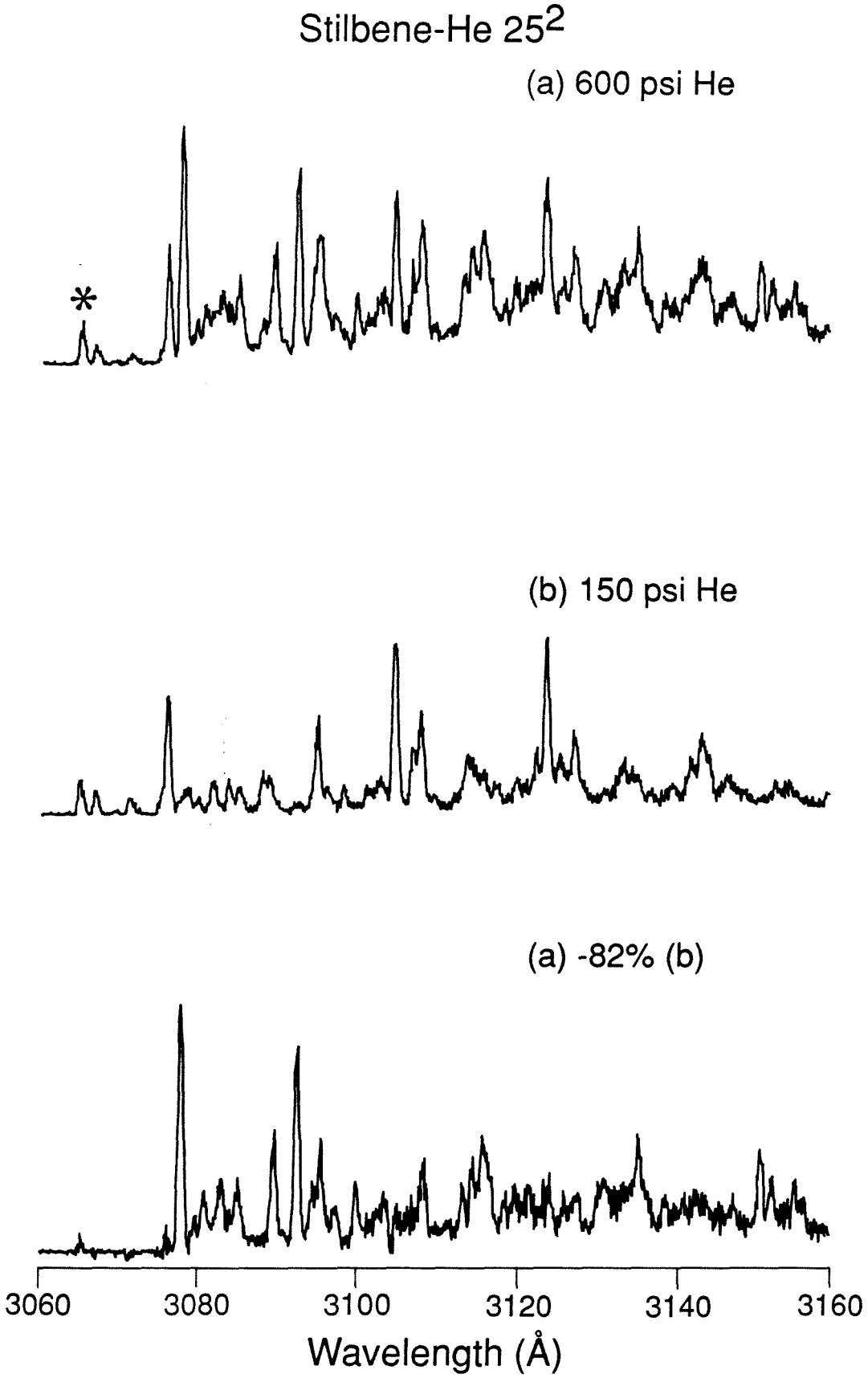
Stilbene-He 25²
(a) 600 psi He
*
(b) 150 psi He
(a) -82% (b)
3060
3080
3100
3120
3140
3160
Wavelength (Å)

Figure 8

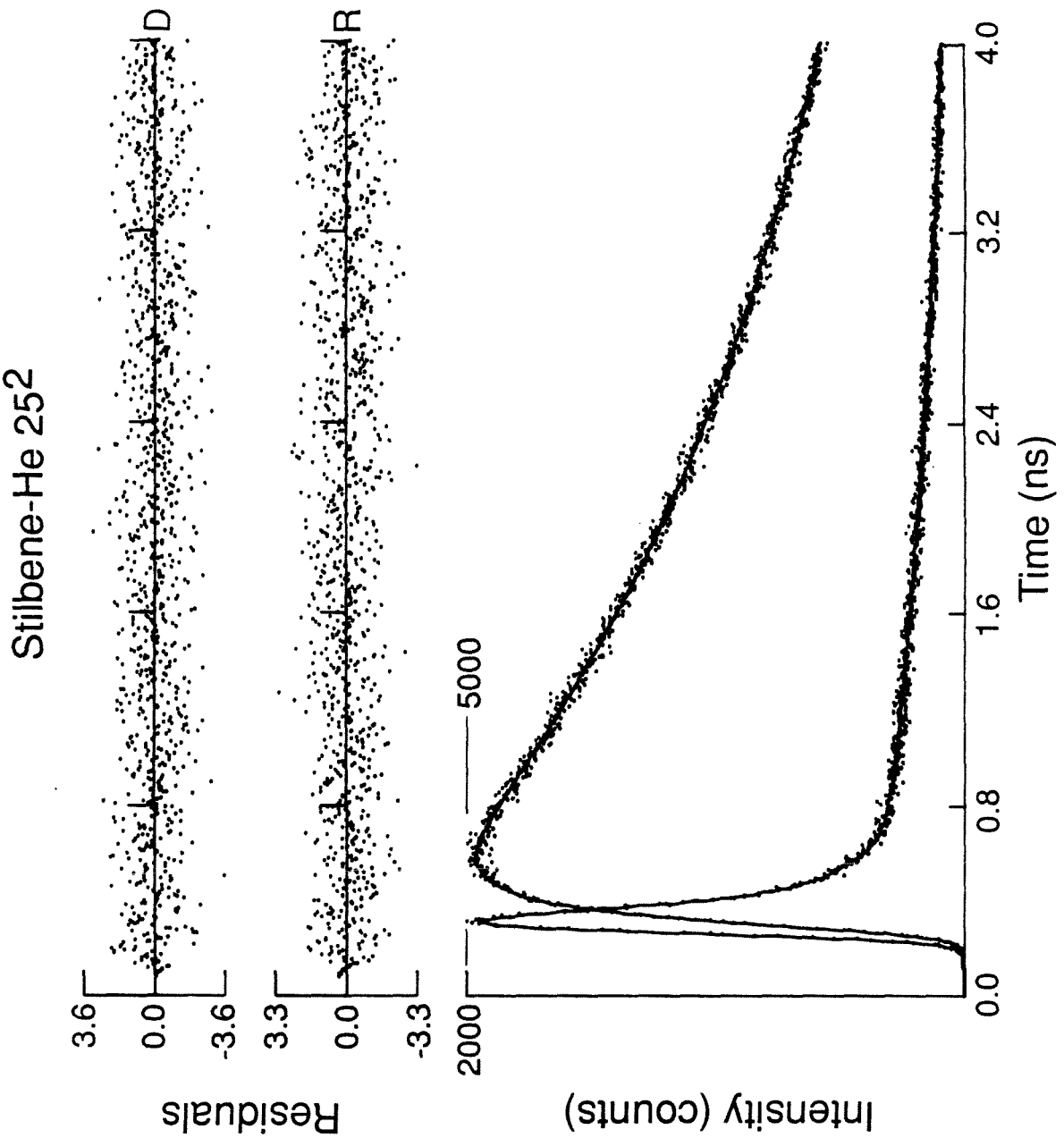
Stilbene-He 252
D
R
3.6
0.0
-3.6
3.3
0.0
-3.3
Residuals
2000
5000
Intensity (counts)
0.0
0.8
1.6
2.4
3.2
4.0
Time (ns)

Figure 9

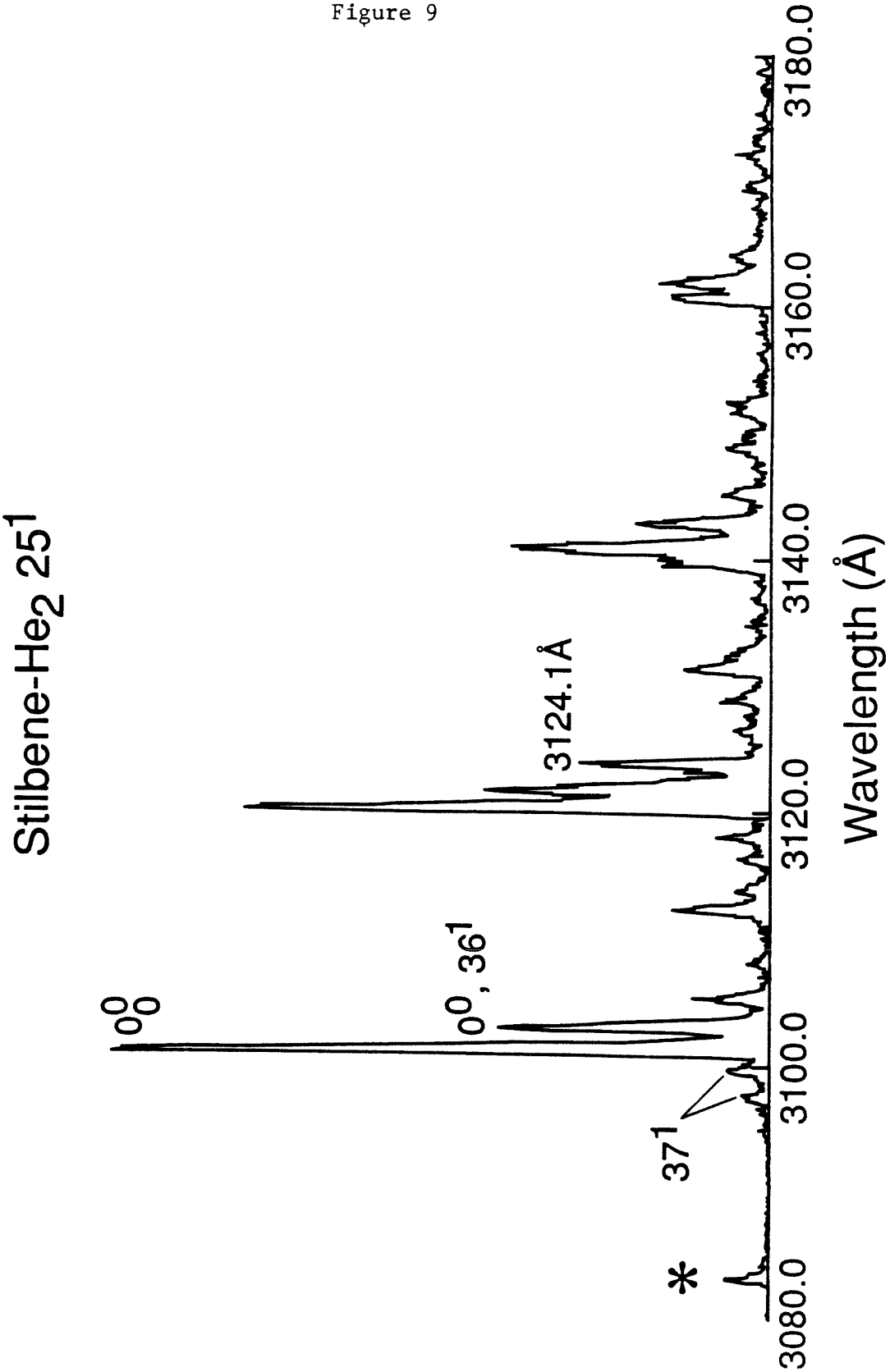
Stilbene-He2 25¹
0₀⁰
0₀⁰, 36¹
3124.1Å
37¹
*
3080.0
3100.0
3120.0
3140.0
3160.0
3180.0
Wavelength (Å)

Figure 10

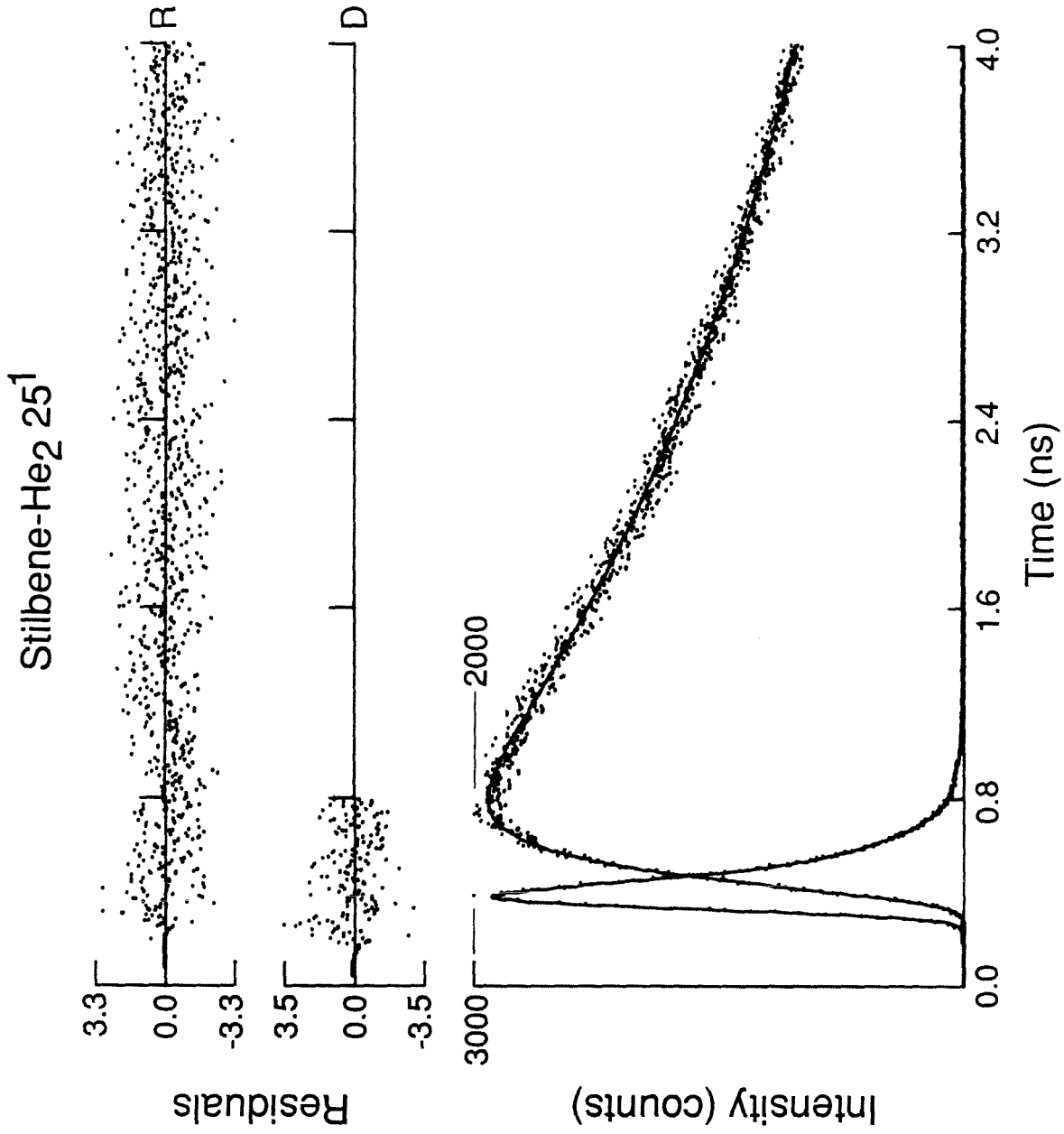
Stilbene-He2 25[1]
R
D
3.3
0.0
-3.3
3.5
0.0
-3.5
Residuals
3000
2000
Intensity (counts)
0.0
0.8
1.6
2.4
3.2
4.0
Time (ns)

Figure 11

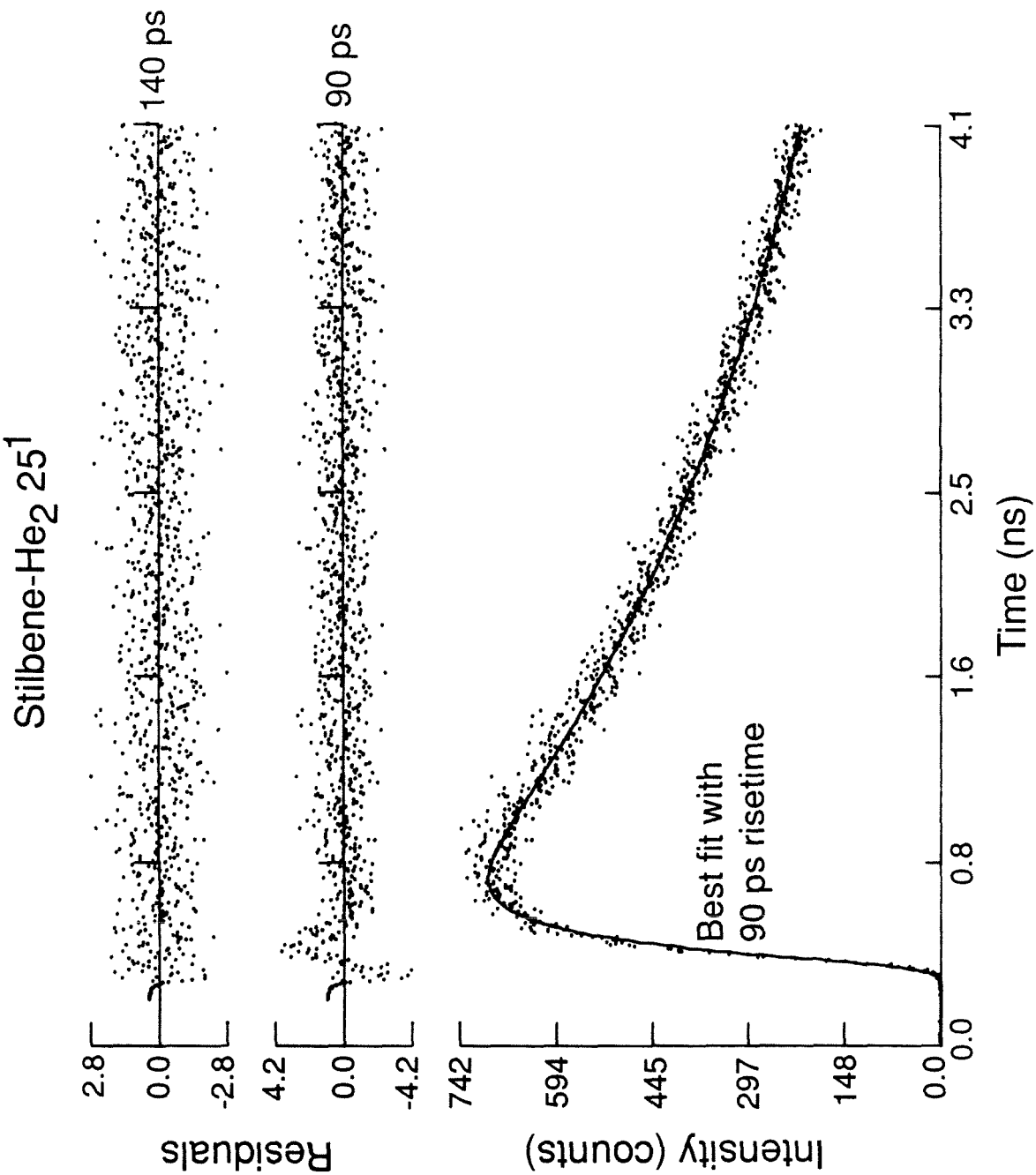
Stilbene-He2 25[1]
140 ps
90 ps
Residuals
2.8
0.0
-2.8
4.2
0.0
-4.2
Intensity (counts)
742
594
445
297
148
0.0
Best fit with
90 ps risetime
0.0
0.8
1.6
2.5
3.3
4.1
Time (ns)

Figure 12

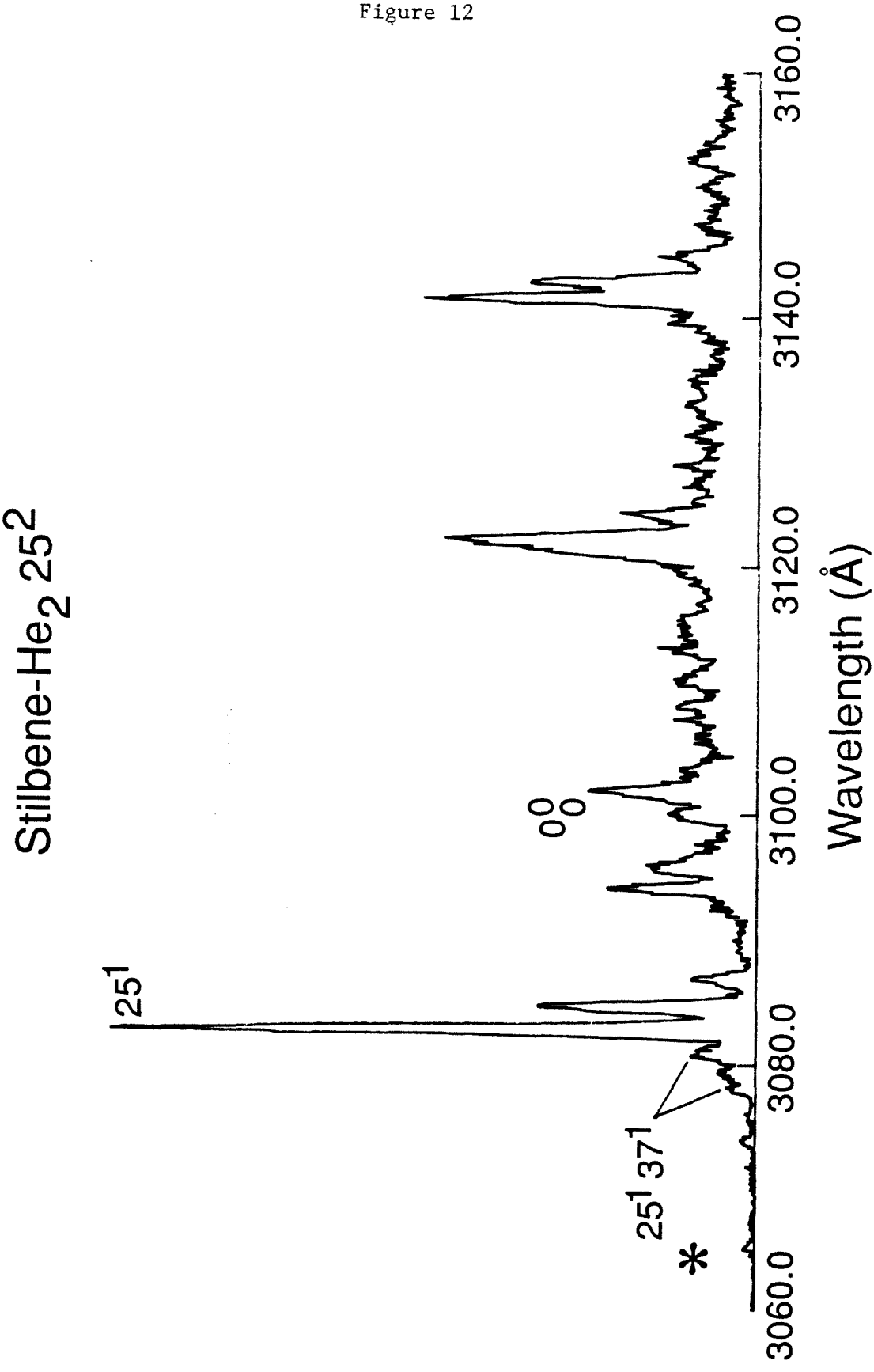
Stilbene-He2 25^2
25^1
0^0_0
25^1 37^1
*
3060.0
3080.0
3100.0
3120.0
3140.0
3160.0
Wavelength (Å)

Figure 13

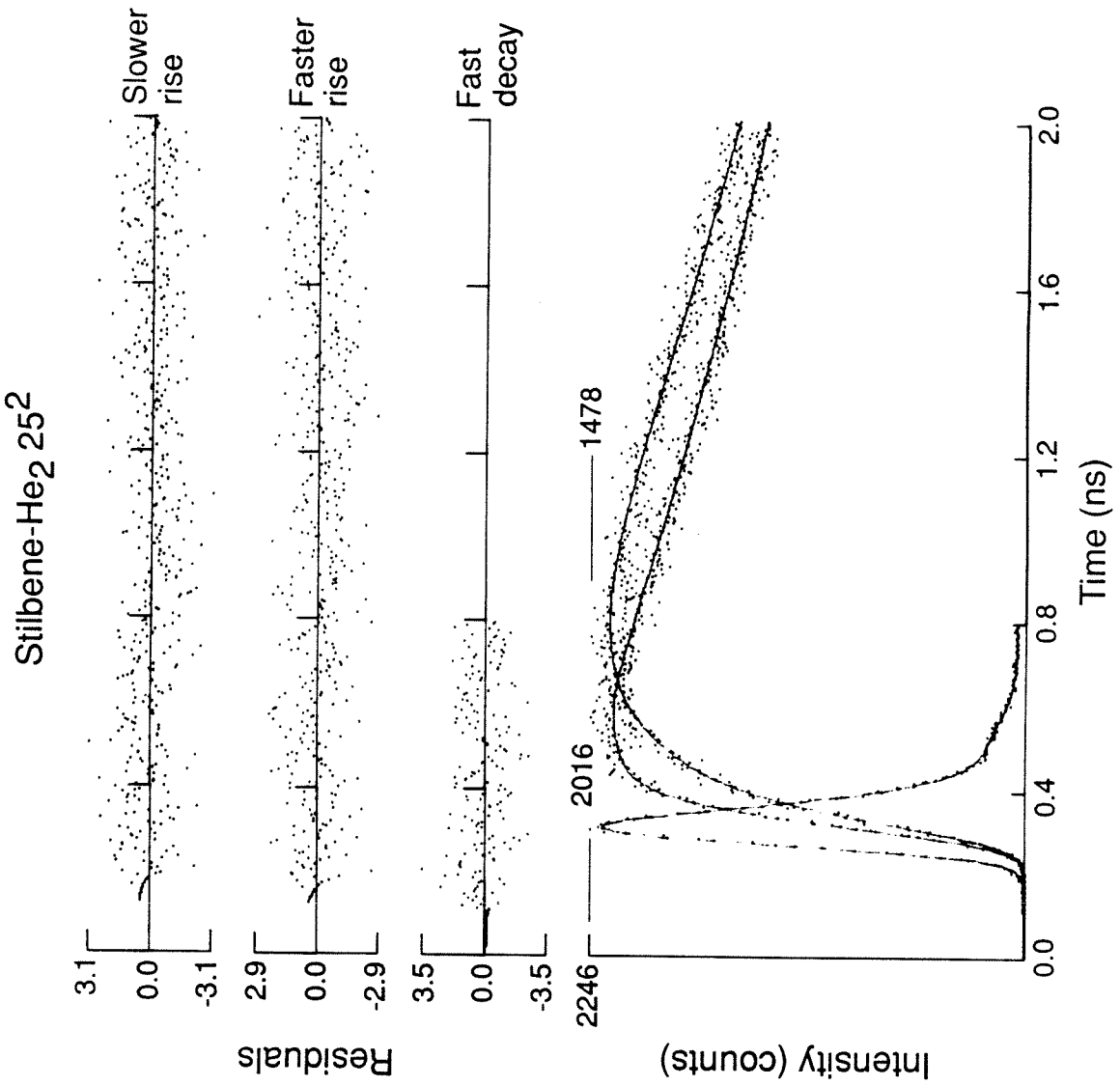
Stilbene-He2 25^2
Slower rise
Faster rise
Fast decay
3.1
0.0
-3.1
2.9
0.0
-2.9
3.5
0.0
-3.5
Residuals
2246
2016
1478
Intensity (counts)
0.0
0.4
0.8
1.2
1.6
2.0
Time (ns)

Figure 14

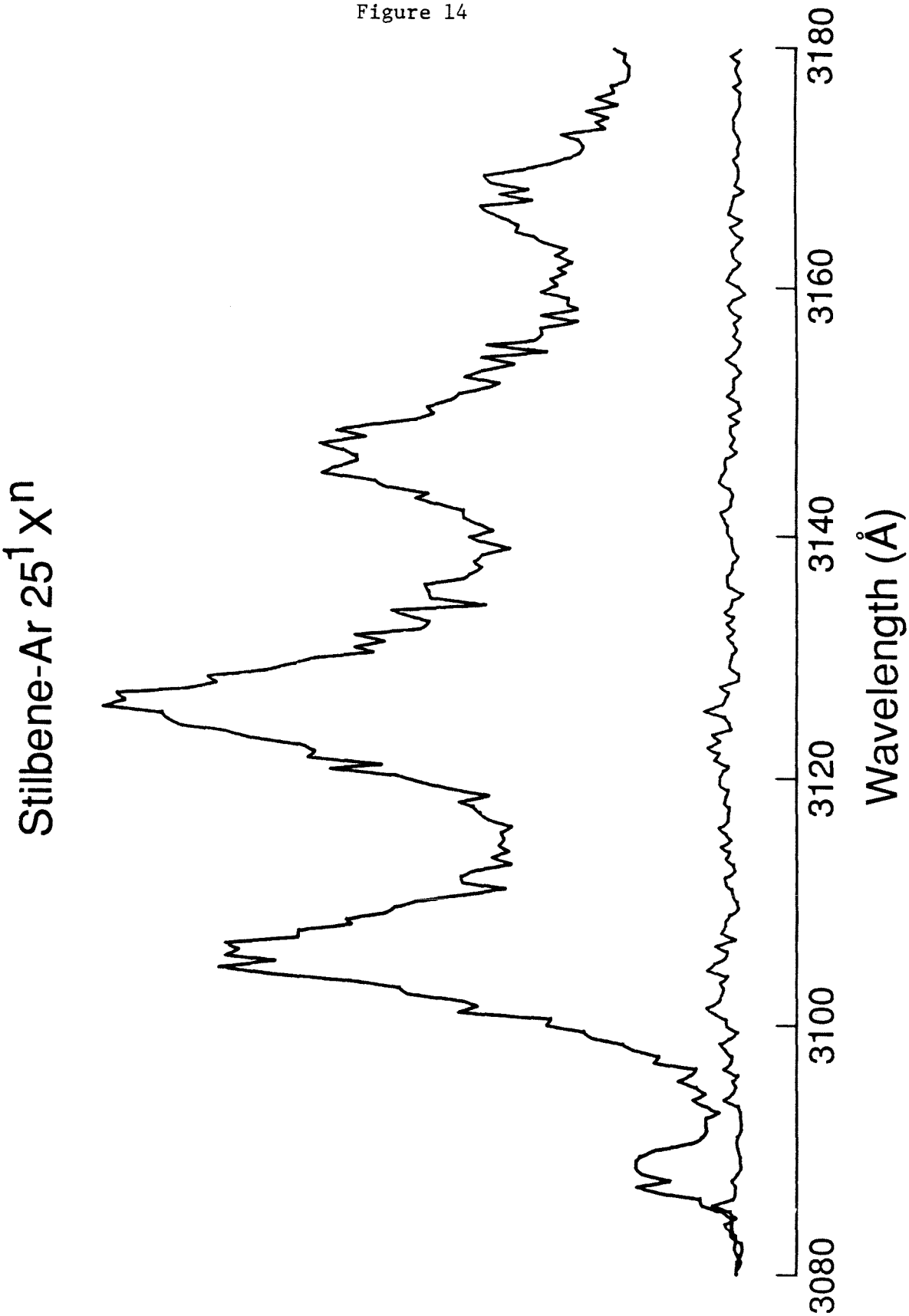
Stilbene-Ar 25 $^{1}X^{n}$
3080
3100
3120
3140
3160
3180
Wavelength (Å)

Figure 15

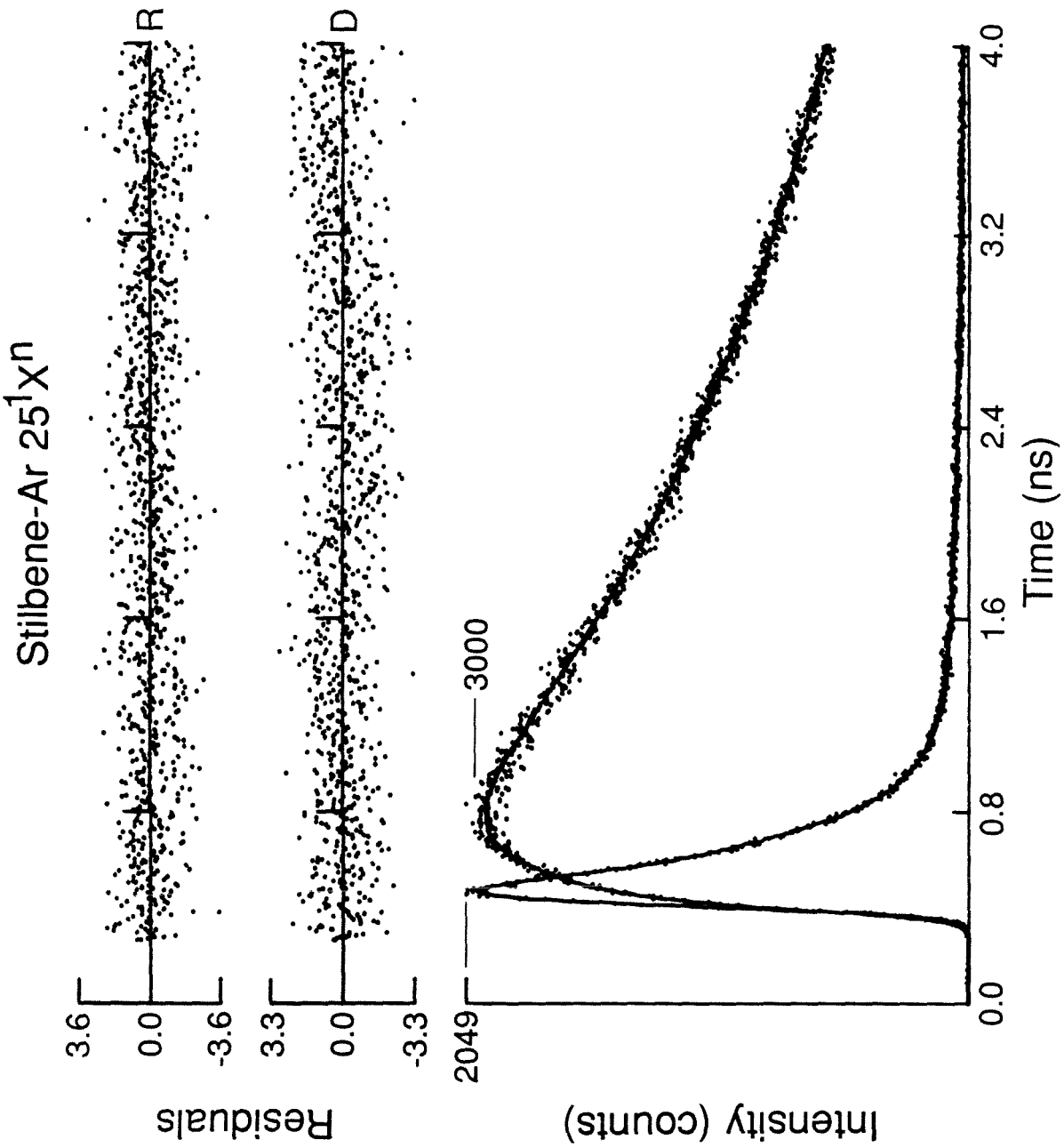
Stilbene-Ar 25 1Xn
R
D
3.6
0.0
-3.6
3.3
0.0
-3.3
Residuals
2049
3000
0.0
0.8
1.6
2.4
3.2
4.0
Time (ns)
Intensity (counts)

Figure 16

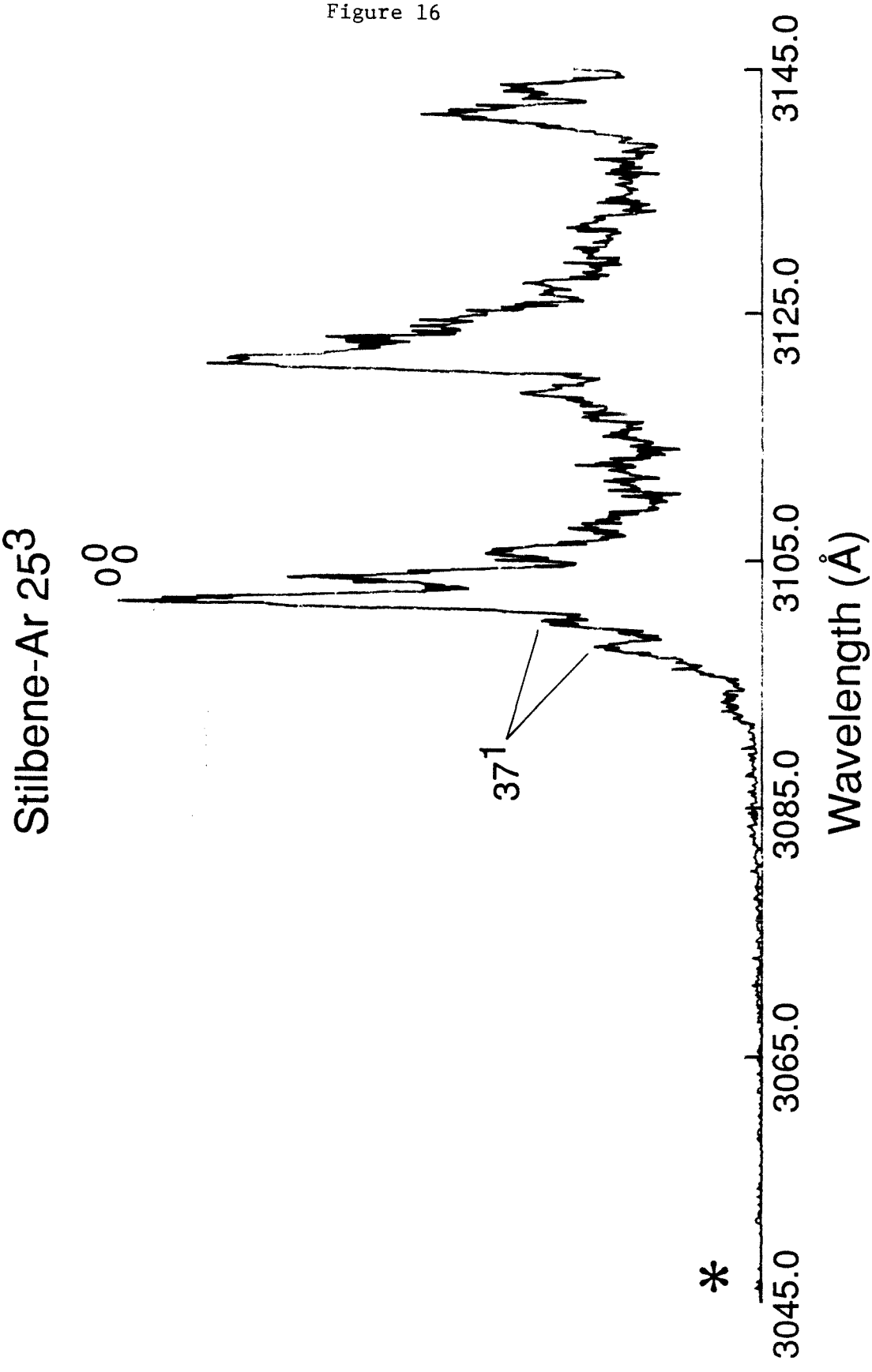
Stilbene-Ar 25^3
0^0_0
37^1
*
3045.0
3065.0
3085.0
3105.0
3125.0
3145.0
Wavelength (Å)

Figure 17

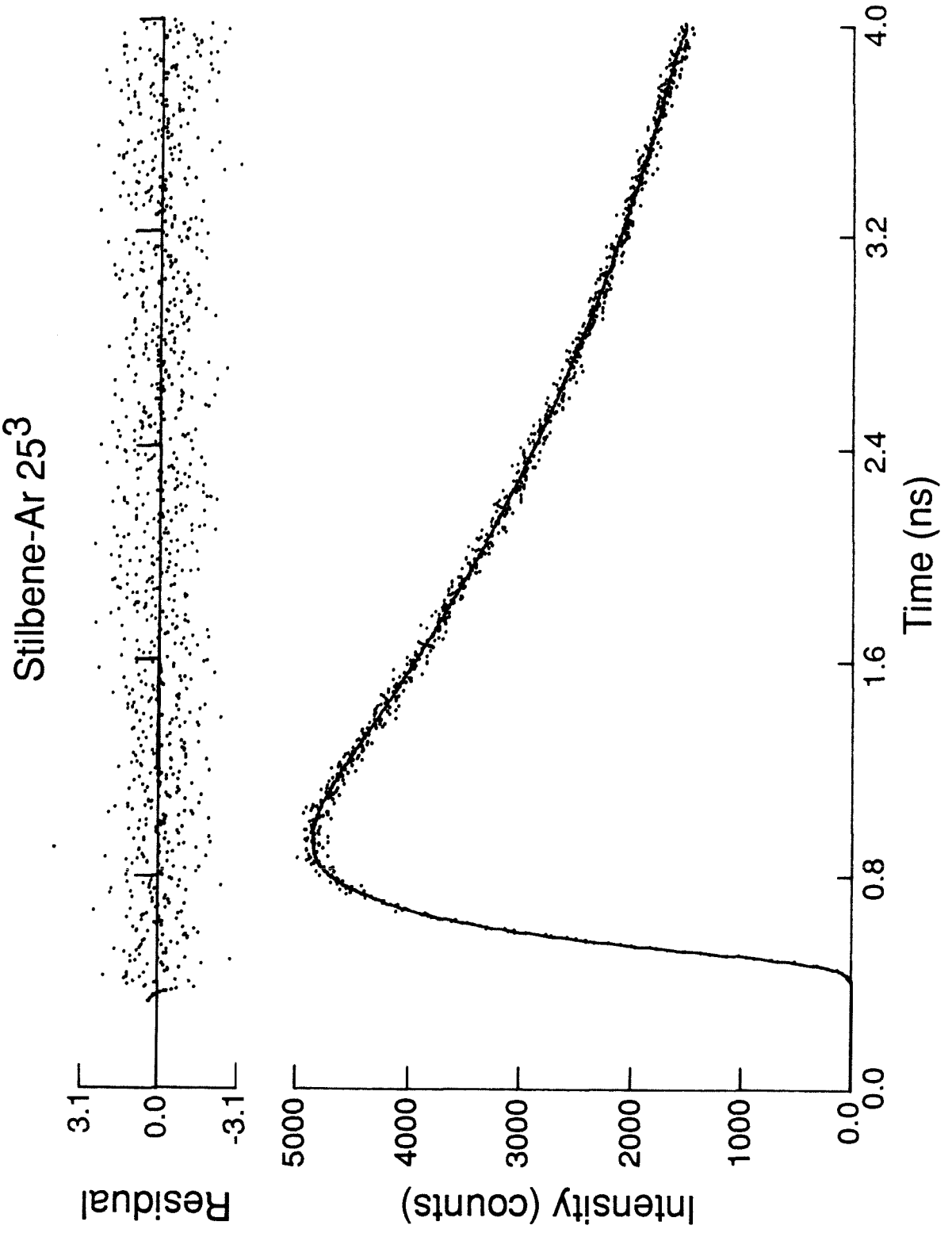
Stilbene-Ar 25^3
Residual
3.1
0.0
-3.1
Intensity (counts)
5000
4000
3000
2000
1000
0.0
0.0
0.8
1.6
2.4
3.2
4.0
Time (ns)

Figure 18

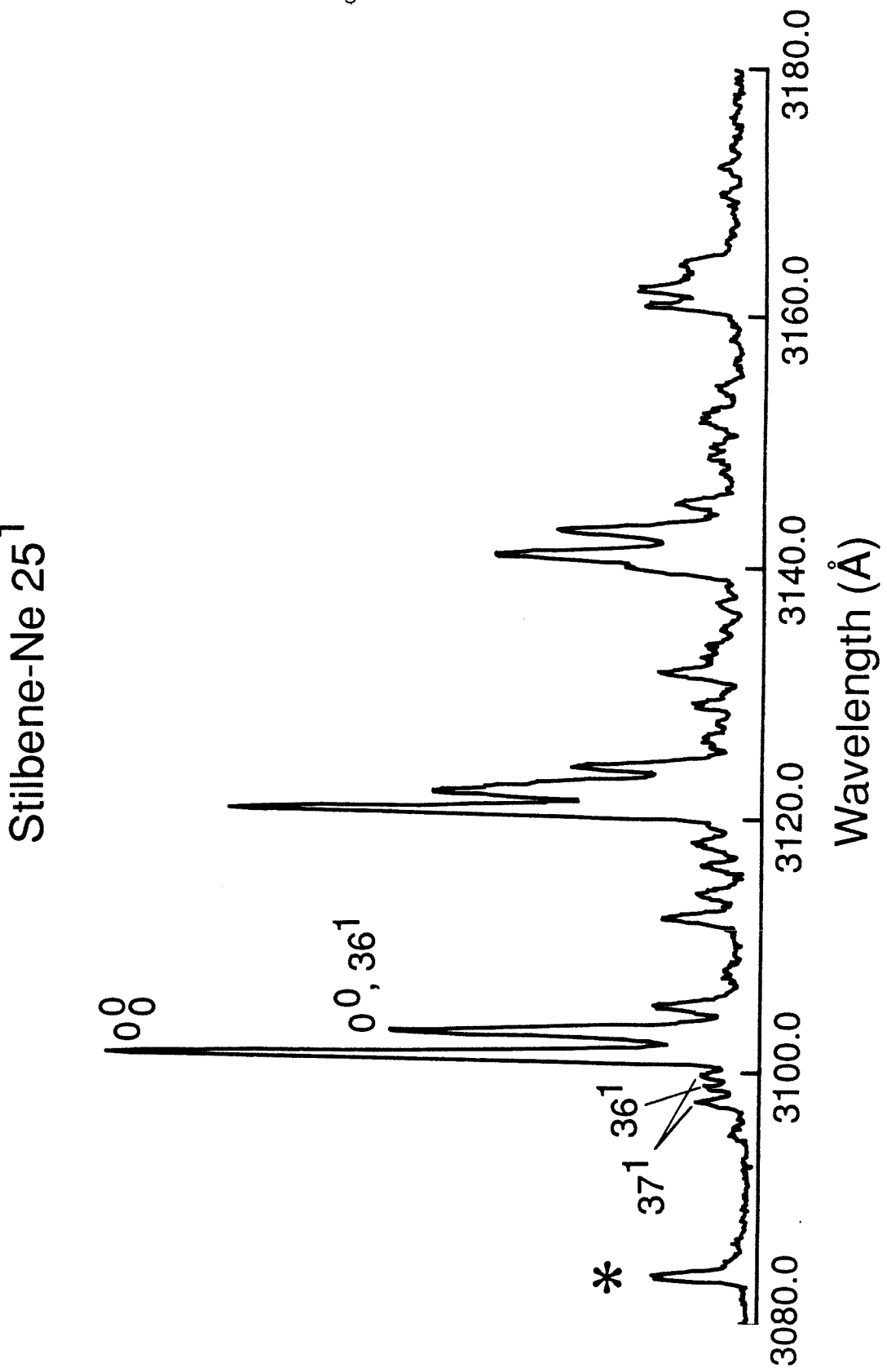
Stilbene-Ne 25^1
0_0^0
$0_0^0, 36^1$
36^1
37^1
*
3080.0
3100.0
3120.0
3140.0
3160.0
3180.0
Wavelength (Å)

Figure 19

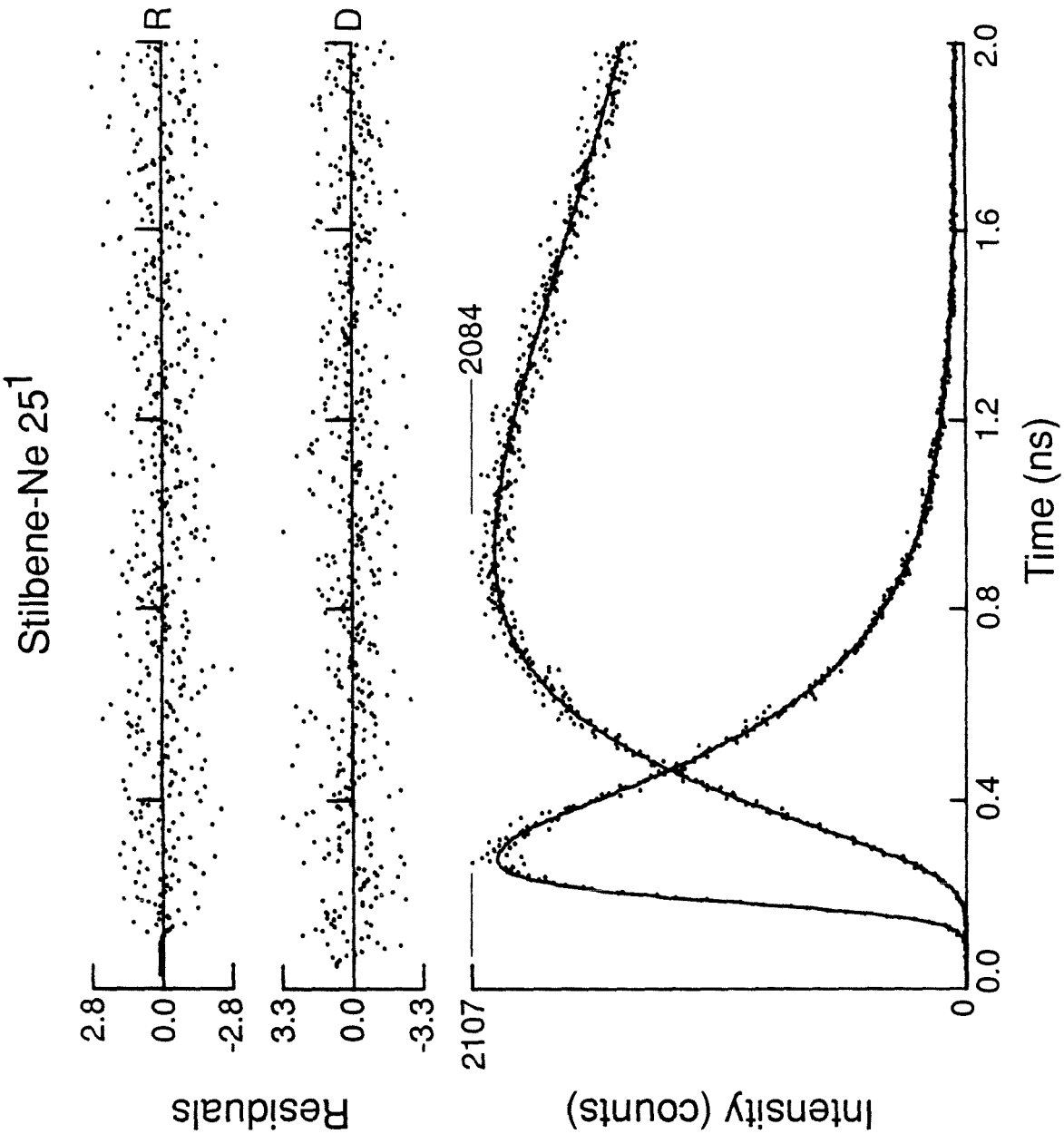
Stilbene-Ne 25[1]
R
D
2.8
0.0
-2.8
3.3
0.0
-3.3
Residuals
2107
2084
0
0.0
0.4
0.8
1.2
1.6
2.0
Intensity (counts)
Time (ns)

Figure 20

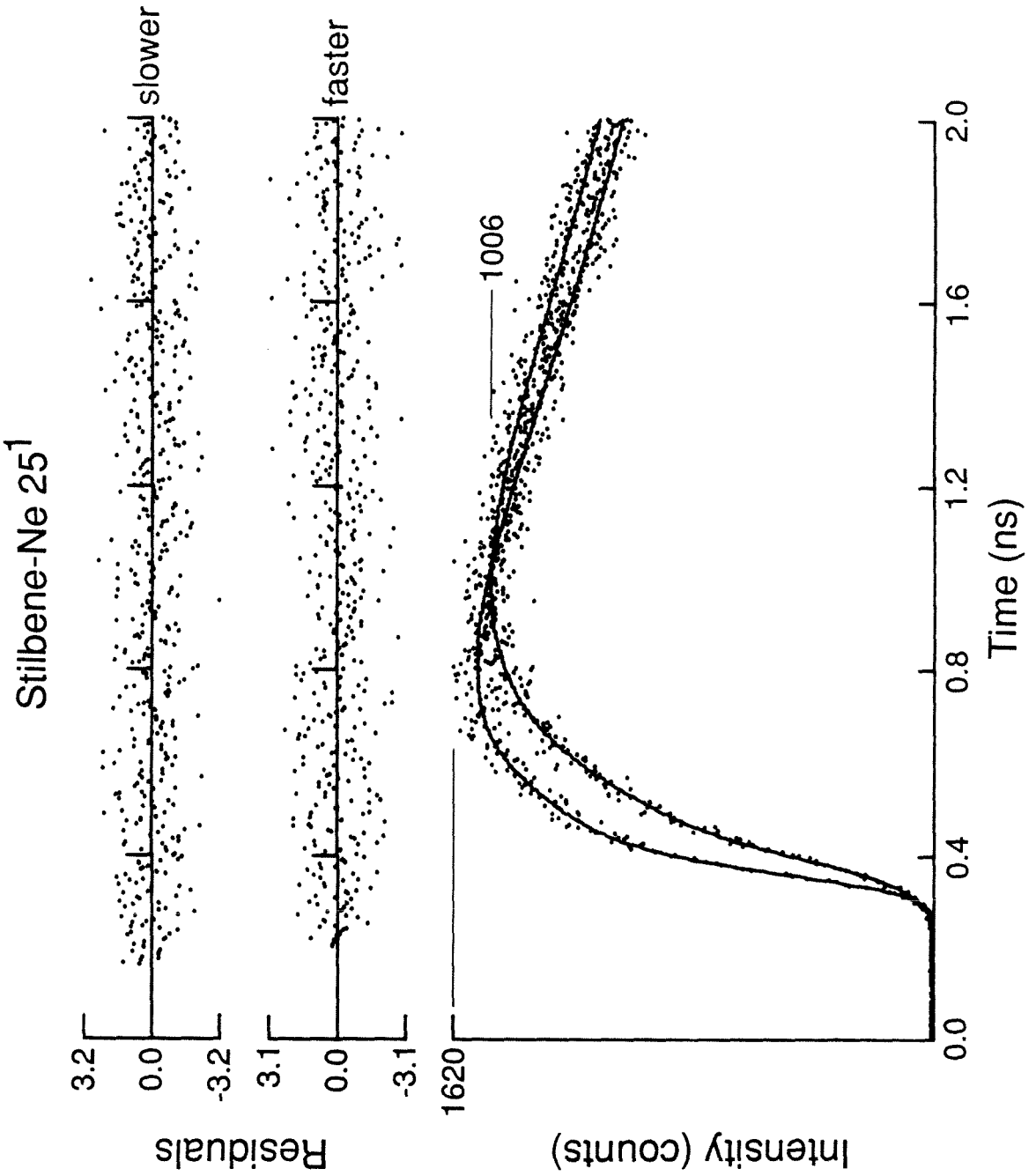
Stilbene-Ne 25[1]
slower
faster
3.2
0.0
-3.2
3.1
0.0
-3.1
Residuals
1620
1006
Intensity (counts)
0.0
0.4
0.8
1.2
1.6
2.0
Time (ns)

Figure 21

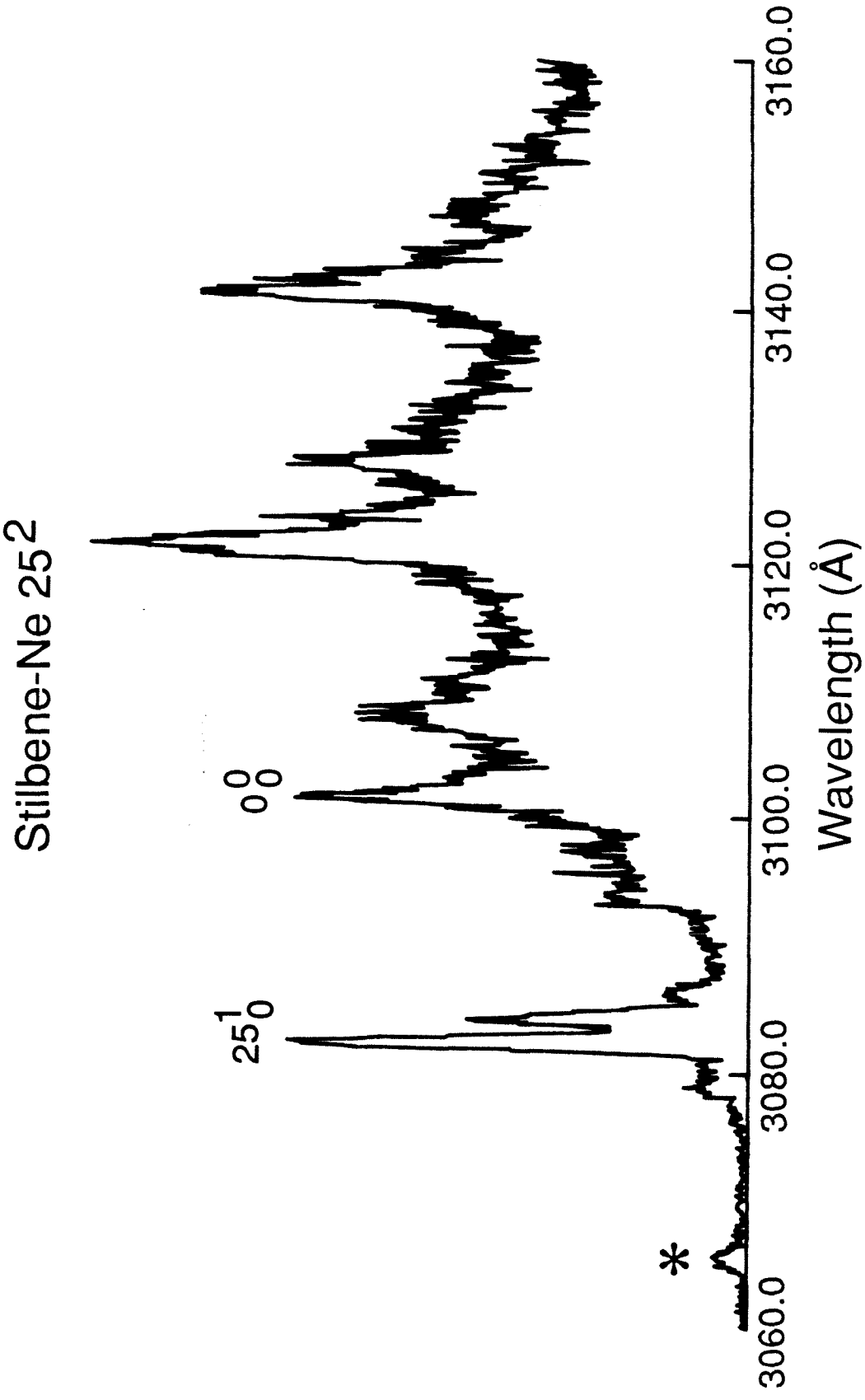
Stilbene-Ne 25^2
0^0_0
25^1_0
*
3060.0
3080.0
3100.0
3120.0
3140.0
3160.0
Wavelength (Å)

Figure 22

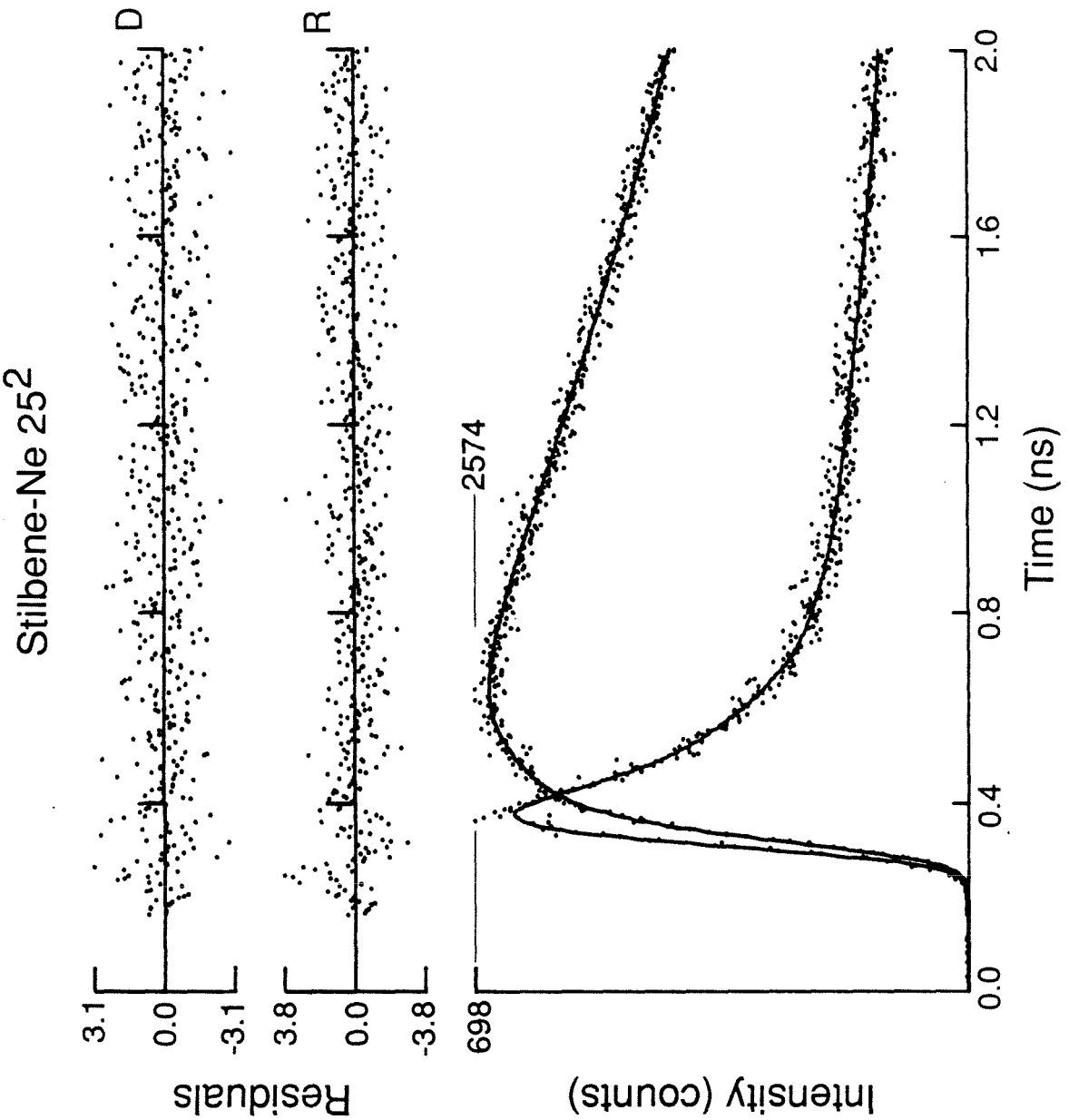
Stilbene-Ne 25²
D
R
3.1
0.0
-3.1
3.8
0.0
-3.8
Residuals
2574
698
0.0
0.4
0.8
1.2
1.6
2.0
Time (ns)
Intensity (counts)

Figure 23

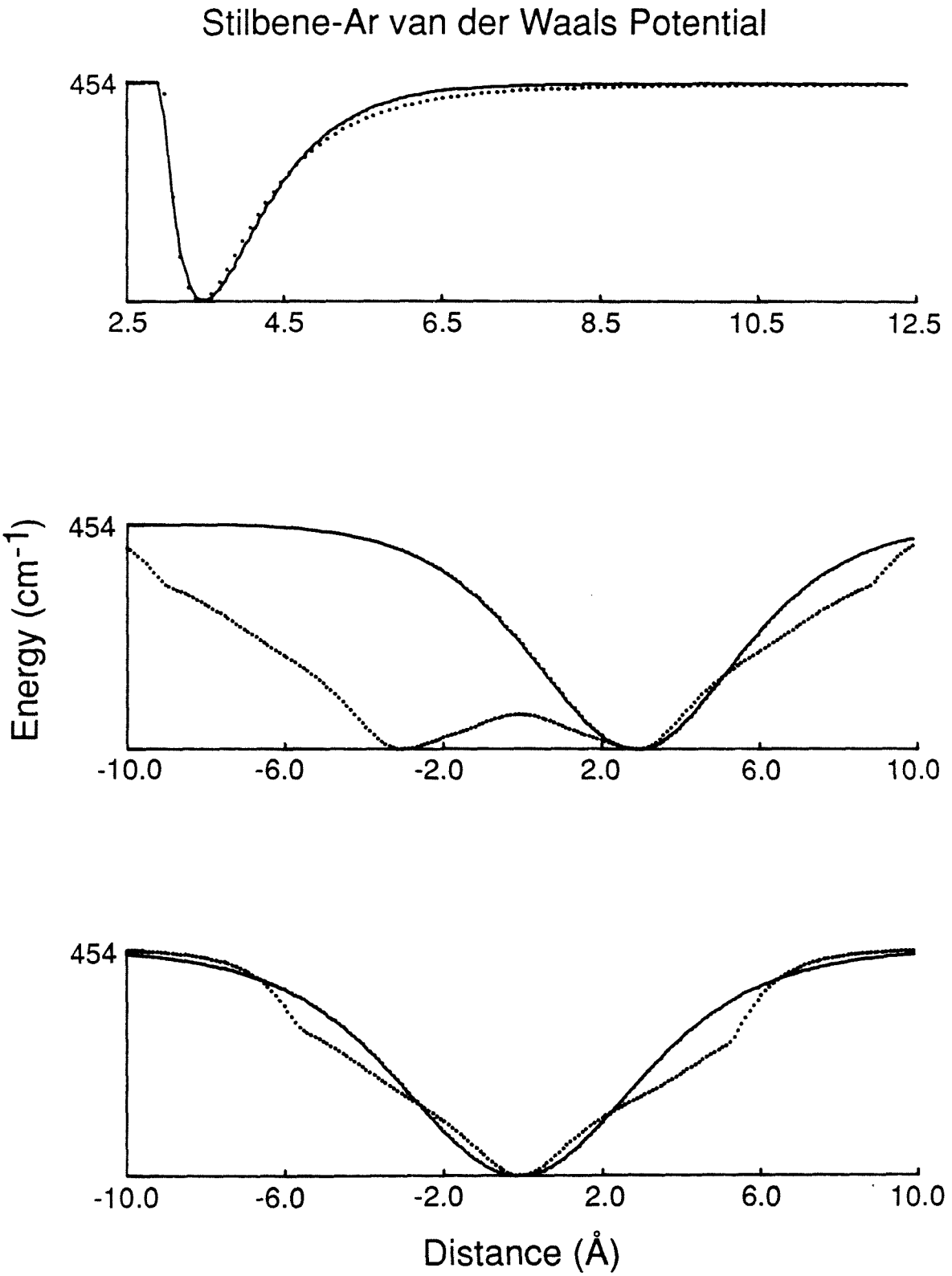
Stilbene-Ar van der Waals Potential
454
2.5
4.5
6.5
8.5
10.5
12.5
Energy (cm-1)
454
-10.0
-6.0
-2.0
2.0
6.0
10.0
454
-10.0
-6.0
-2.0
2.0
6.0
10.0
Distance (Å)

Figure 24

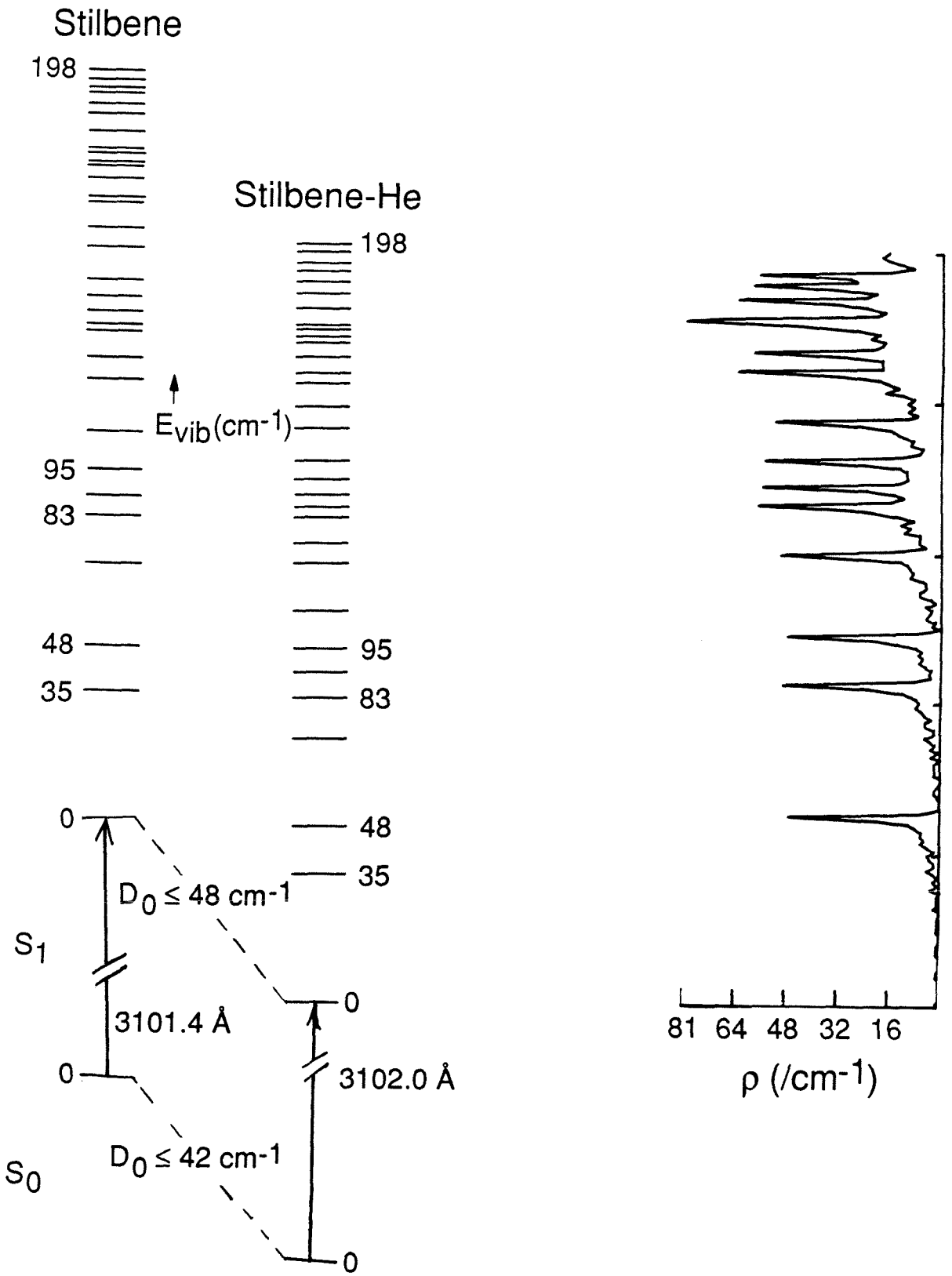
Stilbene
198
95
83
48
35
Stilbene-He
198
$E_{vib}(cm^{-1})$
95
83
48
35
0
$D_0 \leq 48\ cm^{-1}$
S_1
3101.4 Å
0
0
3102.0 Å
$D_0 \leq 42\ cm^{-1}$
S_0
0
81 64 48 32 16
$\rho\ (/cm^{-1})$

Figure 25

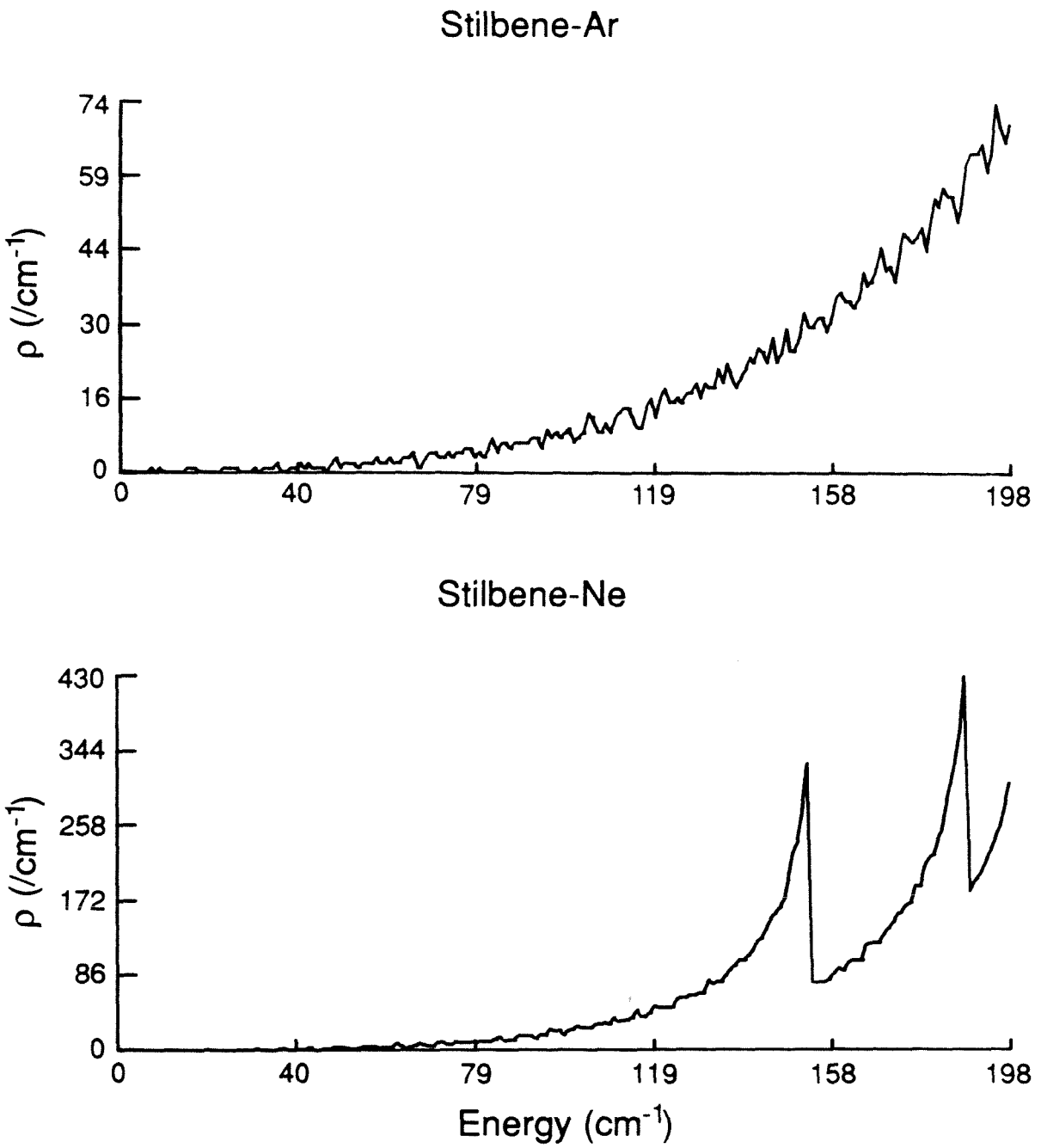
Stilbene-Ar
74
59
44
30
16
0
ρ (/cm-1)
0
40
79
119
158
198
Stilbene-Ne
430
344
258
172
86
0
ρ (/cm-1)
0
40
79
119
158
198
Energy (cm-1)

Chapter Five

Vibrational Predissociation in van der Waals Complexes of Anthracene and Argon

I. Introduction

In the previous chapter some general conclusions about the dissociation of stilbene-rare gas complexes were made: (1) intramolecular vibrational energy redistribution (IVR) appears to precede vibrational predissociation (VP) in general; (2) the overall dissociation in stilbene-He is mode specific, occurring most rapidly from out-of-plane modes; and (3) few of the accessible products are formed, but the VP rate of the major product is approximately that given by simple RRKM theory. In order to assess the generality of those results, the dissociation of anthracene-argon was studied.

Anthracene-argon differs in a number of important aspects from the stilbene complexes discussed in Chapter 4. Anthracene has higher symmetry than stilbene, is more rigid and does not have large-amplitude, low-frequency out-of-plane bending modes. Furthermore, the vibrational structure of the excitation spectrum of anthracene is much different. The excitation spectrum of stilbene has a large number of bands corresponding to the combinations and overtones of a few of these low frequency modes and becomes very congested above the isomerization threshold at 1200 cm^{-1}. In the excitation spectrum of anthracene, several fundamental modes are accessible with considerable intensity up to $\sim$1400 cm^{-1} and are well resolved from other bands. Finally, anthracene has similar but inequivalent binding sites for the rare gas atoms so that geometrical isomers can conceivably be studied.

Like stilbene, the spectroscopy and dynamics of bare anthracene have been studied before. The high resolution excitation and fluorescence spectra of S_1 anthracene in a free-jet expansion have been studied and the observed vibrational structure assigned.[1] The fluorescence lifetime of the vibrational levels in S_1 below $\sim$4000 cm^{-1} have also been measured.[2] Below $\sim$1500 cm^{-1} the

lifetime varies erratically between 28 and 6 ns due to a mode dependence in the intersystem crossing rate. The dynamics of IVR have been studied in detail[3] and characterized according to the vibrational energy. Below 1290 cm^{-1}, no IVR is observed. Between 1290 and 1514 cm^{-1}, restricted IVR, redistribution amongst a few vibrational levels, is observed in the quantum beat modulated fluorescence decays.

The excitation spectrum of anthracene in an argon molecular beam expansion has been reported for the region up to 400 cm^{-1} red of the origin.[4] Bands are assigned as anthracene-Ar_n, n=1-10, according to the spectral shift and the integrated peak intensities. The absorption bands for anthracene-Ar_n, n=1 and 2, have shoulders on the red and blue edges, respectively, which are assigned to different isomers of the complexes on the basis of simple calculations of the potential energy surface of the rare gas atom. Intense absorptions at -43 cm^{-1} and -98 cm^{-1} with respect to the anthracene origin are assigned to the electronic origin of the stable isomers of anthracene-Ar and anthracene-Ar_2. A band at -137 cm^{-1} is assigned to anthracene-Ar_3. Keelan[5] has measured this spectrum at a lower signal-to-noise up to anthracene S_1+800 cm^{-1}. Bands assigned to the anthracene-Ar_1 complex were observed 40 cm^{-1} red of the origin(0_0^0), the 12_0^1 band at 385 cm^{-1}, the 10_0^1 band at 755 cm^{-1}, and the 12_0^2 band at 766 cm^{-1}. Bands assigned to the anthracene-Ar_2 complex were observed 97 cm^{-1} red of the 0_0^0 and 12_0^1 bands. Only one band was observed in the vicinity of 766-98 or 755-98 cm^{-1}, however, at 766-86 cm^{-1}, and the assignment is not known.

Sequence transitions from thermally populated vibrational levels in the molecular beam expansion were also observed 23, 43, and 55 cm^{-1} red of the anthracene origin in the excitation spectrum.[4,5]

II. Experimental

The experimental arrangement for the work with anthracene-Ar was nearly identical to that used for stilbene-Ar. A 1.5 x 10^{-3} M solution of DCM in a 3/2 (volume) mixture of ethylene glycol and benzyl alcohol was used in the dye laser and the visible output was doubled with a $LiIO_3$ second harmonic generation crystal. An Amperex XP2020 photomultiplier tube (PMT) was used to detect fluorescence. Although the temporal system response function measured with this photomultiplier is broader than the response measured with the microchannel PMTs used in the work with stilbene, the quantum efficiency of the photocathode is about three times greater. The response function with this PMT was generally 400 ps. As with the stilbene work, well fit single exponential fluorescence decays of the bare molecule were regularly measured as a control experiment. Simulating data as discussed in Chapter 3, temporal data with risetimes as short as ~75 ps could be accurately fit for data with 4500 detected photons at the maximum of the decay curve.

The concentration of the complex in the molecular beam expansion, determined by measuring broad-band (50Å) fluorescence, was a maximum for an expansion of ~1% Ar in He. Underlying emission from hot bands was reduced using a backing pressure of 100 psi in the molecular beam expansion and could be reduced further by lowering the temperature of the anthracene reservoir.

Decay rates of ~1 ns were reproducible to ~10%. Decay rates of ~15 ns varied as much as 30% because of the relatively short time scale of the measurement compared to the lifetime. In the following section, only the fast lifetimes are discussed. Average values are reported in the text for the lifetimes from data curves that were measured more than once.

III. Results

Anthracene-Ar$_1$ 0_0^0: The fluorescence spectrum of anthracene-Ar excited to

the vibrationless level (Figure 1) is identical, except for a 40 cm^{-1} red shift, to the fluorescence spectrum of the vibrationless state of bare anthracene. The fluorescence decay is well fit as a single exponential with a lifetime of 13 ns.

Anthracene-Ar_1 12_0^1: The fluorescence spectrum of this band of the complex exciting the absorption on resonance, to the red $\sim$3 cm^{-1} and to the blue $\sim$3 cm^{-1} is shown in Figure 2. Most of the emission is assigned to the initially excited level of the complex and the intensity of the emission decays in 12.5 ns, with no discernable rising or additional decaying component (see Figure 3). Time resolved data for the bare vibrationless anthracene that is formed at this excitation depends on the spectral resolution. At high (1.6Å) resolution (Figure 4), three components in the temporal data are distinguished, but do not fit the kinetic scheme of Chapter 3.

Anthracene-Ar_2 12_0^1: The fluorescence spectrum of this level is shown in Figure 5. Most of the emission is assigned to the initially excited level, anthracene-Ar_2 12_0^1. The small peak at 3617.0Å is relatively more intense when the excitation wavelength is tuned $\sim$9 cm^{-1} to the blue and is assigned to the origin of anthracene-Ar. The remaining emission is similar to the spectrum of the vibrationless level, but is unassigned. The time resolved data for the anthracene-Ar_2 12_1^1 band at 3624.0Å fits as with two decaying components, one with a 2.0 ns lifetime and another with a 8.9 ns lifetime. The emission from the unassigned band at 3622.0Å fits as a biexponential with a 2.1 ns rising component and no fast decaying component. This biexponential and the data with the 2.0 ns decay are shown in Figure 6. The data for the anthracene-Ar_1 0_0^0 band is fit as a triexponential with lifetimes of 940 ps and 275 ps in Figure 7.

Anthracene-Ar_1 12_0^2 and 10_0^1: The data for these two levels is similar. In the fluorescence spectra (Figure 8) the emission is similar to emission from the

vibrationless level of bare anthracene, but is red shifted -9 and -25 cm^{-1}. The band at 3567.5Å in the 12_0^2 spectrum and the band at 3627.0Å in the 10_0^1 spectrum can each be assigned to resonant emission.[1a] The decay of the fluorescence at 3567.5Å in the 12_0^2 spectrum, measured with relatively low spectral resolution (8.0Å), was fit with three decaying components, the most prominent having a lifetime of 1.5 ns (Figure 9). The decays of each of the two origin-like bands in the anthracene-Ar_1 12_0^2 spectrum could be fit as triexponentials with lifetimes of 1.5 ns and 246 ps (Figure 9), while the temporal data for the same bands in the anthracene-Ar_1 10_0^1 spectrum fit with lifetimes of 1.5 ns and 513 ps. The relative intensity of the two bands in the fluorescence spectrum does not change perceptibly when the excitation wavelength is off resonance.

Anthracene-Ar_2 $12_0^2/10_0^1$: As discussed in the introduction, only one band in the excitation spectrum is observed that can be attributed to these excitations. The fluorescence spectrum of that band is shown in Figure 10 and can be assigned as anthracene-Ar_1 0^0. Exciting the blue edge of the excitation band, the weak emission from the origin of bare anthracene becomes more intense. The time resolved data for the emission from the 1:1 complex fits a triexponential with lifetimes of 575 ps and 278 ps (Figure 11). For the same emission band but exciting the blue edge of the excitation band, the temporal data fits as a triexponential with lifetimes of 671 ps and 107 ps.

Anthracene-Ar_3 12_0^2: Exciting 131 cm^{-1} to the red of anthracene S_1+766 cm^{-1}, the spectrum in Figure 12 was recorded. Most of the emission is assigned as anthracene-Ar_2 0^0. The temporal decay of the 0_0^0 band is fit as a triple exponential with fast lifetimes of 475 and 262 ps in Figure 13.

Anthracene-Ar_1 6_0^1: The emission from the complex excited to S_1+1380 cm^{-1} (Figure 14) is broad origin-like fluorescence and depends on the precise

excitation wavelength, as in the bare molecule. The bluest band in the emission is shifted 8 cm^{-1} to the red of the 0_0^0 band of the bare molecule. None of the bands can be assigned to known, optically active modes. The most intense band, at 3617.0Å, has two overlapping rises of 680 and 167 ps when exciting on resonance. Tuning red, a single 906 ps rise is fit in the temporal data for this emission band (Figure 15). The decay of the band at 3612.0Å also depends on the excitation wavelength, changing from a curve with a partial rise with a 753 ps risetime to a triexponential with fast lifetimes of 872 and 212 ps when the absorption is excited to the red (Figure 15).

Anthracene-Ar_2 6_0^1: The dispersed fluorescence spectrum of this band excited on resonance, to the blue and to the red, is shown in Figure 16. Again, the emission cannot be assigned in terms of optically active modes and appears to be composed of origin-like sequence bands. Examples of the temporal data for the bands at 3611.4Å and 3613.7Å are shown in Figure 17 and can be fit as triexponentials with fast lifetimes of 868 and 169 ps and of 563 and 203 ps, respectively. The temporal data for the band at 3623.3Å fits as a biexponential with a 190 ps rise.

IV. Discussion

A. Separation of IVR and VP

The results reported in the previous section can all be readily interpreted using the kinetic model of Chapter 3. For every excitation except anthracene-Ar_1 12_0^1, triexponentials are accurately measured that match the kinetic scheme for a two step dissociation. For the temporal data on the vibrationless anthracene formed at that excitation, and for some of the bands at 1380 cm^{-1}, it is likely that overlapping bands are contaminating the data. Nonetheless, it is clear that in these complexes IVR is preceding VP in the dissociation.

When only a single triexponenetial decay is measured, it is not possible to determine which of the two short lifetimes is due to IVR and which is due to VP. Fast decays identifying the first lifetime were measured in these experiments only for anthracene-Ar_2 12_0^1 and anthracene-Ar_1 12_0^2. For anthracene-Ar_1 and anthracene-Ar_2 excited to S_1+1380 cm^{-1}, the fact that the same fast lifetime (e.g., ~900 and ~200 ps, respectively) was measured for different bands suggests (according to the kinetic model) that these are the IVR lifetimes for those excitations. Taking trends into consideration along with these measured lifetimes of the initial decay, IVR and VP lifetimes can be distinguished as listed in Table 1.

Several interesting points are apparent from the data. For the more stable isomers at 385 cm^{-1}, the IVR "turns on" when the second argon atom is bound to the anthracene molecule. Ignoring the effect of the different possible binding sites of the two isomers, this would suggest that a "threshold" vibrational state density had not been reached for the 1:1 complex at 385 cm^{-1}. In stilbene-Ar, on the other hand, IVR was observed at only 198 cm^{-1} of excess vibrational energy, well below the bond energy for that complex.

According to Henke et al.[4] the two bands observed for the 1:1 complex correspond to different structural isomers. Comparing the time resolved data for these bands, the fact that IVR is observed for the only one of the two 1:1 isomers suggests that the IVR may be induced for dynamical reasons, perhaps the reduction of symmetry if Schlag's assignments are correct.

All the rates reported here are hundreds of picoseconds long, up to 2 ns. The longest lifetime measured in any of the stilbene complexes was 250 ps for IVR in stilbene-Ar at 198 cm^{-1}.

Finally, all of the VP lifetimes are on the order of 300 ps. Although they

vary by a factor of ~8, the variation is not monotonic with vibrational energy-at 385 cm^{-1}, the VP lifetime of the less stable isomer is 321 ps while for the 1:2 complex at 1380 cm^{-1}, a 868 ps lifetime is attributed to VP. Such differences could only be due to mode-specific effects in the VP dynamics. Another interesting suggestion of mode-specificity is the fact that the VP rates for anthracene-Ar + 766 cm^{-1}, anthracene-Ar_2 +~760 cm^{-1}, and anthracene-Ar_3 + 766 $cm^{-1}$are all the same within experimental error.

B. IVR and the Vibrational State Density

In the previous chapter it was shown that the addition of the dense set of van der Waals vibrational states to those of bare stilbene increases the total vibrational state density such that many bath modes are within an energy corresponding to the laser bandwidth from the initially excited, optically active, single vibrational level. Many levels are therefore accessible for vibrational redistribution. Similar calculations of the van der Waals potential and the corresponding vibrational state density were made for anthracene-Ar. IVR is observed in stilbene, anthracene, stilbene-Ne, and stilbene-Ar when the vibrational state density is such that more than about ten bath states are close enough in energy to be coherently excited and resolved temporally.

At 385 cm^{-1} the total vibrational state density in anthracene-Ar, including the full anharmonicity of the van der Waals modes and taking D_0=517 cm^{-1} (as calculated from the Lennard-Jones potential), is 256/ cm^{-1}. For every excitation above this energy dissipative IVR is observed, as would be expected from this value of the state density and by comparison of this state density with that calculated for other observations of IVR. At this energy, however, (ignoring the contribution from the less stable isomer), only fluorescence assigned entirely to the initially excited state is observed and no time-dependent process other

than fluorescence is observed. On the other hand, at 198 cm^{-1} in stilbene-Ar where ρ ~70/ cm^{-1}, dissipative IVR occurs in 250 ps. At 594 cm^{-1} in the stilbene-Ar complex where ρ=6678/ cm^{-1} according to a count of *harmonic* vibrational levels, τ_{ivr} decreases to <16 ps. In anthracene-Ar, τ_{ivr}=1.4 ns at 755 and 766 cm^{-1} and τ_{ivr}=880 ps at 1380 cm^{-1} where $\rho_{harmonic}$ ~1833 and 71230/ cm^{-1}, respectively.

As referred to in Chapter 4, Lahmani[6] has shown that the number of coupled levels affects both the rate of the IVR and the extent to which it is dissipative, i.e., is accurately reproduced by kinetic equations, having no quantum oscillations or recurrances. The rate, of course, also depends on the average coupling strength. Thus, the relatively long redistribution lifetimes compared to stilbene and stilbene-Ar and the insensitivity of the redistribution lifetimes to the excess vibrational energy, to the vibrational state density, suggest that the coupling is relatively ineffective and does not couple the initially excited state with all available bath states.

C. Vibrational Predissociation-Comparison with Theory

RRKM rates were calculated by directly counting harmonic levels as discussed by Khundkar et al.[7] and in the previous chapter. The van der Waals vibrational frequencies were taken to be 43.7, 9.94, and 6.44 cm^{-1}, as calculated from the fitted potential. The calculated rates and lifetimes, taking D_0=450 and 550 cm^{-1}, are shown in Figure 18. These calculated rates agree with experiment only to the extent that they are relatively independent of energy for excess vibrational energies greater than D_0 by ~200 cm^{-1}. The calculated high energy lifetime is ~100 times smaller than those measured.

According to this calculation, one would not expect to see much change in the measured lifetimes since the accessible vibrational energies in the complex are

considerably greater than D_0. The calculated lifetimes drop rapidly with excess vibrational energy. The difference in the order of magnitude of the lifetime is surprising, however, especially in light of the agreement of the RRKM rates with those measured for the stilbene complexes. Agreement would be improved if the number of levels in the transition state ($N^\dagger$) was uniformly smaller than calculated. This would be the case if D_0 were taken to be substantially larger. The RRKM rate at 1400 cm^{-1} is not comparable to those measured until D_0 is taken to be ~1000 cm^{-1} (where k_{RRKM}=1/255 ps), well over the experimental lower limit of 755 cm^{-1}. Another way in which the number of levels in the transition state would be smaller is if some number of anthracene modes did not participate in the dissociation and were ignored in the direct count used to calculate the RRKM rate. When half of the anthracene modes are ignored in the calculation of both $N^\dagger$ and ρ, the final RRKM rates are not changed substantially-the changes in $N^\dagger$ and ρ are comparable. Thus, to improve the calculated RRKM rate, $N^\dagger$ would have to be lowered unilaterally.

As for the stilbene complex, the momentum-gap rates depend sensitively on the identity of the unknown intermediate state. Since the mass of stilbene is nearly the same as the mass of anthracene, the dependence of the momentum-gap rate on the van der Waals stretching quantum number and the energy into translation is very nearly the same as discussed in Chapter 4 for stilbene-Ar.

D. Mode-Selectivity

The data for the dissociation from the levels in anthracene-Ar at S_1+755 and 766 cm^{-1} provide an interesting assessment of the extent to which the dissociation of these complexes is statistical or mode selective. The dissociation occurs at essentially the same excess vibrational energy, but two different A_g modes of anthracene are initially excited. Furthermore, the band at 766 cm^{-1}

is the overtone of the band at 385 cm^{-1}, while the band at 755 cm^{-1} is a fundamental vibration. As is evident from Figure 8 , the product state distribution of each of these excitations are identical: the only difference in the dispersed fluorescence spectra of these levels are the weak resonant emission bands at 3567.5Å and 3627.0Å. The time resolved data shows that the redistribution rates are also identical. Nonetheless, the predissociation rates differ by a factor of $\sim$2, being faster when the overtone is initially excited. This behavior contrasts sharply with the excitation mode specificity observed in stilbene-He. In that case, excitation of overtones of out-of-plane bends of different symmetry than a particular in-plane bend led to a great difference in the dissociation rates, presumably the IVR rates. In this case, different in-plane vibrations of the same symmetry have identical redistribution rates, but somewhat different predissociation rates from the intermediate levels formed in the redistribution.

V. Conclusions

In this chapter the results of picosecond time resolved experiments on the dissociation of van der Waals complexes of anthracene and argon excited to four different single vibrational levels of anthracene are reported and discussed.

The time resolved results clearly show that redistribution precedes predissociation for every excitation for which dissociation is observed. IVR is observed at much lower energies than in the bare molecule. As with stilbene and the stilbene complexes, that fact can be accounted for by considering the drastic increase in the vibrational state density from the binding of the argon atom to the anthracene plane. The IVR rates, however, are about an order of magnitude larger than observed in the stilbene complexes and change more slowly with increasing energy. This suggests that the coupling of the van der Waals modes with the anthracene modes is weaker or not as complete as the coupling of the

van der Waals modes with the stilbene modes that were studied. The relatively slow increase in the IVR rate with excess vibrational energy, with ρ_{vib}, suggests that the number of coupled levels or the strength of the coupling does not increase with vibrational energy to the same extent as in the stilbene complexes.

Measured predissociation rates vary by a factor of $\sim$8, but the variation is not monotonic with excess vibrational energy. For the anthracene-Ar complex excited to the levels at 755 and 766 cm^{-1}, the predissociation rates differ by a factor of two, even though the IVR rates and the product state distributions are identical. Thus, the VP dynamics are mode specific. These rates are an order of magnitude slower than calculated RRKM rates, which are essentially constant over about 200 cm^{-1} above the dissociation limit. The calculated RRKM rates would agree better with those observed if the number of levels in the transition state was reduced. Thus, both the IVR and VP rates suggest that the dissociation is not completely statistical even though it is dissipative.

REFERENCES

1. (a) W. R. Lambert, P. M. Felker, and A. H. Zewail, J. Chem. Phys. **81**, 2195 (1984).
(b) B. W. Keelan and A. H. Zewail, J. Chem. Phys. **82**, 3011 (1985).

2. W. R. Lambert, P. M. Felker, and A. H. Zewail, J. Chem. Phys. **81**, 2209 (1984).

3. P. M. Felker and A. H. Zewail, J. Chem. Phys. **82**, 2975 (1985).

4. W. E. Henke, Weijun Yu, H. L. Selzle, E. W. Schlag, D. L. Wutz, and S. H. Lin, Chem. Phys. **92**, 187 (1985).

5. B. W. Keelan, unpublished.

6. F. Lahmani, A. Tramer, and C. Tric, J. Phys. Chem. **60**, 4431 (1974).

7. L. R. Khundkar, R. A. Marcus, and A. H. Zewail, J. Phys. Chem. **87**, 2473 (1983).

Table 1

Observed vibrational predissociation and redistribution lifetimes

(in picoseconds)

	τ_{ivr}	τ_{vp}
anthracene-Ar 385 cm^{-1}	–	–
isomer	1120	321
anthracene-Ar_2 385 cm^{-1}	2000	–
isomer	940	275
anthracene-Ar 755 cm^{-1}	1500	513
anthracene-Ar 766 cm^{-1}	1500	246
anthracene-Ar_2 760 cm^{-1}	575	278
anthracene-Ar_3 766 cm^{-1}	475	262
anthracene-Ar 1380 cm^{-1}	872	212
	906	<150
anthracene-Ar_2 1380 cm^{-1}	169	868
	203	563
	190	<150

Figure Captions

Figure 1. Dispersed fluorescence spectra (spectral resolution, R=1.6Å) of anthracene-Ar excited to the vibrationless level of S_1.

Figure 2. Dispersed fluorescence spectra (spectral resolution, R=0.8Å) of anthracene-Ar S_1+385 cm^{-1} exciting the maximum of the excitation band, the red edge (-3 cm^{-1}) and the blue edge (+3 cm^{-1}).

Figure 3. Fluorescence decay of resonant emission from anthracene-Ar excited to the level 12^1 fit as a single exponential decay (τ=13 ns) convoluted with the system response function (also shown). χ^2_r=1.04 for this fit.

Figure 4. Triple exponential fit (τ_1=1.12 ns, Amplitude 1/Amplitude fluorescence =A_1/A_f=-1.10, τ_2=321 ps, A_1/A_f= 0.292, τ_f=20 ns, χ^2_r=1.11) of the time resolved emission of vibrationless anthracene produced in the dissociation of anthracene-Ar 12^1, exciting the blue edge of the excitation band. The upper residual is for the biexponential fit, for which χ^2_r=1.30.

Figure 5. Dispersed fluorescence spectra (R=1.6Å) of emission from anthracene-Ar_2 12^1 exciting the maximum of the absorption band, ~3 cm^{-1} to the red and ~9 cm^{-1} to the blue. The hot-band emission measured under identical conditions except for the absence of

argon in the molecular beam is also shown.

Figure 6. Rise and decay of emission from anthracene-Ar_2 12^1. For the decaying fluorescence at λ=3624.0Å, τ_1=1.9 ns, τ_f=8.5 ns, A_1/A_f=2.07 and χ_r^2=1.06. For the fluorescence with a rising component at λ=3622.0Å, τ_1=2.0 ns, τ_f=11.0 ns, A_1/A_f=-.933 and χ_r^2=1.02.

Figure 7. Triple exponential fit (τ_1=940 ps, A_1/A_f=-1.38, τ_2=275 ps, A_2/A_f=.39, τ_f=14 ns, χ_r^2= 1.04) of the time resolved emission of vibrationless anthracene-Ar produced in the dissociation of anthracene-Ar_2 12^1, exciting the blue edge of the excitation band. The upper residual shows the inadequacy of the best biexponential fit, for which χ_r^2=1.49.

Figure 8. Dispersed fluorescence spectrum (R=1.6Å) of anthracene-Ar 10^1 and 12^2 and the emission from the latter in the absence of argon in the molecular beam. The uppermost trace is a high resolution spectrum (R=0.48Å) of the 12^2 emission.

Figure 9. Temporal data for the decay (τ_1=1.44 ns, A_1/A_f=2.40, τ_2=272 ps, A_2/A_f=0.63, τ_f=5.6 ns, χ_r^2= 1.06) of intensity of the anthracene-Ar 12_1^2 band and the triexponential fit (τ_1=275 ps, A_1/A_f=0.231, τ_2=1.44 ns, A_2/A_f=-1.19, τ_f=23 ns, χ_r^2= 1.06) of the intensity from the unassigned band at -25 cm^{-1}.

Figure 10. Dispersed fluorescence spectrum (R=1.6Å) of anthracene-Ar_2 ex-

cited to approximately 760 cm^{-1}. The lower trace was recorded under identical conditions except for the absence of argon in the molecular beam. An asterisk marks the excitation wavelength.

Figure 11. Temporal data (τ_1=278 ps, A_1/A_f=0.951, τ_2=575 ps, A_2/A_f= -1.92, τ_f=11 ns, χ^2_r= 1.07) for the emission of vibrationless anthracene-Ar formed in the dissociation of anthracene-Ar_2 excited to ~760 cm^{-1}. χ^2_r=1.93 for the best biexponential fit.

Figure 12. Dispersed fluorescence (R=1.6Å) of anthracene-Ar_3 12^2. An asterisk marks the excitation wavelength.

Figure 13. Temporal data (τ_1=262 ps, A_1/A_f=1.33, τ_2=475 ps, A_2/A_f=-2.22, τ_f=14 ns, χ^2_r= 1.10) for the decay of anthracene-Ar_2 0^0_0 emission formed in the dissociation of anthracene-Ar_3 12^2.

Figure 14. Dispersed fluorescence spectrum of (R=1.6Å) of anthracene-Ar 6^1, hot band emission in the absence of argon, and the spectra exciting the red (-12 cm^{-1}) and blue (+12 cm^{-1}) edges of the excitation band. An asterisk marks the excitation wavelength.

Figure 15. Temporal data for two of the products of the dissociation of anthracene-Ar 6^1. The data which rises faster is emission from the band at λ=3617.0Åand is fit as a biexponential (τ=906 ps, A/A_f=-0.97, τ_f=13 ns, χ^2_r= 1.02). The more slowly rising emission was measured at λ=3612.0Å and is fit as a triexponential (τ_1=198 ps,

A_1/A_f=.342, τ_2=891 ps, A_2/A_f=-1.31, τ_f=17 ns, χ_r^2= 1.11).

Figure 16. Dispersed fluorescence spectrum (R=0.8Å) of anthracene-Ar_2 6^1 in the region of the anthracene origin, exciting on resonance, 12 cm^{-1} red, 7 cm^{-1}blue, and in the absence of argon in the expansion mixture.

Figure 17. Temporal data for two of the products of the dissociation of anthracene-Ar_2 6^1. The data which rises faster is emission from the band at λ=3613.7Åand is fit as a triexponential (τ_1=197 ps, A_1/A_f=-0.66, τ_2=536 ps, A_2/A_f=-1.61, τ_f=15 ns, χ_r^2= 1.12). The more slowly rising emission was measured at λ=3611.3Å and is also fit as a triexponential (τ_1=160 ps, A_1/A_f=.347, τ_2=884 ps, A_2/A_f=-1.29, τ_f=18 ns, χ_r^2= 1.05).

Figure 18. RRKM rates and lifetimes for the dissociation of anthracene-Ar complexes for D_0=450 cm^{-1} (crosses) and D_0=550 cm^{-1} (circles).

Figure 1

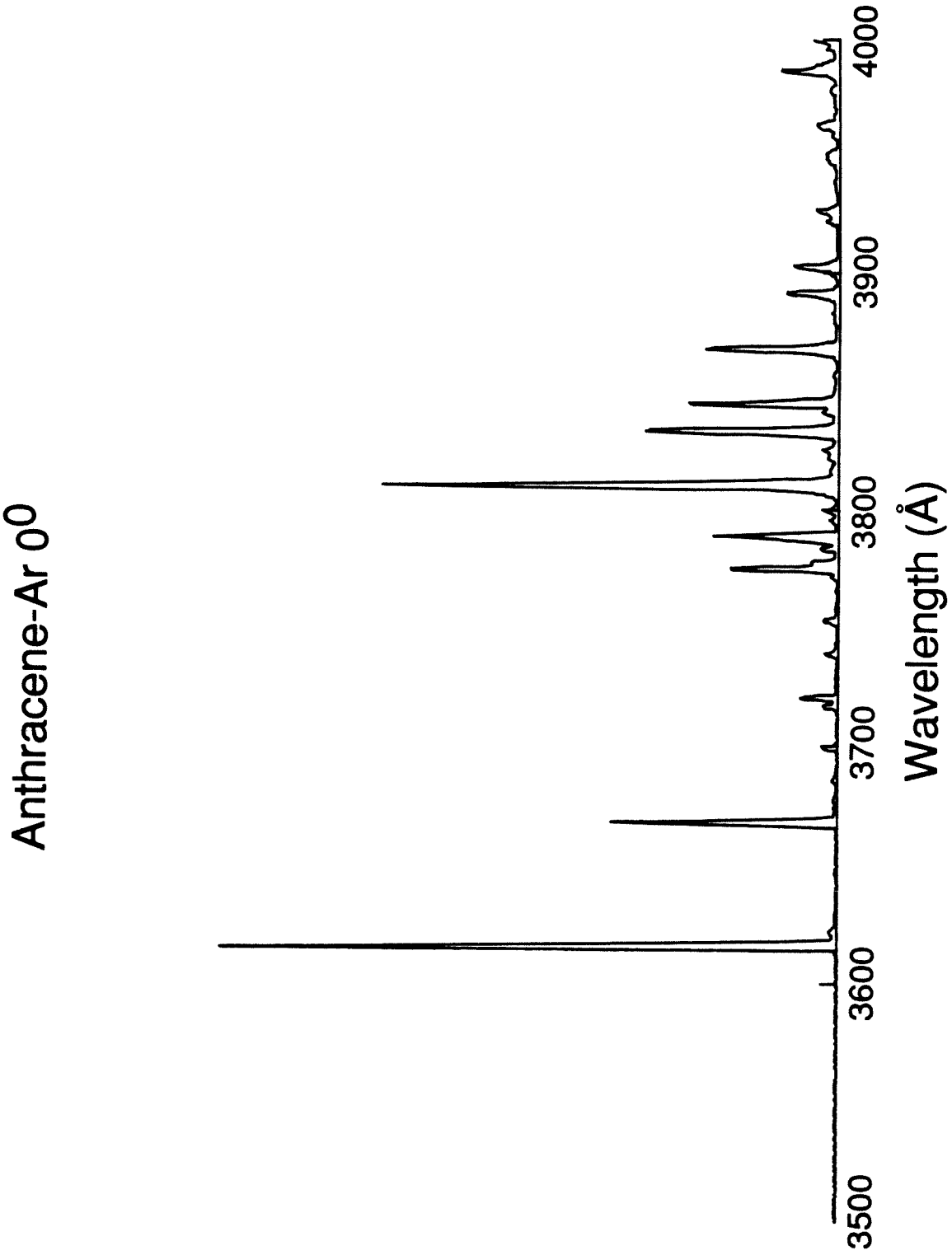

Figure 2

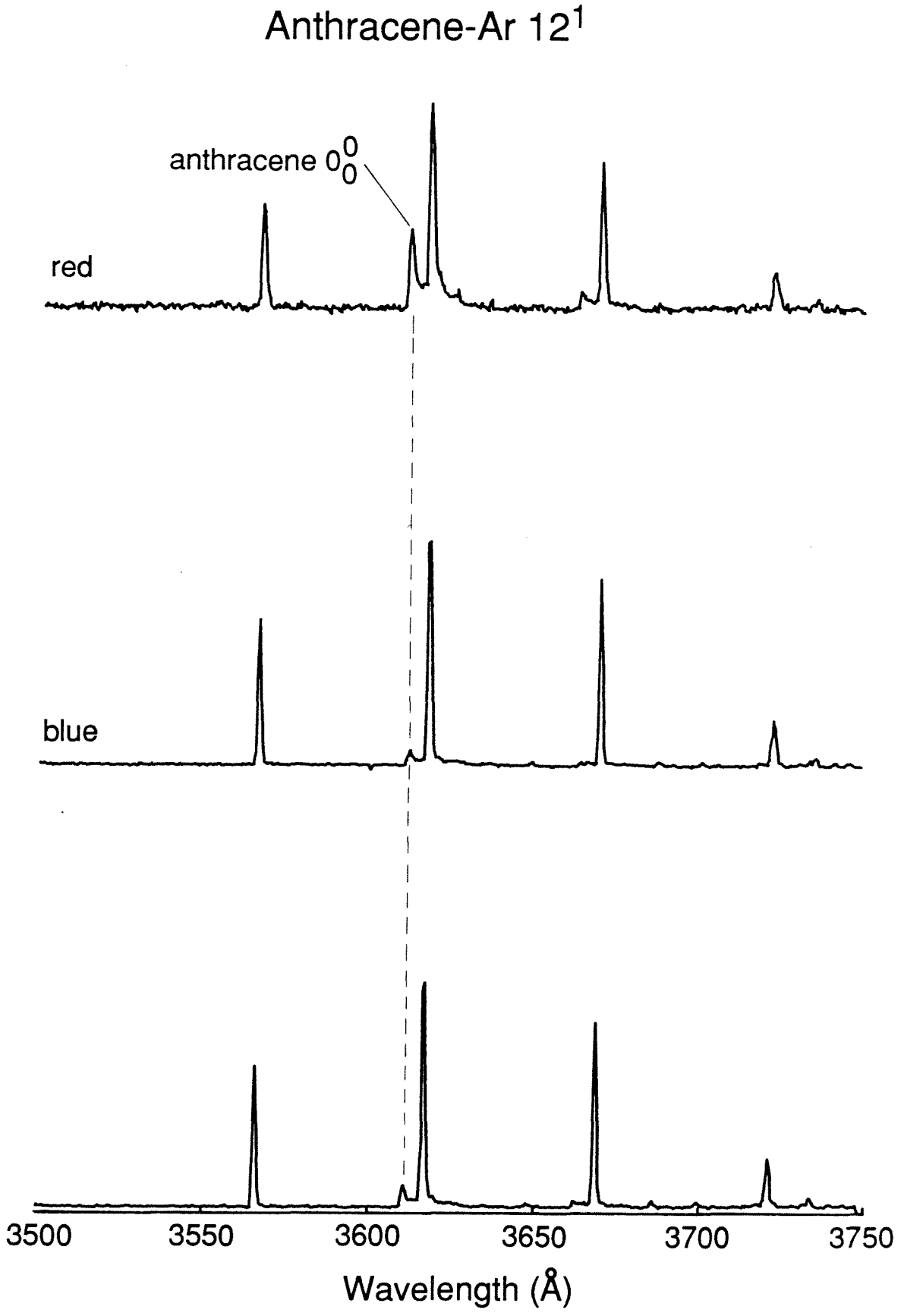
Anthracene-Ar 12[1]
anthracene 0_0^0
red
blue
3500
3550
3600
3650
3700
3750
Wavelength (Å)

Figure 3

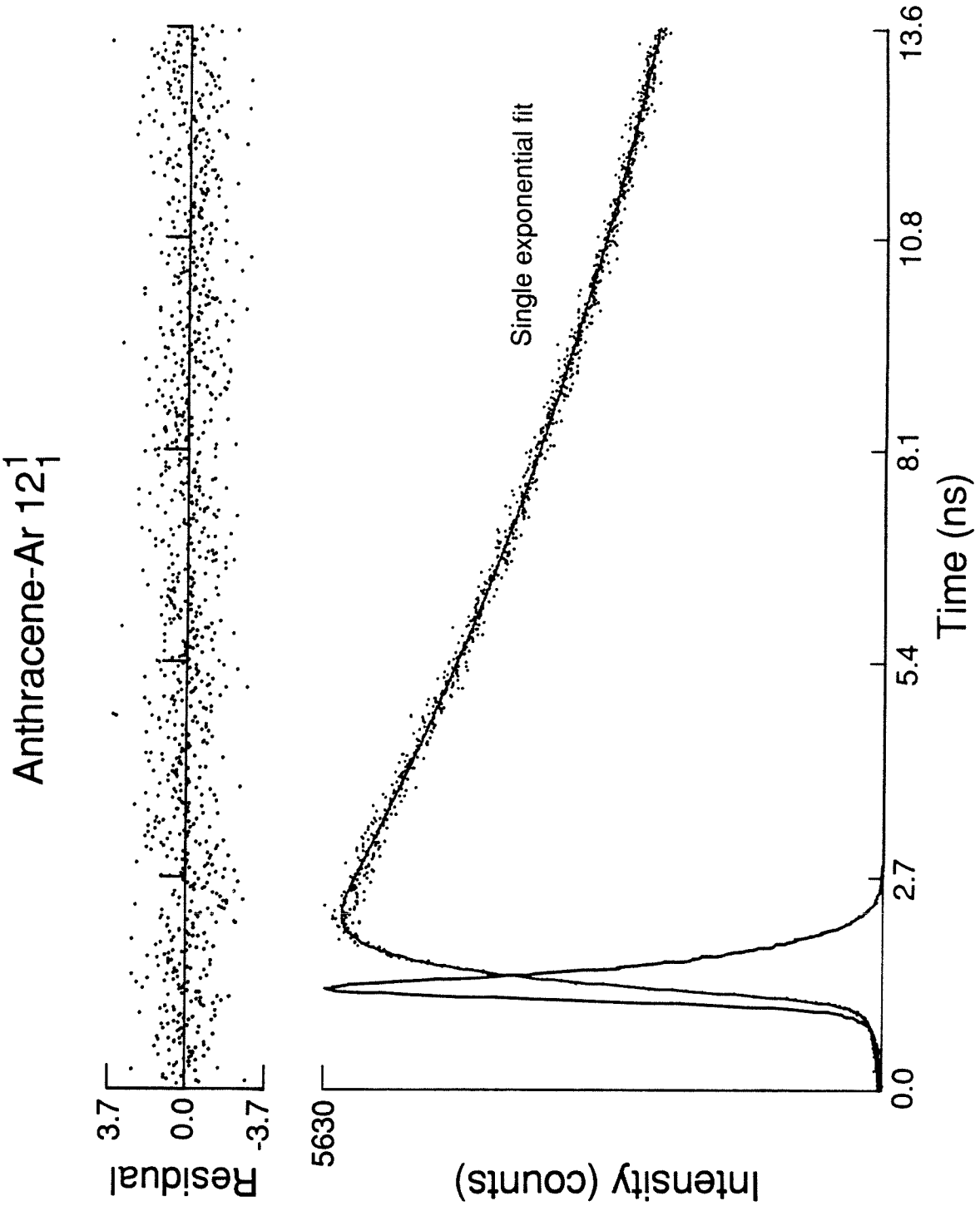
Anthracene-Ar 12 1 1
Residual
3.7
0.0
-3.7
Single exponential fit
Intensity (counts)
5630
0.0
2.7
5.4
8.1
10.8
13.6
Time (ns)

Figure 4

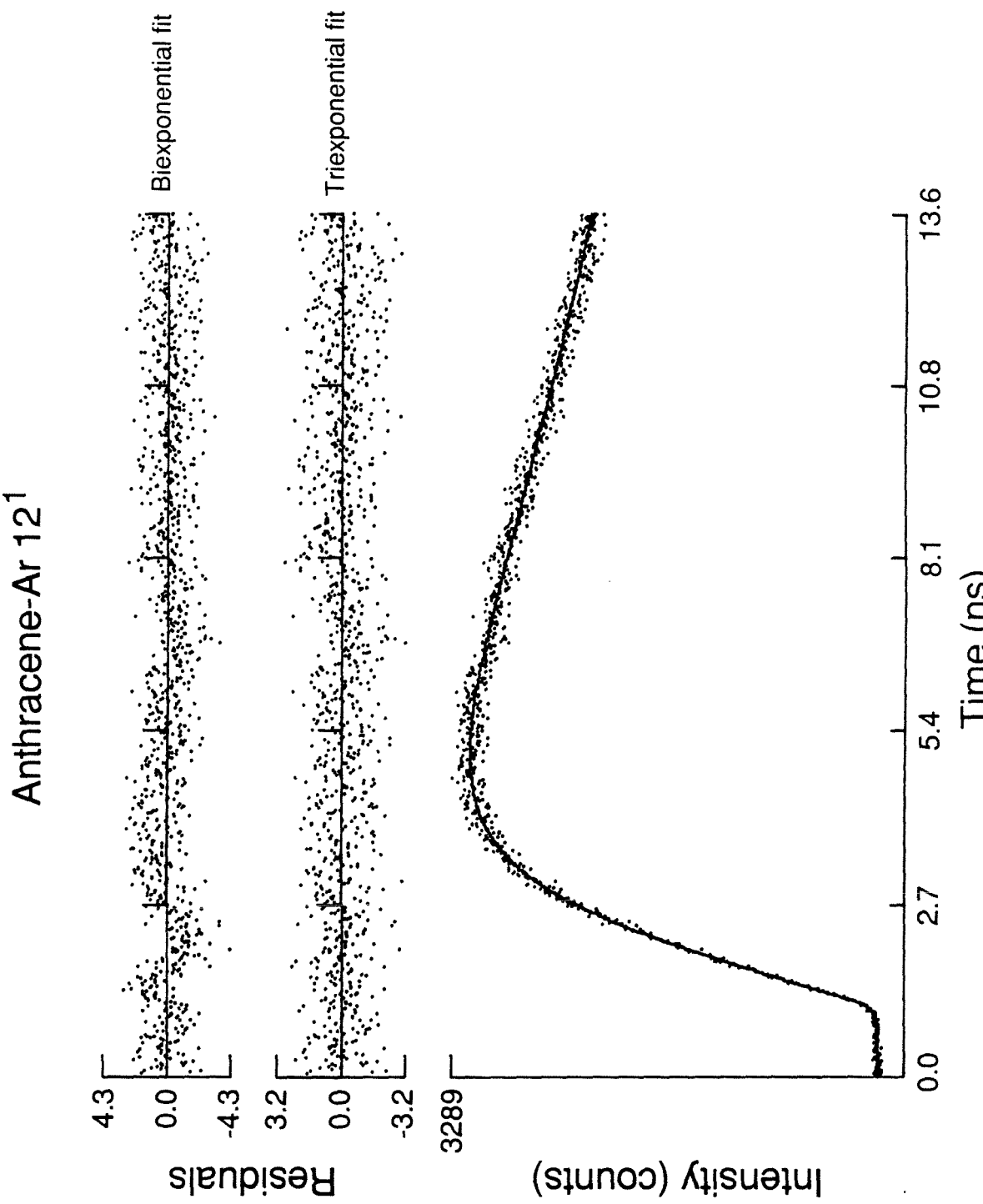
Anthracene-Ar 12[1]
Biexponential fit
Triexponential fit
Residuals
4.3
0.0
-4.3
3.2
0.0
-3.2
Intensity (counts)
3289
0.0
2.7
5.4
8.1
10.8
13.6
Time (ns)

Figure 5

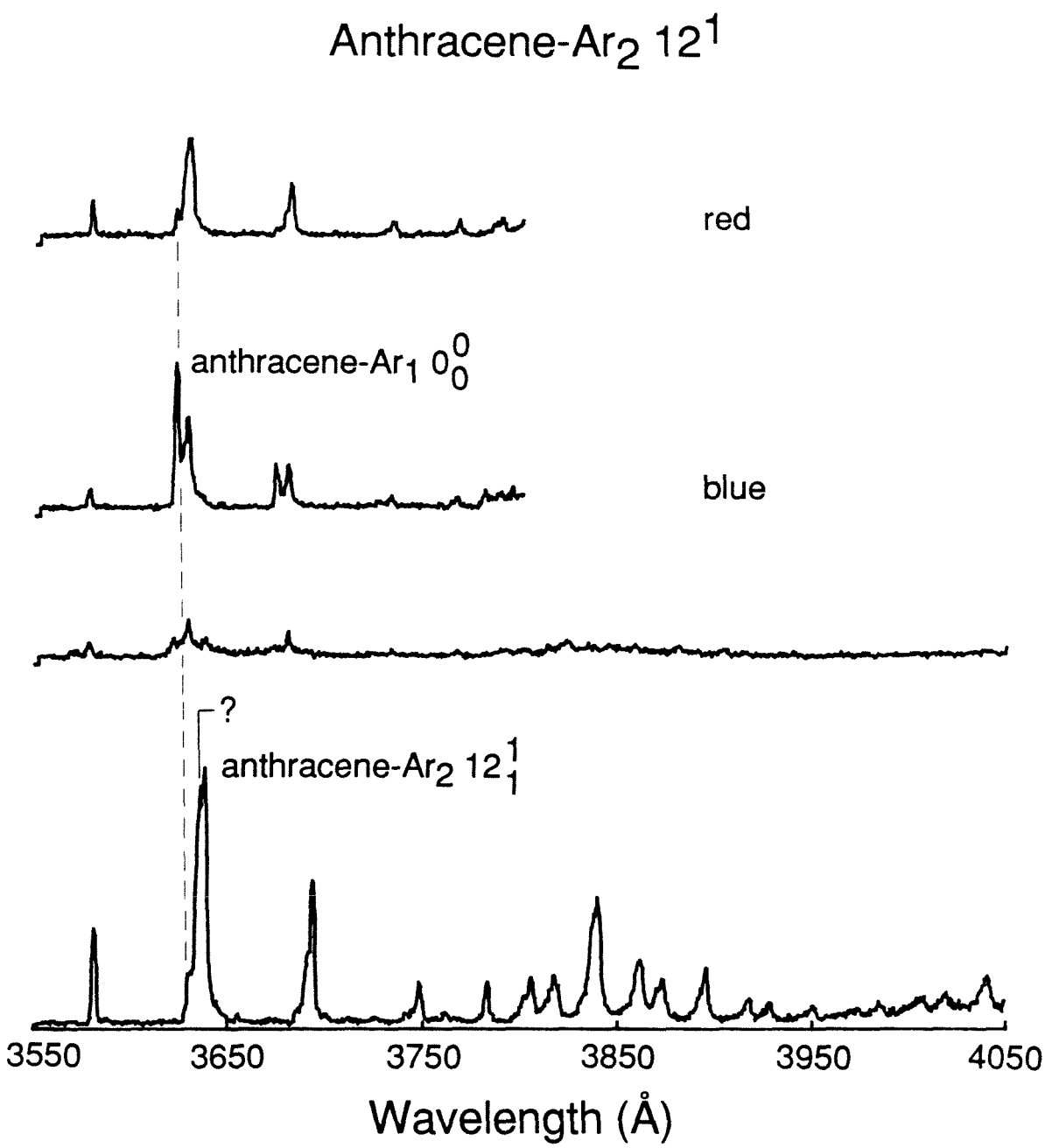
Anthracene-Ar2 12^1
red
anthracene-Ar1 0^0_0
blue
?
anthracene-Ar2 12^1_1
3550
3650
3750
3850
3950
4050
Wavelength (Å)

Figure 6

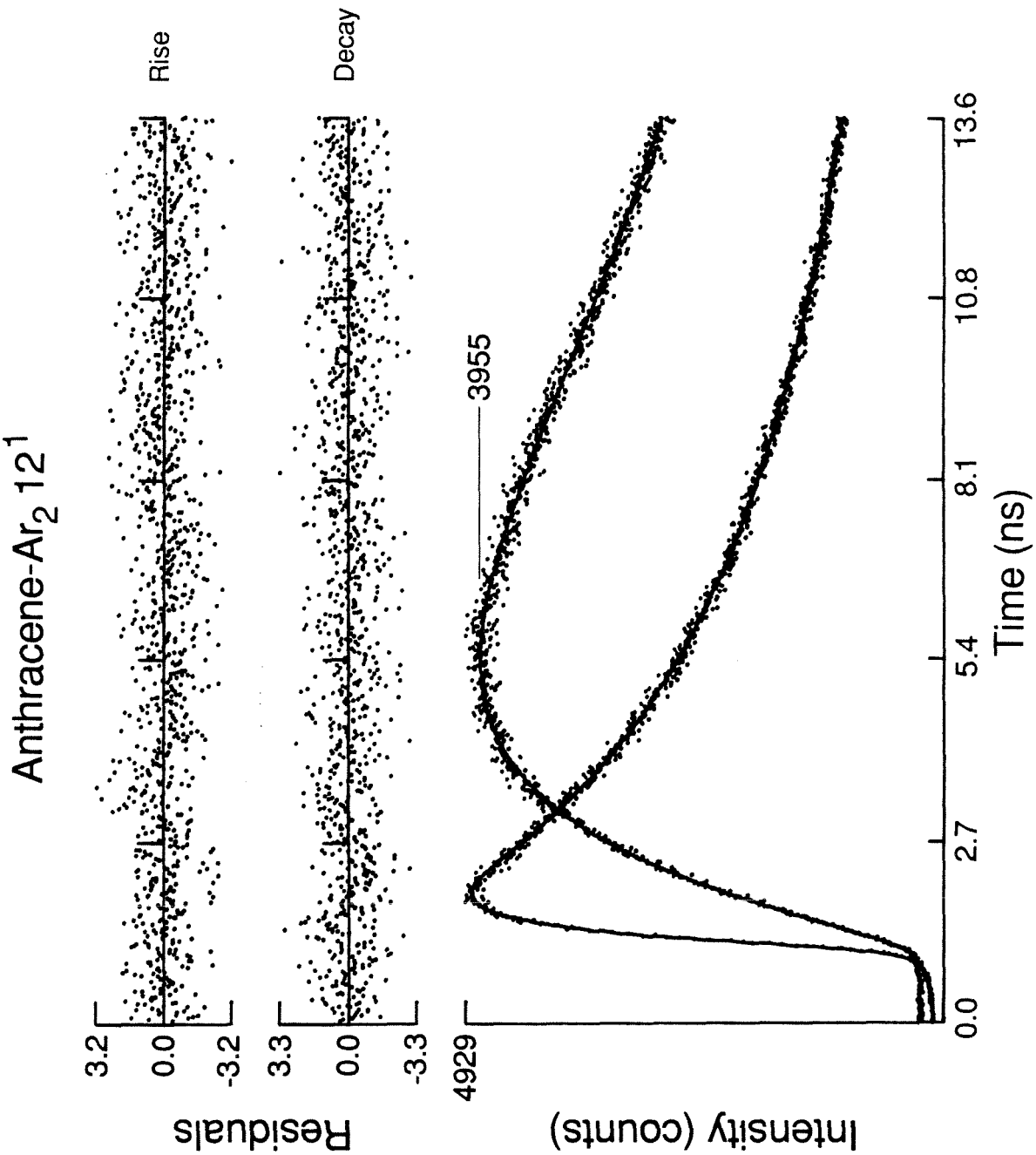
Anthracene-Ar2 12[1]
Rise
Decay
3.2
0.0
-3.2
3.3
0.0
-3.3
Residuals
4929
3955
0.0
2.7
5.4
8.1
10.8
13.6
Time (ns)
Intensity (counts)

Figure 7

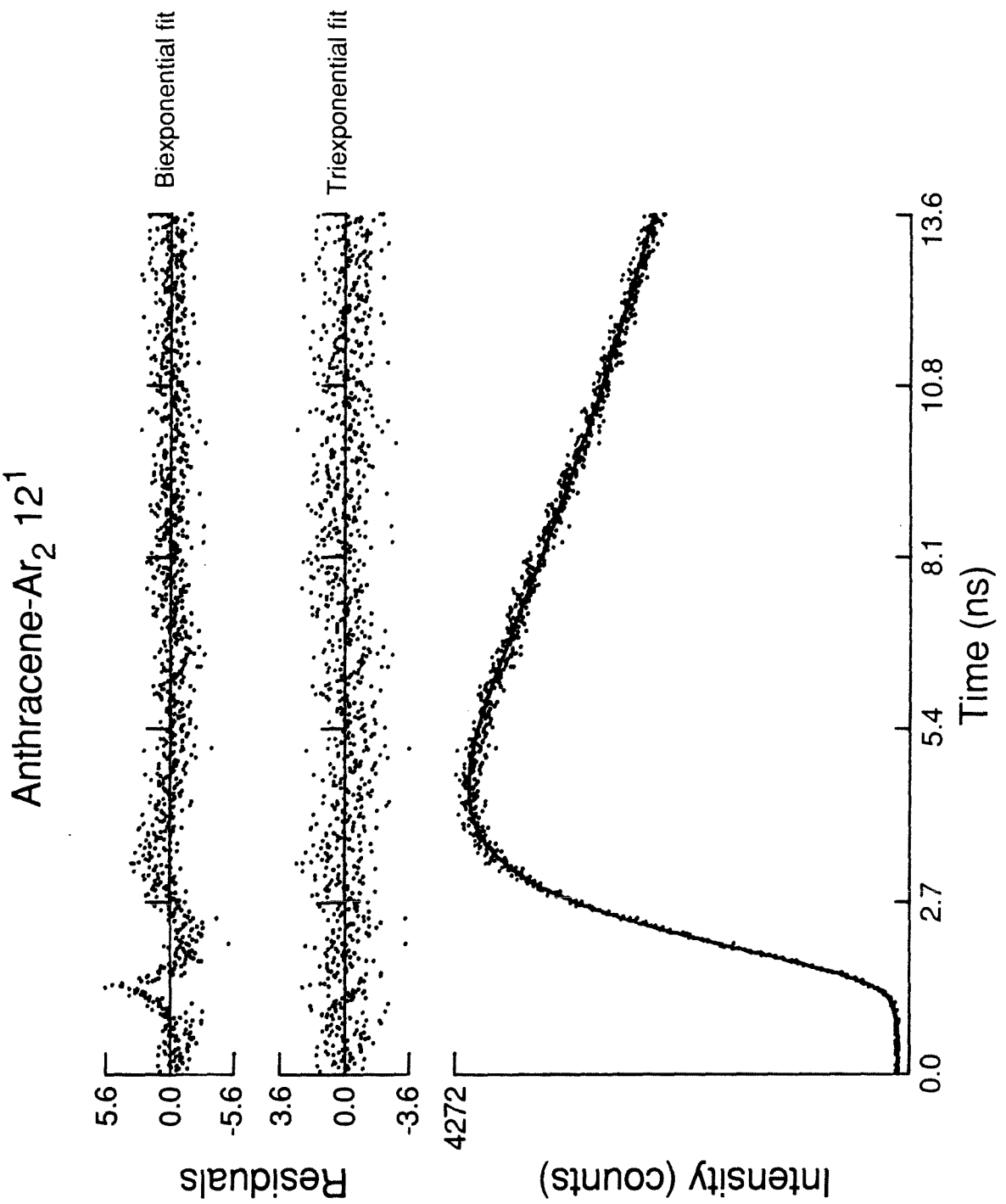
Anthracene-Ar2 12^1
Biexponential fit
Triexponential fit
Residuals
5.6
0.0
-5.6
3.6
0.0
-3.6
Intensity (counts)
4272
0.0
2.7
5.4
8.1
10.8
13.6
Time (ns)

Figure 8

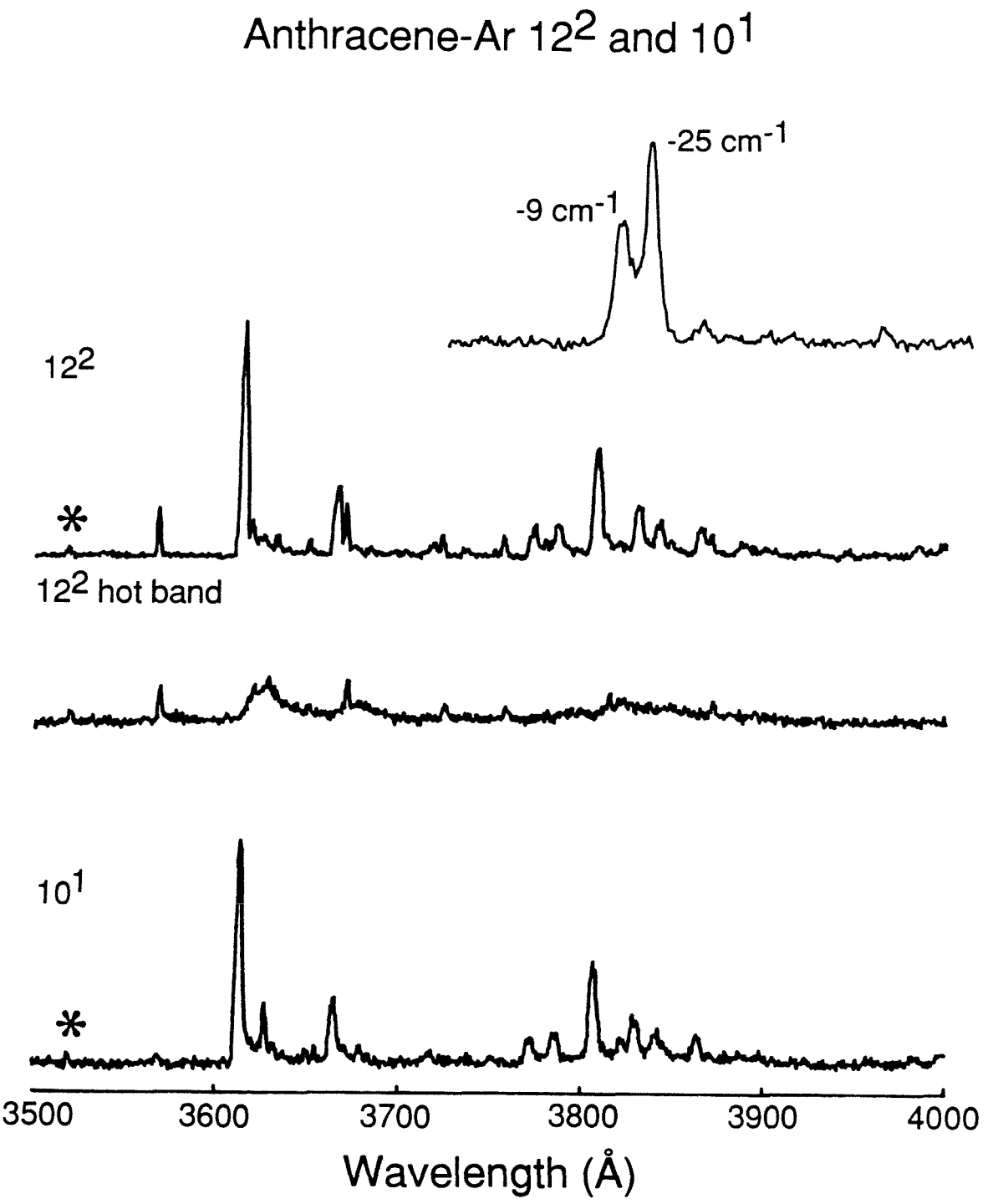
Anthracene-Ar 12² and 10¹
-25 cm⁻¹
-9 cm⁻¹
12²
*
12² hot band
10¹
*
3500
3600
3700
3800
3900
4000
Wavelength (Å)

Figure 9

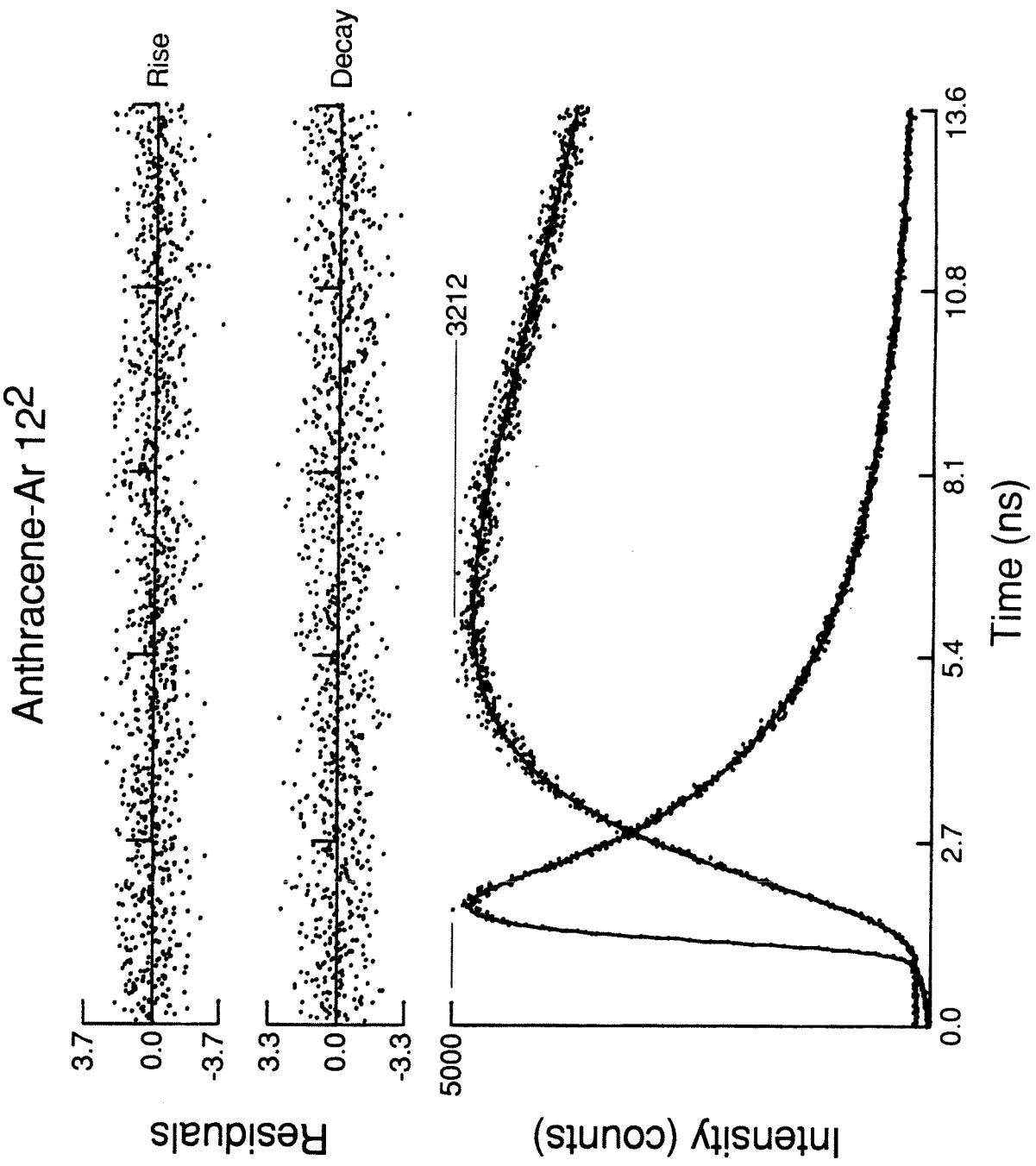
Anthracene-Ar 122
Rise
Decay
3.7
0.0
-3.7
3.3
0.0
-3.3
Residuals
3212
5000
0.0
2.7
5.4
8.1
10.8
13.6
Intensity (counts)
Time (ns)

Figure 10

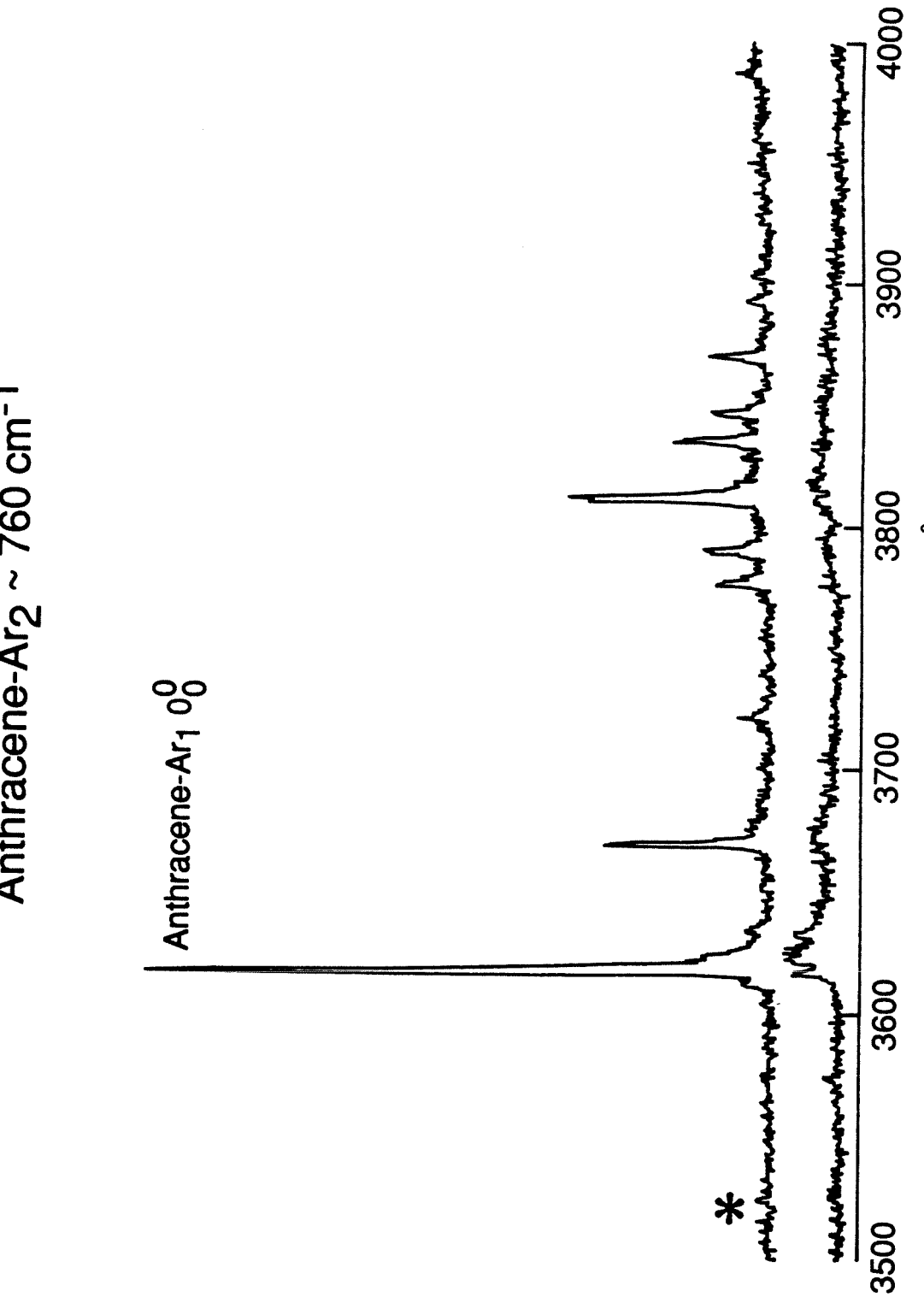
Anthracene-Ar2 ~ 760 cm-1
Anthracene-Ar1 0$_0^0$
*
3500
3600
3700
3800
3900
4000
Wavelength (Å)

Figure 11

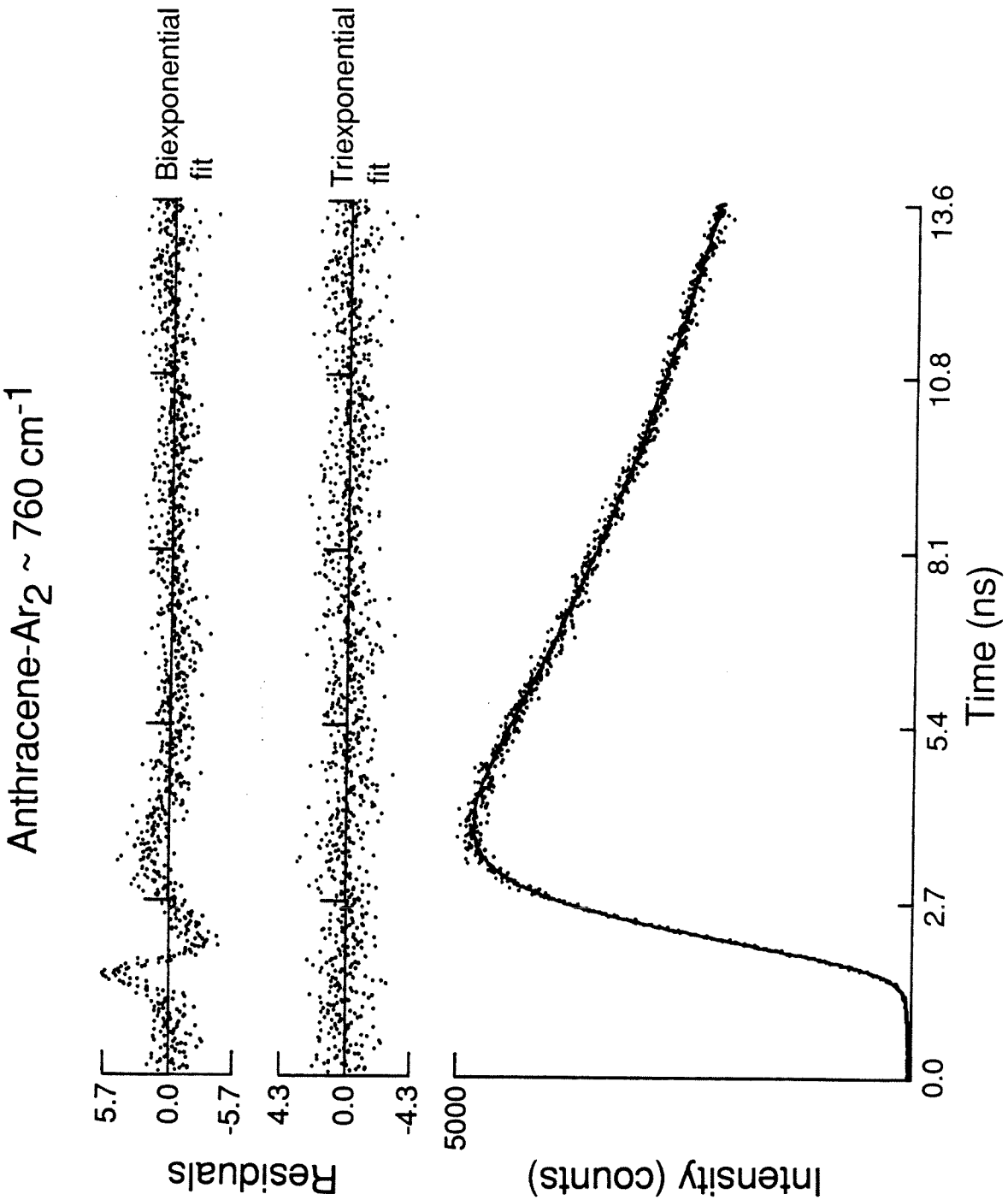
Anthracene-Ar2 ~ 760 cm-1
Biexponential fit
Triexponential fit
Residuals
5.7
0.0
-5.7
4.3
0.0
-4.3
Intensity (counts)
5000
0.0
2.7
5.4
8.1
10.8
13.6
Time (ns)

Figure 12

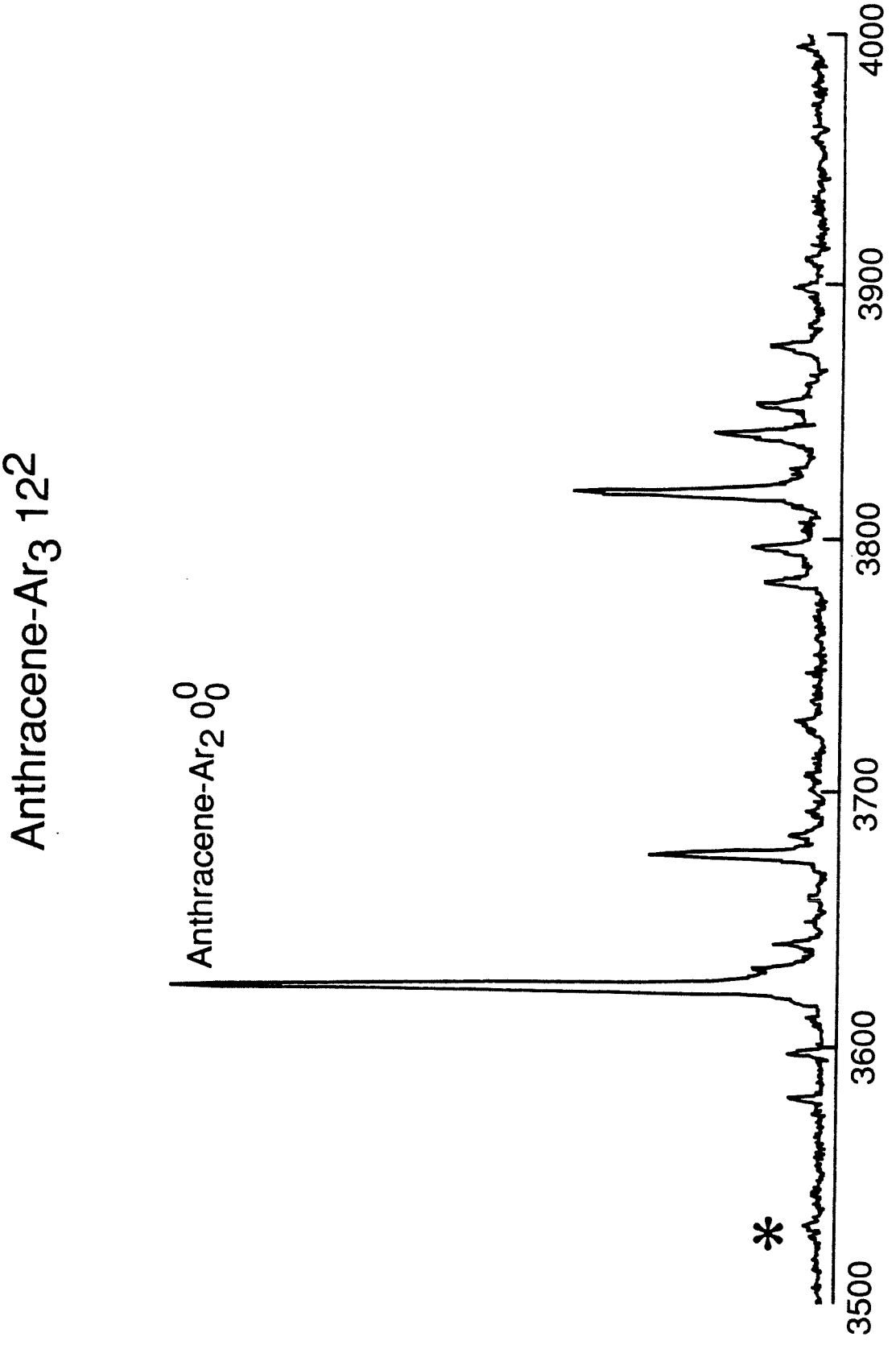
Anthracene-Ar3 122
Anthracene-Ar2 0_0^0
*
3500
3600
3700
3800
3900
4000
Wavelength (Å)

Figure 13

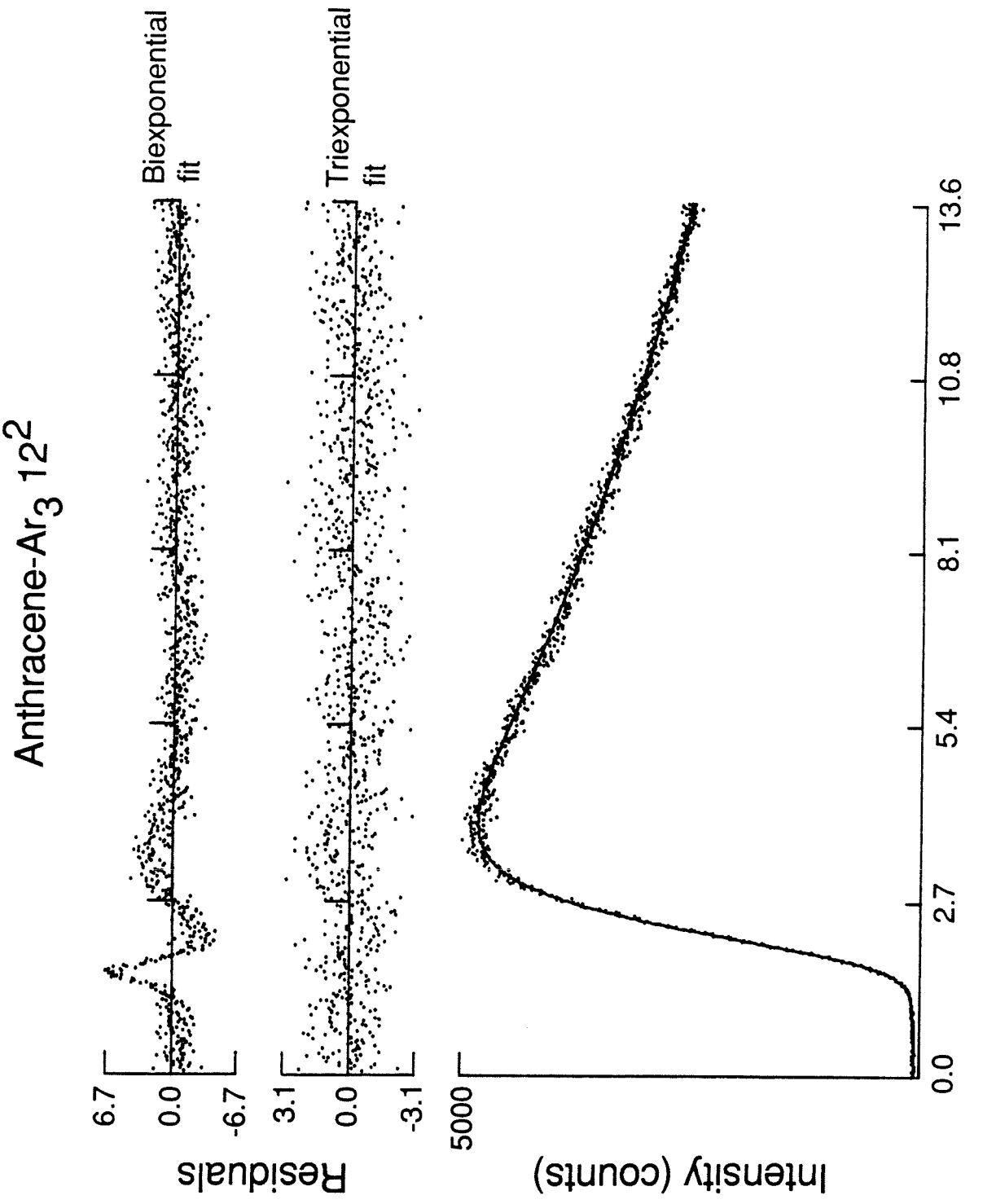
Anthracene-Ar3 12^2
Biexponential fit
Triexponential fit
Residuals
6.7
0.0
-6.7
3.1
0.0
-3.1
Intensity (counts)
5000
0.0
2.7
5.4
8.1
10.8
13.6

Figure 14

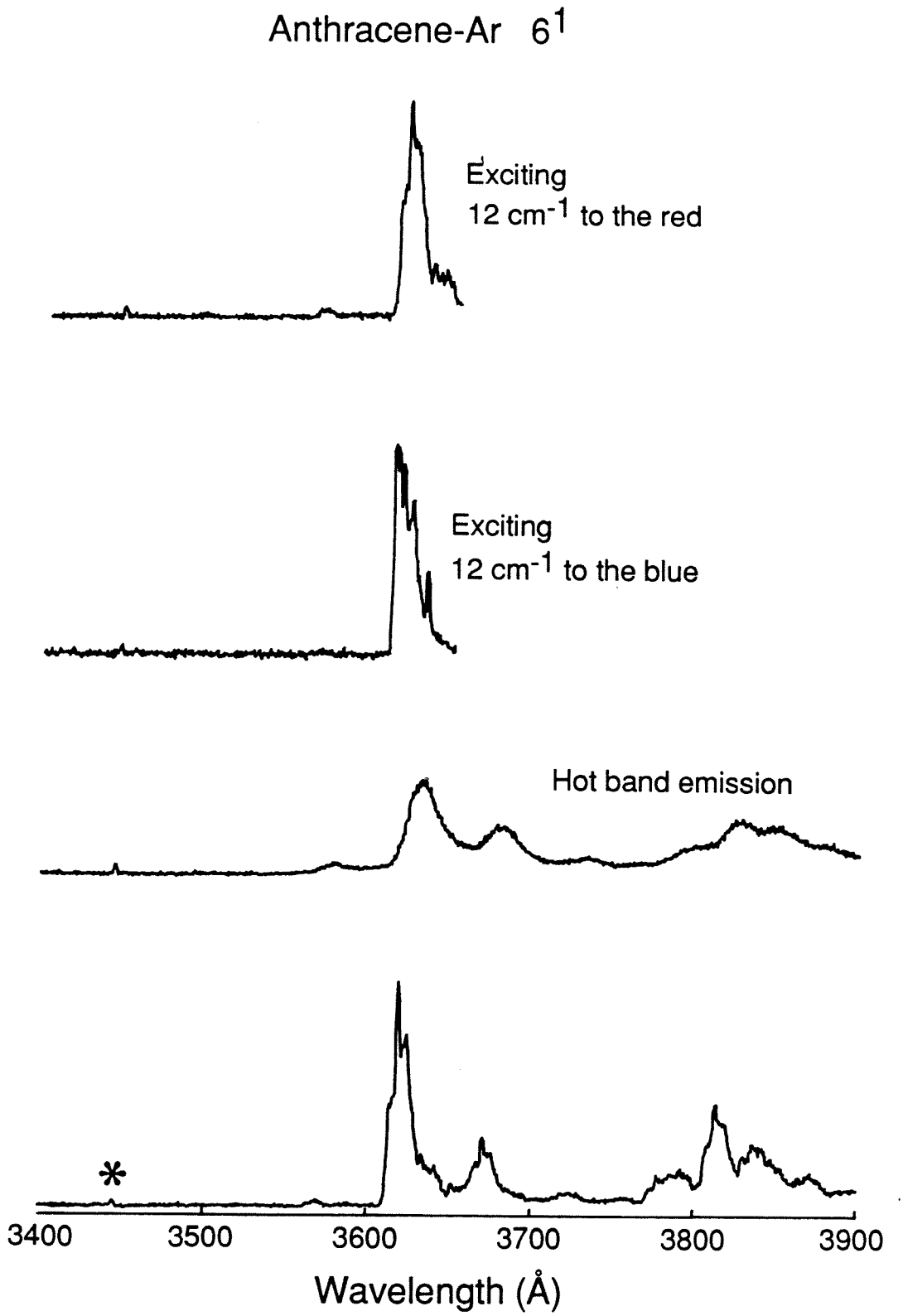
Anthracene-Ar 6^1
Exciting
12 cm^{-1} to the red
Exciting
12 cm^{-1} to the blue
Hot band emission
*
3400
3500
3600
3700
3800
3900
Wavelength (Å)

Figure 15

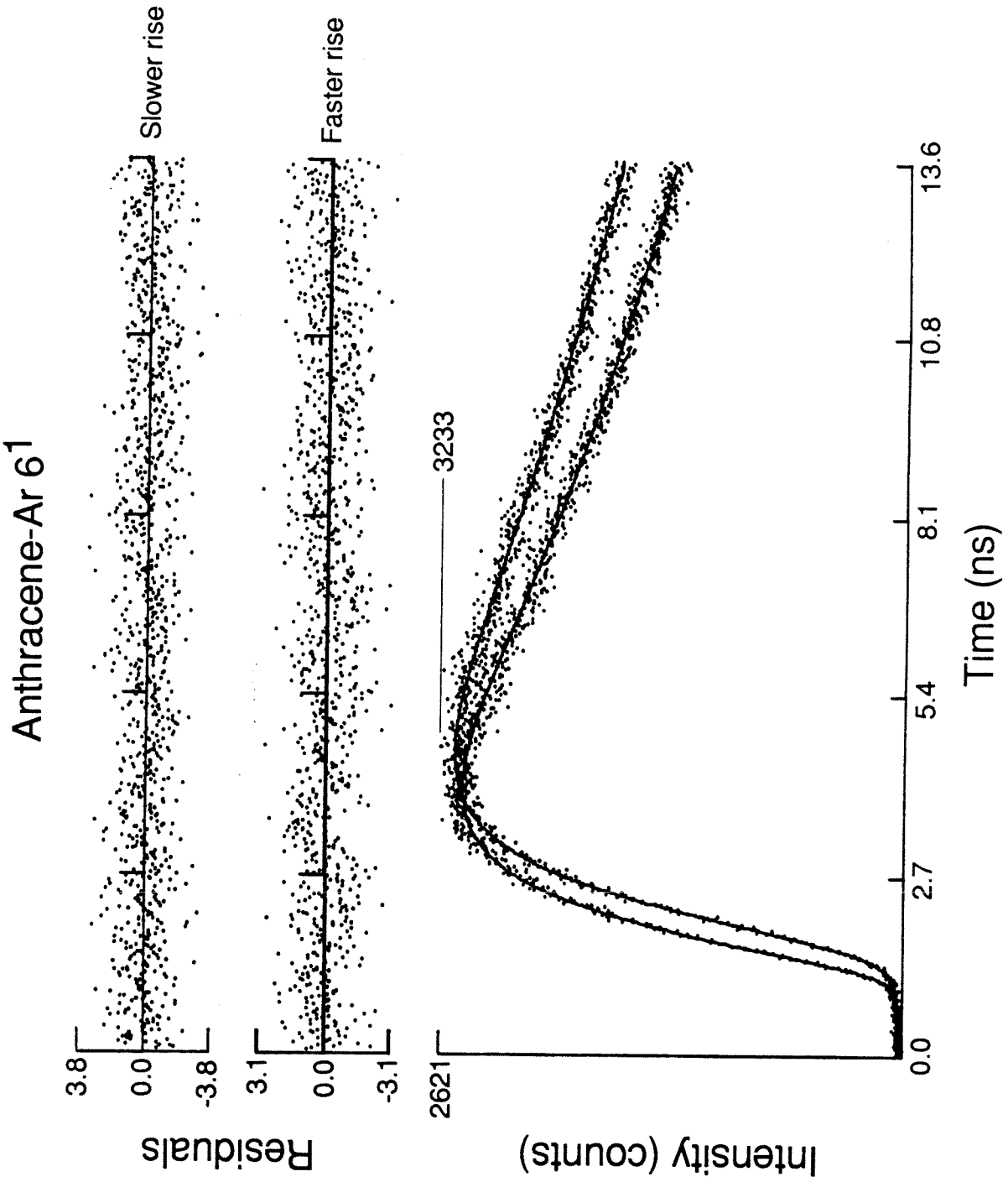
Anthracene-Ar 6[1]
Slower rise
Faster rise
3.8
0.0
-3.8
3.1
0.0
-3.1
Residuals
2621
3233
0.0
2.7
5.4
8.1
10.8
13.6
Intensity (counts)
Time (ns)

Figure 16

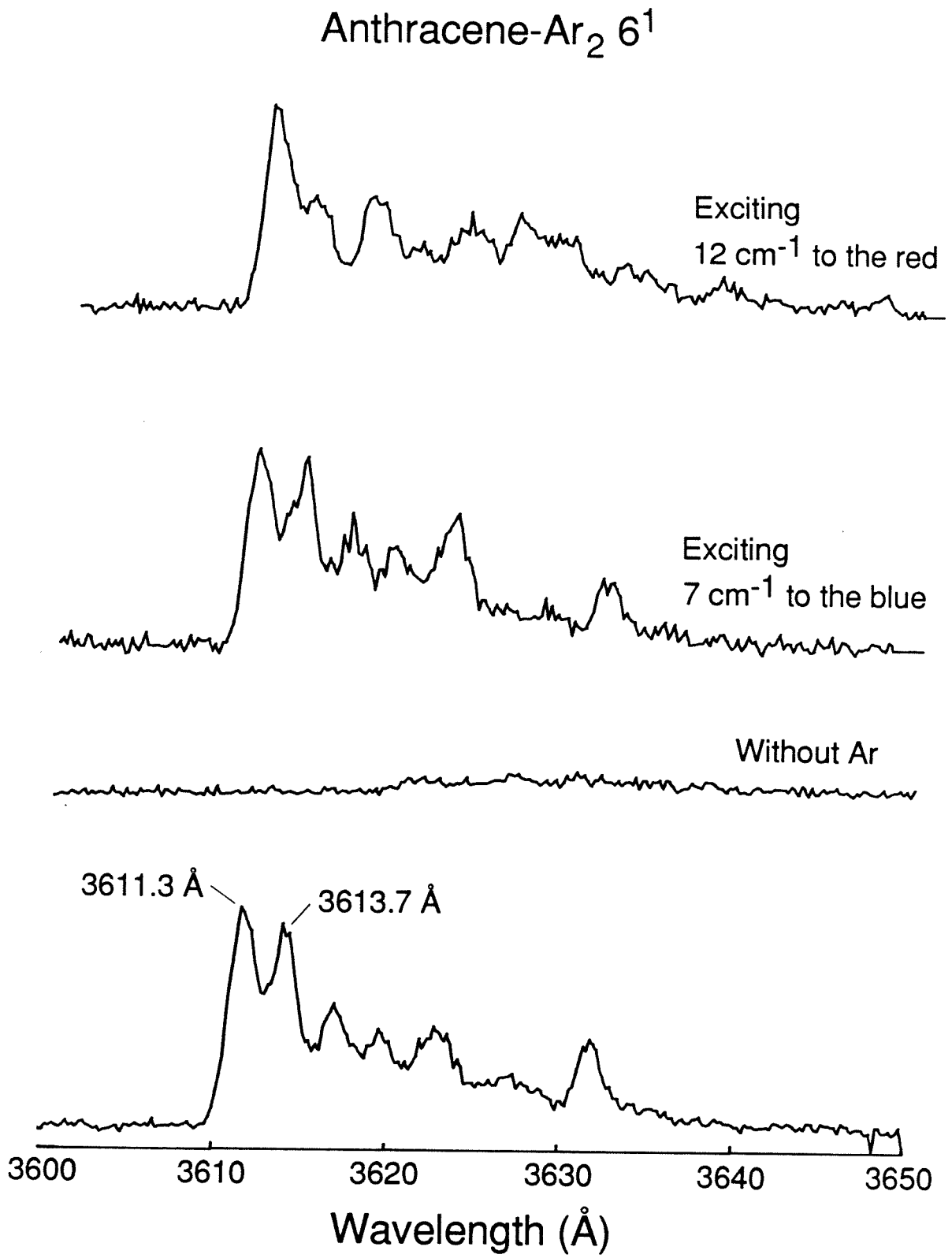
Anthracene-Ar2 6^1
Exciting
12 cm-1 to the red
Exciting
7 cm-1 to the blue
Without Ar
3611.3 Å
3613.7 Å
3600
3610
3620
3630
3640
3650
Wavelength (Å)

Figure 17

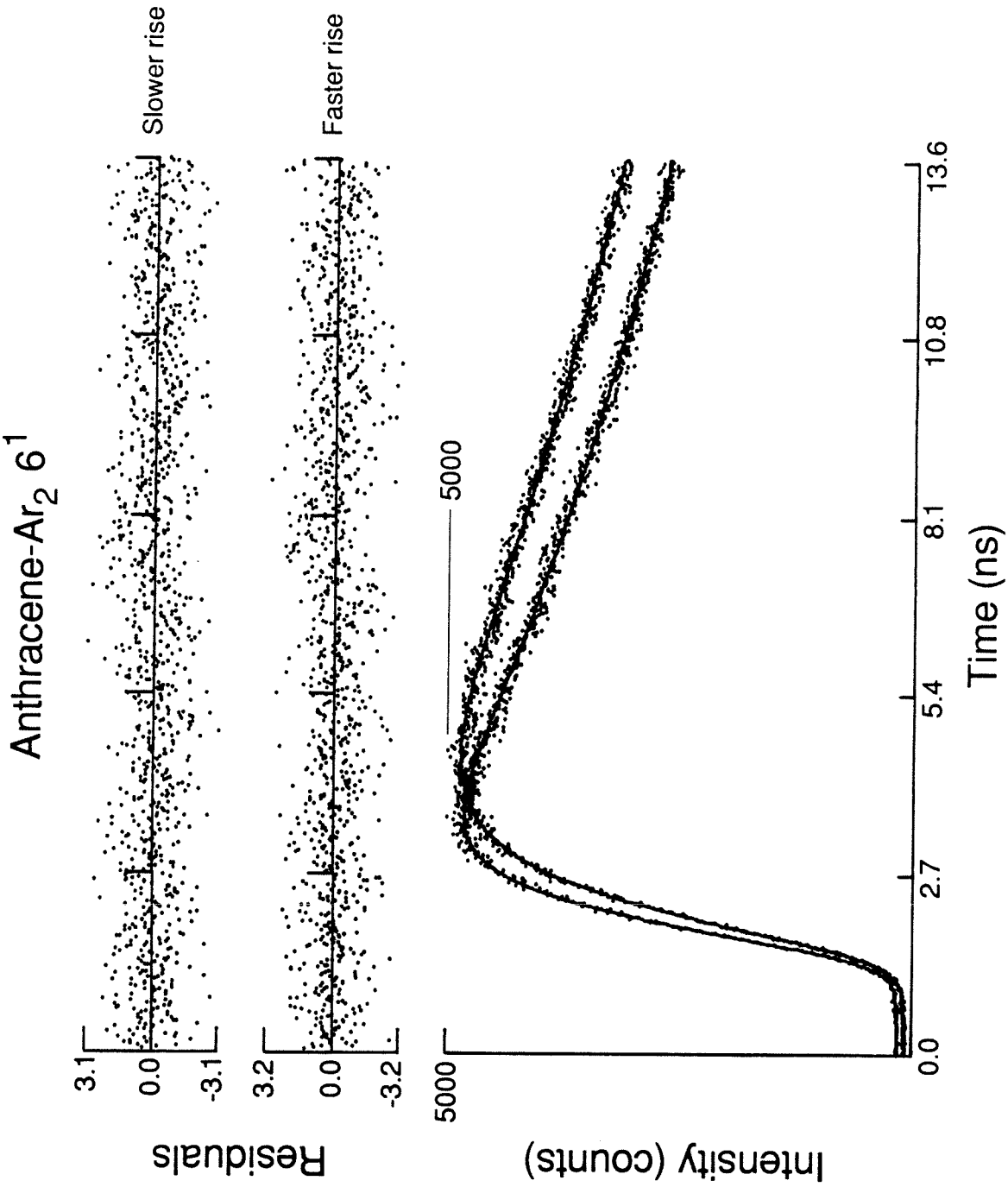
Anthracene-Ar2 6^1
Slower rise
Faster rise
3.1
0.0
-3.1
3.2
0.0
-3.2
Residuals
5000
5000
0.0
2.7
5.4
8.1
10.8
13.6
Time (ns)
Intensity (counts)

Figure 18

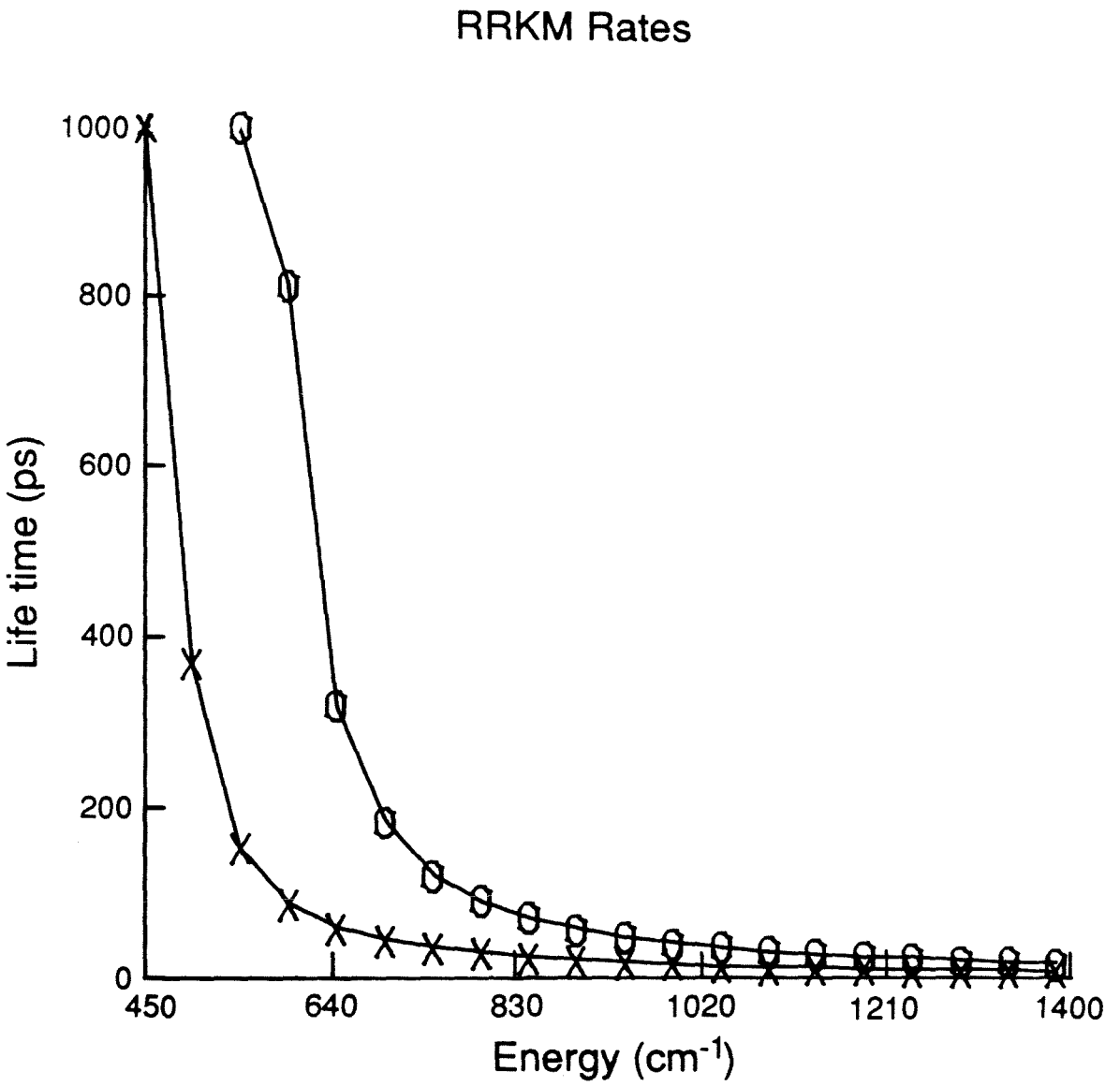
RRKM Rates
Life time (ps)
1000
800
600
400
200
0
450
640
830
1020
1210
1400
Energy (cm-1)

Chapter Six

Conclusions

The data in this thesis show that intramolecular vibrational redistribution to some set of combination levels involving both chemical and van der Waals vibrational modes is an important initial step in the dissociation of the aromatic molecule-rare gas van der Waals complexes studied. The fact that dissipative vibrational redistribution is observed at considerably lower energies than in the bare molecule is understood when the drastic increase in the vibrational state density due to the very anharmonic low frequency van der Waals modes is taken into account.

Products are generally formed with different vibrational predissociation rates which implies that the final product state distribution is determined largely by the redistribution rates to the intermediate states, not by the vibrational predissociation rates. Only a few of the large number of energetically accessible products are actually formed, and those states that are formed have undergone small changes in vibrational quantum numbers from the initially excited state of the complex. This suggests an interesting question not directly addressed in these experiments: How complete is the redistribution and what is the nature of the intermediate states that are reached in the dissociation process? The fact that so few vibrational modes in the products are excited implies that the redistribution is limited to only a few of the energetically accessible chemical modes. The relatively slow vibrational redistribution rates measured in the more rigid and more symmetric anthracene complexes also suggests that the redistribution in those complexes is incomplete, even though it is dissipative.

Some information on the mode selectivity of the intramolecular vibrational redistribution is available from these experiments. In the anthracene complexes, the modes ν_{12}, ν_{10}, and ν_6 were all studied and the redistribution rates were found to increase monotonically with energy. Comparing the redistribution from

the levels 12^2 and 10^1 in anthracene-Ar, levels which differ in energy by only 11 cm^{-1} out of $\sim$760 cm^{-1}, the redistribution rates and the product state distributions are identical.

On the other hand, dramatic differences in both the dissociation rates and the product state distributions are observed comparing the dissociation from different combinations of the modes ν_{25}, ν_{36}, and ν_{37} in stilbene-He. In this case, the "active" modes are out-of-plane bending vibrations and have large components along the van der Waals bond. The data for this complex show that mode-specific, non-statistical dissociation is possible even in such large complexes.

The vibrational predissociation rates observed in the complexes are mode specific. This is apparent from some of the experiments on the stilbene complexes and those on the anthracene complexes at 1380 cm^{-1} where different vibrational predissociation rates are measured for different product vibrational states. Again, information on the identity of the redistributed states from which the different products are formed would be very interesting. Without such information, it is impossible to correlate the measured rates with the vibrational dynamics using, for example, the momentum-gap law.

Large energy gap processes are commonly observed for the dissociation of the stilbene complexes. (Since most of the anthracene product states are not assigned, the energy gap is not known). This and the observation of small changes in the vibrational quantum numbers in the overall dissociation suggests that these changes are more important than the energy gap between the initial and final states. The large energy gaps are probably compensated by the excitation of the van der Waals modes in the intermediate states.

The change in the measured vibrational predissociation rates as a function

of energy is different for complexes of the two different molecules. In the stilbene experiments, rates positively identified as vibrational predissociation rates could not be resolved for any two different energies of the same complex. However, the RRKM rates for the major products of the different complexes are all correct for the energies where rates attributable to vibrational predissociation were resolved, and the RRKM rates also agreed with the fact that no rate was resolvable when the higher energy levels were studied. Thus, the vibrational predissociation rates of the major products are correctly approximated by RRKM and appear to increase rapidly with energy, as predicted by RRKM.

In anthracene complexes, on the other hand, the measured predissociation rates vary erratically with energy and are ~100 times slower than those calculated using the same method that gave agreement with the rates for the stilbene complexes. This suggests that the number of states in the transition state is lower than would be if the dissociation were statistical. In any case, the erratic variation in the predissociation rates with energy shows that the predissociation in these complexes is not completely statistical.

In conclusion, the data in this thesis shows that detailed information on the vibrational dynamics of unimolecular dissociation is available from picosecond studies of the van der Waals complexes in molecular beams. Not only is accurate rate information accessible that is not otherwise available, but information on the actual dissociation pathway is revealed from the analysis of the time-resolved data. The rates measured show interesting examples of both mode-specific and statistical behavior and some correlation of these behaviors with the molecular structure can be made.

Appendix I*

*Published paper:J. S. Baskin, D. Semmes, and A. H . Zewail, J. Chem. Phys. **85**, 7488 (1986).

Coherent photodissociation reactions: Observation by a novel picosecond polarization technique

J. S. Baskin, D. Semmes, and A. H. Zewail
Arthur Amos Noyes Laboratory of Chemical Physics,[a] *California Institute of Technology, Pasadena, California 91125*

(Received 23 September 1986; accepted 10 October 1986)

Photodissociation reactions have been studied by a variety of techniques that probe the initial (reagent) or final (product) state distribution(s) of the reaction.[1] With high-resolution lasers, one is able to obtain the population density[1,2] of a given vibrational(v)–rotational(J) state. With picosecond/femtosecond lasers crossed with molecular beams, state-to-state rates are directly measured.[3] An interesting, and perhaps fundamental, question about the photodissociation process itself is this: Is molecular photodissociation a coherent process? In other words, if instead of exciting one vJ state one prepares a coherent superposition of vJ levels, would this superposition "survive" the dissociation process? Such coherence has not been detected before, perhaps because the laser coherence was not adequate or the pulses

 0021-9606/86/247488-03$02.10

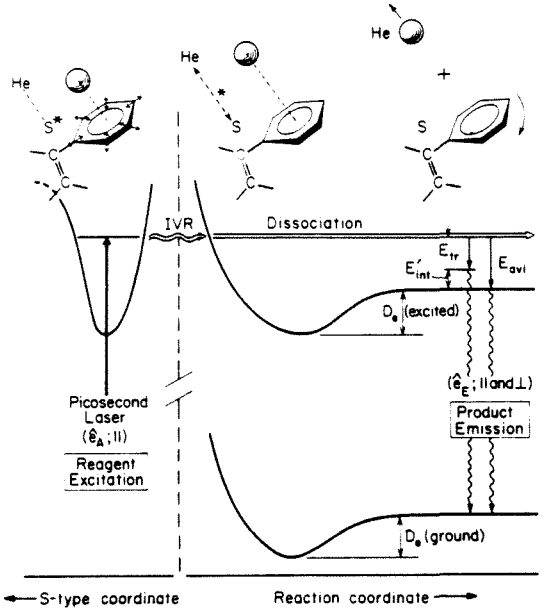

FIG. 1. Potential energy surface description of photodissociation and probing of coherence. $\hat{e}_A$ and $\hat{e}_E$ are the polarization vectors for vdW complex absorption and nascent product emission, respectively. D_e is the binding energy of the complex. The optically-excited stilbene-type mode of the complex is represented on the left-hand side of the figure. Energy reaches the reaction coordinate (right-hand side) via intramolecular vibrational energy redistribution (IVR). After dissociation (far right) the available energy is partitioned between translation (E_{tr}) and internal excitation of stilbene (E'_{int}).

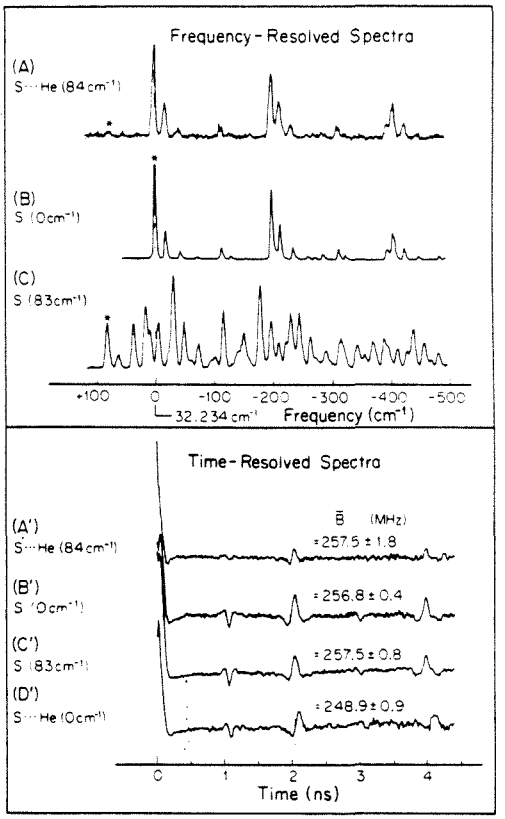

FIG. 2. Time- and frequency-resolved spectra of stilbene and stilbene–helium (1:1) complex. Excitation energies relative to the respective (complex or molecule) 0_0^0 transition energies are given at left. Excitation frequencies are marked by an asterisk in the upper spectra. Spectral resolutions for (A), (B), and (C) are 4, 1, and 5 cm^{-1}, respectively. The difference in resolution accounts for the broadening of (A) relative to (B). The time-resolved data is presented in the form of polarization anisotropies. Temporal resolution was about 60 ps FWHM for all measurements. $\bar{B}$ is $\frac{1}{3}$(B + C) of the complex or parent stilbene. Typical beam conditions are 500 psig for the complex, X/D ~60, and temperature ~150 °C.

used were not short enough in duration.

In this communication, we wish to report on a novel picosecond polarization method for measuring the degree of rotational coherence that is preserved in photodissociation reactions. The systems studied here are jet-cooled van der Waals molecules; stilbene[4–6] bound[5] to He or Ne with a 1:1 composition.[7]

Figure 1 gives the potential energy description of the experiment. A *polarized* picosecond laser-pulse coherently excites the vJ levels of a well-known stilbene-type mode[4] (83, 95, or 198 cm^{-1}) in S_1 of the vdW complex. This creates an initial alignment. By IVR, energy transfers to the reaction coordinate, and the available energy partitions to translation and internal vJ excitation in nascent stilbene. The rising emission of nascent stilbene is then viewed with *parallel* and *perpendicular* polarizations (with respect to the initial pulse polarization). From these experiments, the IVR/photodissociation rates are measured from the decay of the complex and the buildup of the nascent, while the loss of coherence or alignment is determined from the observation of rotational recurrences.[7]

The picosecond/beam apparatus is described elsewhere.[8] To this apparatus we added a polarizer/analyzer system so that the fluorescence can be analyzed prior to dispersion in the spectrometer.

Figure 2 gives the experimental results, frequency- and time-resolved at 83 cm^{-1} excitation. Similar studies were made for 95 and 198 cm^{-1} excitations, and for S·Ne. When exciting S·He at 84 cm^{-1} we observe product(S) emission that entirely mimics the emission of parent S from 0 cm^{-1} (0° level) excitation (spectra A and B), consistent with previous observations.[5] If parent stilbene is excited to 83 cm^{-1}, however, the emission is much different (C spectra) and exhibits resonant bands that have been analyzed in detail before.[4] The available translational energy is therefore > 30 cm^{-1} since we know that the vdW bond energy is 50 cm^{-1} or less.

The time-resolved data are displayed here as anisotropies $r(t)$, i.e., picosecond decays with parallel polarization minus decays with perpendicular polarization. This allows us to monitor the coherence from *recurrence amplitudes* and establish the identity of products from *recurrence spacings* (which directly give the rotational constants of S and S·He).[7] Exciting the complex at 83 cm^{-1} we *observe product stilbene recurrences* as shown by the comparison made in the figure (A', B', C'). These recurrences give precisely the rotational constant of stilbene in the excited state (257.5 ± 1.8

MHz), and conclusively identify the stilbene product.[9] Exciting the complex 0° level, on the other hand, (spectrum D') gives different recurrences characteristic of the S·He (1:1) complex (248.9 ± 0.9 MHz) with the He being on the phenyl ring.[7]

The above results lead to the following important conclusions. The recurrences do survive the dissociation process at all excitation energies studied in the S·He system; *the initial alignment (J coherent excitation) in the complex is preserved in the product.* In this case, we also observe very little (<4 cm^{-1}) rotational excitation in the product, as evidenced by the emission linewidth. For S·Ne, the recurrences have not been observed which indicates that the ensemble-averaged coherence is lost. The recoil velocity in the center-of-mass is $\sim 5\times 10^4$ and $\sim 2\times 10^4$ cm/s for He and Ne systems, respectively. The He leaves stilbene very rapidly and the impulsive force on the benzene ring is relatively small. For Ne, the force is larger and the available energy is channeled[10,11] into more rotations [torque on the stilbene; more tumbling (J) than spinning (K)], as evidenced by the severe broadening (~ 40 cm^{-1}) observed in the emission spectra of produced stilbene.

Theoretical treatments[12] of coherence and mode specificity in these half-collision systems is now very important. The reported picosecond technique probes directly (in real time), these photofragmentation coherences and product state rates, and implications to recoil dynamics is evident.

We have benefited from detailed and enlightening discussions with Professor R. B. Bernstein.

[a] Contribution No. 7477. This work is supported by a grant from the National Science Foundation (DMR-8521191).

[1] For a recent review see: S. Buelow, M. Noble, G. Radhakrishnan, H. Reisler, C. Wittig, and G. Hancock, J. Phys. Chem. **90**, 1015 (1986).

[2] H. W. Cruse, P. J. Dagdigian, and R. N. Zare, Faraday Discuss. Chem. Soc. **55**, 277 (1973).

[3] J. L. Knee, L. R. Khundkar, and A. H. Zewail, J. Chem. Phys. **82**, 4715 (1985); **83**, 1996 (1985); N. F. Scherer, J. L. Knee, D. D. Smith, and A. H. Zewail, J. Phys. Chem. **89**, 5141 (1985).

[4] J. A. Syage, W. R. Lambert, P. M. Felker, A. H. Zewail, and R. M. Hochstrasser, Chem. Phys. Lett. **88**, 266 (1982); J. A. Syage, P. M. Felker, and A. H. Zewail, J. Chem. Phys. **81**, 4685, 4706 (1984); P. M. Felker, W. R. Lambert, and A. H. Zewail, *ibid.* **82**, 3003 (1985); J. Phys. Chem. **89**, 5402 (1985).

[5] T. S. Zwier, E. Carrasquillo, and D. H. Levy, J. Chem. Phys. **78**, 5493 (1983); C. A. Taatjes, W. B. Bosma, and T. S. Zwier, Chem. Phys. Lett. **128**, 127 (1986).

[6] A. Amirav and J. Jortner, Chem. Phys. Lett. **95**, 295 (1983); T. J. Majors, U. Even, and J. Jortner, J. Chem. Phys. **81**, 2330 (1984).

[7] J. S. Baskin, P. M. Felker, and A. H. Zewail, J. Chem. Phys. **84**, 4708 (1986); P. M. Felker, J. S. Baskin, and A. H. Zewail, J. Phys. Chem. **90**, 724 (1986).

[8] W. R. Lambert, P. M. Felker, and A. H. Zewail, J. Chem. Phys. **81**, 2217 (1984); **82**, 2975 (1985).

[9] We have checked for the effect of collisions and bare stilbene absorption underlying the complex absorption. By careful distance and pressure dependence we determined that the complex absorption is definitely better than 95%.

[10] See, e.g., R. Bersohn, J. Phys. Chem. **88**, 5145 (1984); J. P. Simons, *ibid.* **88**, 1287 (1984).

[11] K. W. Butz, D. L. Catlett, G. E. Ewing, D. Krajnovich, and Charles S. Parmenter, J. Phys. Chem. **90**, 3533 (1986); see also the excellent review by G. Ewing, *ibid.* **90**, 1790 (1986).

[12] For a recent review of work by the groups of Freed, Shapiro, Beswick, Jortner, and others, see: R. Schinke, J. Phys. Chem. **90**, 1742 (1986), and Ref. 11.

Appendix II*

*Published paper:Lawrence W. Peng, Brian W. Keelan, David H. Semmes, and Ahmed H . Zewail, J. Chem. Phys. **92**, 5540 (1988).

5540 J. Phys. Chem. 1988, 92, 5540-5549

Dynamics of Intramolecular Vibrational Energy Redistribution in Deuterated Anthracenes: Rotational Band Contour Analysis and Time-Resolved Measurements

Lawrence W. Peng, Brian W. Keelan,† David H. Semmes, and Ahmed H. Zewail*,‡

Arthur Amos Noyes Laboratory of Chemical Physics,§ California Institute of Technology, Pasadena, California 91125 *(Received: February 29, 1988)*

The nature of intramolecular vibrational energy redistribution (IVR) in jet-cooled anthracene-9-d_1 and anthracene-d_{10} has been investigated in both the frequency and time domains. Comparison with anthracene-h_{10} is made, with particular emphasis on the role of vibrational density of states and molecular symmetry. The general regions of IVR (nonexistent, restrictive, and dissipative) have been identified, as in anthracene-h_{10}, in all molecules studied.

I. Introduction

In a recent series of papers published from this laboratory,[1,2] the dynamics of intramolecular vibrational energy redistribution (IVR) was investigated in jet-cooled anthracene-h_{10} and *trans*-stilbene. This was accomplished by spectrally and temporally resolving the fluorescence as a function of excess vibrational energy. From the spectral[2] data for anthracene-h_{10}, it was possible to assign the vibrational symmetries (a_g or b_{1g}) of levels below 1100 cm^{-1} and other higher energy levels. In addition, the distinctiveness of the P-(Q)-R structure of the contours served as a basis for evaluating the spectral purity of levels, i.e., whether a level had major contributions from one (spectrally pure) or more than one (spectrally impure) vibronic state. The temporal data[1] revealed the dynamic nature of the redistribution as a function of excess energy. Single-exponential, quantum beats, and biexponential fluorescence decays have been measured for both anthracene-h_{10} and *trans*-stilbene. The relationship of the decays to the nature of dynamic IVR (nonexistent to restrictive to dis-

† John Simon Guggenheim Foundation Fellow.
‡ Present address: Eastman Kodak Research Laboratories, Rochester, NY 14650.
§ Contribution no. 7743.

(1) (a) Felker, P. M.; Zewail, A. H. *J. Chem. Phys.* **1985**, *82*, 2961; (b) *Ibid.* 2975; (c) *Ibid.* 2994; (d) *Ibid.* 3003.
(2) Keelan, B. W.; Zewail, A. H. *J. Chem. Phys.* **1985**, *82*, 3011; *J. Phys. Chem.* **1985**, *89*, 4939.

0022-3654/88/2092-5540$01.50/0

sipative with increasing vibrational energy) has been discussed in detail.[1,3,4] Single-exponential decays indicate the absence of dynamic IVR in the excited single vibronic level (SVL), while quantum beats are the result of IVR among a few vibrational levels. Biexponential decays indicate dissipative IVR among approximately 10 or more levels.[5]

In an attempt to generalize these findings to deuteriated analogues and to understand the effect of chemical structure on IVR, we have undertaken studies of IVR in partially and fully deuteriated anthracenes. In this paper we will focus on the simplest aspects of molecular symmetry and vibrational-state density. These effects on IVR can potentially be investigated by spectrally and temporally studying the fluorescence as a function of excess vibrational energy in two of anthracene's isotopes: anthracene-9-d_1 (point group symmetry C_{2v}) and anthracene-d_{10} (point group symmetry D_{2h}). The fluorescence excitation spectra, dispersed fluorescence spectra, and temporal data for the three anthracene isotopes are compared. From these data, the vibrational assignments and purity and IVR dynamics are presented. An exhaustive rotational band contour analysis of 65 levels in anthracene-9-d_1 and 71 levels in anthracene-d_{10} is made, and the results are compared with 61 levels in anthracene-h_{10}.

II. Experimental Section

To study the IVR in the two anthracene isotopes, we measured the frequency- and time-resolved fluorescence intensity from many single vibronic levels observed in their excitation spectra. Two sets of laser/supersonic jet apparatus were used for this study. The experimental arrangements are the same as for most of the earlier work done on anthracene-h_{10}.[2,6]

The spectroscopy of the deuteriated anthracenes was obtained by using a Nd:YAG pumped pulsed dye laser system (10 Hz, 5-ns pulse width), with the dye laser output frequency-doubled by a KDP crystal to produce UV light. The dyes used in this study were 25% normal concentration LDS 750 in normal concentration methanolic LDS 698 (lower energies) and normal concentration ethanolic LDS 698 (higher energies). Spectra were taken with the sample temperature held at 443 K with 50 psi of carrier gas (nitrogen or neon) backing pressure. Optimal cooling was achieved at a laser-to-nozzle distance of 10 mm, with the nozzle diameter being 0.5 mm. When the emission was not resolved with the monochromator, it was passed through a UV band-pass filter (Schott UG-11 filter) to remove stray visible light and through a cutoff filter (Schott GG-395 filter) to remove scattered laser light. Pressure tuning was done with nitrogen, which gives a full scan range of 20 cm^{-1} at 360 nm. The pulsed dye laser was frequency-calibrated by using an iron–neon lamp and the optogalvanic method.[7] Vibrational frequencies are reproducible to ± 1 cm^{-1} below 1000 cm^{-1} and ± 2 cm^{-1} above 1000 cm^{-1}.

Temporal data was obtained by using a mode-locked, synchronously pumped, cavity dumped dye laser. The red dye laser output was doubled with a lithium iodate second harmonic generation crystal producing nanojoule pulses in the ultraviolet (UV) region of a 15-ps duration. Dispersed fluorescence spectra were recorded by using a three-plate birefringent filter as a tuning element, which gives a 5-cm^{-1} bandwidth in the UV output. Temporal decays of dispersed fluorescence were recorded with an etalon as an additional tuning element to narrow the laser band width to 2 cm^{-1}. These near-ultraviolet laser beam pulses illuminated molecules in a free jet molecular beam expansion that was produced by expanding 30 psi of helium over the isotope of anthracene in a reservoir held at 438 K (about 5 Torr of vapor pressure) and expanded through a 70-μm pinhole. Fluorescence was dispersed by a $^1/_2$-m monochromator and collected by one of three photomultiplier tubes (PMTs) depending on the relative importance of a short system response time and absolute sensitivity. Dispersed fluorescence spectra were recorded with a 1.6-Å resolution by counting the pulses from an Amperex XP2020Q photomultiplier tube with a multichannel analyzer. Temporal decays of spectrally resolved emission were recorded by using time-correlated single-photon-counting electronics and either a Hamamatsu R1564U or a Hamamatsu R2287U-01 multichannel plate photomultiplier tube. The system response function was measured after each decay by detecting scattered laser light when the molecular beam nozzle was moved into the laser beam and typically had a full width at half maximum (fwhm) of 80 ps. The measured decays were deconvoluted from the system response function and fit to a single exponential, were Fourier analyzed to obtain quantum beat frequencies, or were deconvoluted from the system response function and fit to a double-exponential decay depending on the nature of the decay. Data were stored and analyzed with a PDP 11/23 computer. The monochromator was calibrated by recording the spectrum of a hollow cathode iron–neon lamp under normal experimental conditions.

Anthracene-h_{10} (Aldrich 99.9+%) and anthracene-d_{10} (Aldrich 98+%) were used without further purification. Anthracene-9-d_1 was synthesized from 9-bromoanthracene (Aldrich 98%) by lithiation with *n*-butyllithium followed by hydrolysis in D_2O.[8] Following recrystallization in benzene, the purity of the product was found to be >99% chemically by gas chromatography and >95% isotopically by mass spectrometry (the balance being anthracene-h_{10}). The excitation spectrum of anthracene-9-d_1 showed minor anthracene-h_{10} impurity lines; these were readily identified by absolute frequency and relative intensity.

III. Vibrational-State Densities

A. Anthracene-h_{10}. Vibrational-state densities were calculated between 0 and 2000 cm^{-1} by using the direct-counting computer program reported in the paper by Khundkar et al.[9] Vibrational frequencies for the normal modes of the ground electronic state were taken from the valence field calculations of Cyvin and Cyvin[10] for the in-plane vibrations and from the calculations of Evans and Scully[11] for the out-of-plane vibrational frequencies. The force fields used in these calculations were based on infrared absorption frequencies and a force field transferred from benzene, respectively. All of these calculated frequencies are close to the experimentally determined values[12,13] for both the in-plane and out-of-plane vibrational frequencies.

In the excited state, however, there is a dearth of information on the values of the vibrational frequencies. From spectroscopic experiments on isolated molecules in a molecular beam, 15 vibrational frequencies are known in both the ground and first excited singlet electronic states, all for in-plane modes.[3] Vibrational frequencies have not been calculated for the excited-state force field. The only quantitative indication of how the vibrational frequencies and therefore the density of vibrational states changes for anthracene-h_{10} when it is excited to the first singlet from the ground singlet comes from data on benzene, where there is good agreement between calculated and measured vibrational frequencies for almost all the vibrational modes in the ground and excited electronic states.[14,15]

Our approximate calculations for the vibrational-state densities of the three isotopes in the first excited singlet are based on the

(3) Lambert, W. R.; Felker, P. M.; Zewail, A. H. *J. Chem. Phys.* **1984**, *81*, 2209.
(4) Mukamel, S. *J. Chem. Phys.* **1985**, *82*, 2867.
(5) For a review see: Felker, P. M.; Zewail, A. H. *Adv. Chem. Phys.* **1988**, *70*, 265.
(6) Lambert, W. R.; Felker, P. M.; Zewail, A. H. *J. Chem. Phys.* **1984**, *81*, 2217.
(7) Zalewski, E. F.; Kellar, R. A.; Engleman, Jr., R. *J. Chem. Phys.* **1979**, *70*, 1015, and references therein.
(8) Charlton, J. L.; Agagnier, R. *Can. J. Chem.* **1973**, *51*, 1852.
(9) Khundkar, L. R.; Marcus, R. A.; Zewail, A. H. *J. Phys. Chem.* **1983**, *87*, 2473.
(10) Cyvin, B. N.; Cyvin, S. J. *J. Phys. Chem.* **1969**, *73*, 1430.
(11) Evans, D. J.; Scully, D. B. *Spectrochim. Acta* **1964**, *20*, 891.
(12) Radziszewski, J. G.; Michl, J. *J. Chem. Phys.* **1985**, *82*, 3527. See also: Bree, A. *Chem. Phys. Lett.* **1986**, *131*, 65.
(13) Lambert, W. R.; Felker, P. M.; Zewail, A. H. *J. Chem. Phys.* **1984**, *81*, 2195.
(14) Robey, M. J.; Schlag, E. W. *J. Chem. Phys.* **1977**, *67*, 2775.
(15) Krogh-Jesperson, K.; Rava, R. P.; Goodman, L. *J. Phys. Chem.* **1984**, *88*, 5503.

TABLE I: Approximate Densities at Relevant Energies[a]

	770 cm^{-1}	1420 cm^{-1}	1790 cm^{-1}
S_0, anthracene-h_{10}	1	25	123
S_1, anthracene-h_{10}	6	233	1443
S_1, anthracene-h_{10} (+5%)	4	151	887
S_1, anthracene-h_{10} (−5%)	8	388	2497
S_1, anthracene-d_1	6	257	1609
S_1, anthracene-d_{10}[b]	12	691	5059
S_1, anthracene-d_{10}[c]	15	901	6680

[a] Per wavenumber. [b] Literature. [c] Teller-Redlich rule.

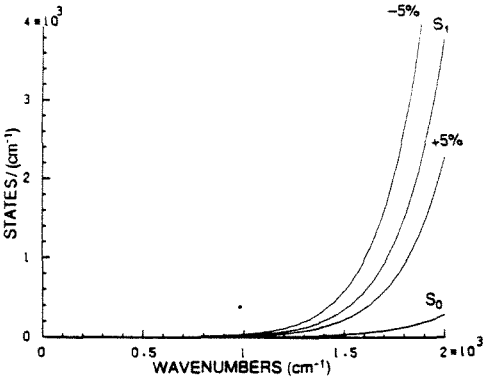

Figure 1. Calculated vibrational density of states versus excess vibrational energy for the S_0 and S_1 electronic states in anthracene-h_{10}.

valence field normal frequencies for the ground singlet.[10,11] The difference between values for S_0 and S_1 are roughly accounted for by considering data for benzene. Benzene's in-plane vibrational frequencies are 4% lower in S_1 than in S_0 on the average (known S_1 anthracene in-plane vibrational frequencies are 6% lower than the average in S_0), and out-of-plane vibrational frequencies are 32% lower on the average. To calculate the vibrational-state density for anthracene in the excited singlet, we therefore made the approximation that the average difference between the in-plane and out-of-plane vibrational frequencies in the ground and first excited singlet of anthracene is the same as the average difference for benzene, 4% for in-plane and 32% for out-of-plane vibrations.

The approximate S_1 vibrational frequencies for anthracene calculated by using this benzene-like approximation were used with the computer algorithm mentioned to directly count the number and density of vibrational levels at various energies of interest. To estimate the uncertainty in this approximation, we repeated the calculation with the out-of-plane frequencies decreased by 5% more and 5% less than the average in benzene. The results are listed in Table I and plotted in Figure 1.

B. State Densities of the Isotopes. A detailed normal-coordinate calculation of the S_0 anthracene-d_{10} frequencies is given in the literature.[10,11] The vibrational density of states (labeled as curve B for anthracene-d_{10} in Figure 2) is then calculated in the same manner as done for anthracene-h_{10}. Curve A for anthracene-d_{10} is an approximate calculation based on the well-known Teller–Redlich rule for isotopic substitution.[16] Similarly, the vibrational frequencies for anthracene-9-d_1 in S_1 were calculated by using the Teller–Redlich rule and the approximate S_1 anthracene-h_{10} frequencies. The Teller–Redlich rule, in the harmonic oscillator limit, relates products of vibrational frequencies for the unsubstituted molecule to those of the substituted molecule for each symmetry species of the lower symmetry point group (only C_{2v} in the case of anthracene-9-d_1). For use of the equation to explicitly calculate the frequencies for the substituted molecule, an approximation must be made relating each of the frequencies in each symmetry class to the anthracene-h_{10} frequencies of that class. Since it is impossible to estimate frequency changes for specific vibrations without a more involved normal-coordinate analysis, it is assumed that all frequencies change by the same factor or, equivalently, that the ratios of vibrational frequencies of the same symmetry species are the same for the two isotopically related molecules.[17] Again, the direct-counting computer algorithm was used to calculate state densities from these vibrational frequencies. The results are listed in Table I and plotted in Figure 2.[18]

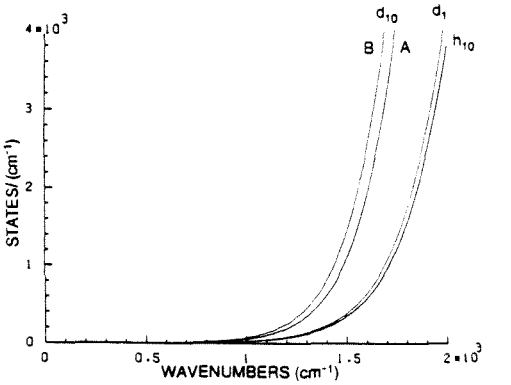

Figure 2. Calculated vibrational density of states versus excess vibrational energy for the S_1 electronic state of the three anthracene analogues.

IV. Results and Discussion

A. Fluorescence Excitation Spectra. Although the power-normalized S_1 fluorescence excitation spectra of anthracene-9-d_1 (point group symmetry C_{2v}) and anthracene-d_{10} (point group symmetry D_{2h}) in supersonic beams have been reported previously,[19] these spectra were not analyzed in any great detail.

The S_1 fluorescence excitation spectra of anthracene-9-d_1 and anthracene-d_{10} are compared with that of anthracene-h_{10} in Figure 3. Each spectrum is plotted against vibrational (excess) energy, i.e., energy above the electronic origin. By obtaining the spectrum of a mixture of all three analogues, we determined the relative positions of the anthracene-9-d_1 and anthracene-d_{10} origins to be 12 and 71 cm^{-1}, respectively, to the blue of the anthracene-h_{10} origin (at 27 695 cm^{-1}).[19] Origin blue-shifts upon deuteriation are expected since excited-state vibrational frequencies are usually lower than ground-state frequencies and so have smaller absolute deuterium (zero-point) shifts.

The vibrational energies (cm^{-1}) and relative intensities (origin = 100%) of the more intense levels in each isotopic species are listed in Table II. The intensities above which the table is complete for each species are as follows: anthracene-h_{10}, 0.05%; anthracene-9-d_1, 0.1%; anthracene-d_{10}, 1%. Analogous levels in the different isotopic species are placed on the same line of the table. The assignments involved many points (and sometimes speculations), and the criteria used for the assignments have been detailed in ref 20.

(16) Wilson, E. B.; Decuis, J. C.; Cross, P. C. *Molecular Vibrations*; Dover: New York, 1955.

(17) A single chemical substitution on a polyatomic molecule generally affects only a few vibrational frequencies (see, for example: Herzberg, G. *Infrared and Raman Spectra of Polyatomic Molecules*; Van Nostrand: Princeton, 1945). Comparing Cyvin and Cyvin's and Evans and Scully's calculated frequencies for anthracene-h_{10} and 9,10-d_2, it is clear that only some of the frequencies are affected by this substitution. More than 70% are within 30 cm^{-1} of their values in anthracene-h_{10} and most of those are within only 5 cm^{-1}. For anthracene-9-d_1, therefore, it was assumed that only the frequencies that change substantially upon 9,10-d_2 substitution are changed by 9-d_1 substitution. The Teller–Redlich rule was used to calculate the remaining 20 frequencies.

(18) Cyvin and Cyvin and Evans and Scully[10,11] also calculated all the normal frequencies for anthracene-d_{10}. The difference in the vibrational-state density calculated by using their vibrational frequencies and the density calculated by using the Teller–Redlich rule and their anthracene-h_{10} frequencies is not too significant although some specific frequencies differ by as much as 20%.

(19) Lambert, W. R.; Felker, P. M.; Syage, J. A.; Zewail, A. H. *J. Chem. Phys.* **1984**, *81*, 2195.

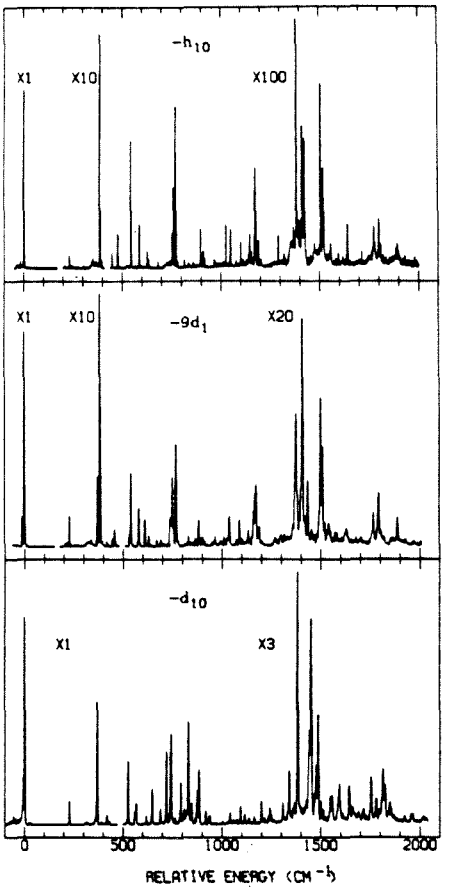

Figure 3. S_1 fluorescence excitation spectra of anthracene-h_{10} (50 psi of neon, 415 K, X/D = 24), anthracene-9-d_1, and anthracene-d_{10} (both 50 psi of nitrogen, 443 K, X/D = 20). Energy references are the electronic origins (anthracene-h_{10} = 27 695 cm^{-1}, anthracene-9-d_1 = 27 707 cm^{-1}, anthracene-d_{10} = 27 766 cm^{-1}). Note that the multiplicative factors for the intensities differ in the three spectra.

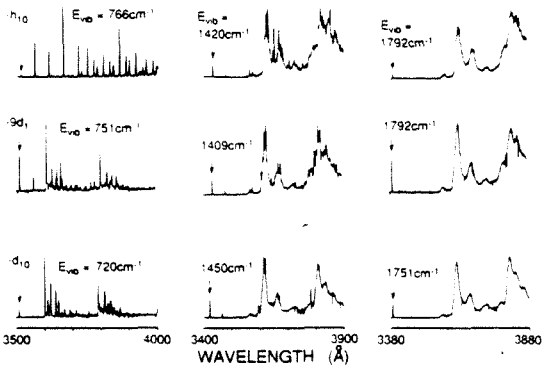

Figure 4. Dispersed fluorescence spectra (anthracene-h_{10}, top; anthracene-9-d_1, middle; anthracene-d_{10}, bottom) taken for selected bands in the excitation spectra of the three anthracene analogues. Resolution is 1.6 Å.

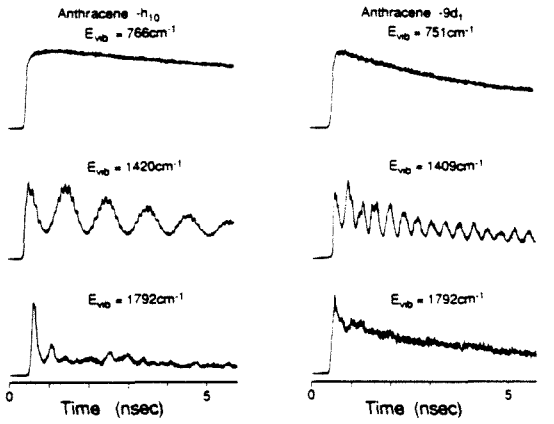

Figure 5. In-phase fluorescence decays (anthracene-h_{10}, left column; anthracene-9-d_1, right column) of the initially excited state for selected bands in the excitation spectra of the three anthracene analogues. All decays are for detection 390 cm^{-1} to the red of the excitation wavelength.

It is shown in section IV.D that the a_g and b_{1g} modes can easily be distinguished by contour shapes. The small number of non-totally symmetric modes simplified the determination of analogous bands and thus provided a check on the isotopic shifts and intensity changes of nearby symmetric levels. Levels of different isotopes were not considered analogous and placed on the same line of Table II unless this assignment was consistent with most or all of the different criteria.

The excitation spectra of these three analogues are qualitatively very similar, but they differ quantitatively in the variation of average intensity with vibrational energy. In anthracene-h_{10}, the intensity of levels drops precipitously with increasing vibrational energy; e.g., the strongest level in the C–C stretching region (1380 cm^{-1}) is only ~1.4% as strong as the origin. The average level intensity drops off less rapidly in anthracene-9-d_1; the strongest C–C stretch at 1409 cm^{-1} is ~5.3% as intense as the origin. In anthracene-d_{10}, average intensity decreases slowly with E_{vib}; the 1382-cm^{-1} C–C stretch is ~40.8% as strong as the origin. The trend is especially clear when one considers the multipliers in Figure 3 (1, 10, 100 in anthracene-h_{10}; 1, 10, 20 in anthracene-9-d_1; 1, 1, 3 in anthracene-d_{10}). In an electronic transition involving little geometry change, most of the intensity is concentrated in the origin. It would thus appear that vibronic activity plays an important role.[14,15]

One other difference was noted in the excitation behavior of the three analogues: while anthracene-h_{10} was efficiently vibrationally cooled by neon carrier gas (the spectrum in Figure 3 was obtained with 50 psi of neon), anthracene-9-d_1 and anthracene-d_{10} showed slight and severe apparent sequence congestion, respectively, in neon. Both deuteriated anthracenes cooled well with 50 psi of nitrogen (see Figure 3). The origin of this difference in cooling behavior between the isotopic analogues is not clear.

B. Dispersed Fluorescence Spectra. The dispersed fluorescence spectra of some of the SVLs investigated are presented in Figure 4 for anthracene-h_{10} and for the two deuteriated isotopes studied. As was observed in the earlier studies of anthracene-h_{10}, the spectra from the deuteriated isotopes fall in three general categories of description: (1) Assignable, sharp spectra are observed at "low" excitation energies. (2) Slightly broadened spectra that still have some sharp, resolvable structure are observed at "intermediate" excitation energies. Some of this sharp structure is assignable as originating from the initially excited level and some is not. (3) Broad, unresolvable spectra with very little resonance fluorescence is observed at "high" excitation energies. It must be noted, however, that there is not necessarily a clear division between the three types of behavior. Additionally, as discussed before,[1,2] spectral congestion is not a direct measure of the nature of the dynamic IVR.[5]

Table III has explicit spectral assignments for the bands observed in the fluorescence from the levels at S_1 +751 cm^{-1} and S_1 +1409 cm^{-1} in anthracene-9-d_1, exemplifying how the bands in the spectra from the different energy regions can be assigned.

C. Temporal Behavior. The temporal behavior of both "relaxed" (where possible) and "unrelaxed" fluorescence bands

TABLE II: Comparison of S_1 Vibrational Levels in Anthracene-h_{10}, -9-d_1, and -d_{10}

anthracene-h_{10}			anthracene-9-d_1			anthracene-d_{10}		
energy[a]	int[b]	assgnt[c]	energy	int	sym[d]	energy	int	sym
0	100.00	0_0^0	0	100.0	a_g	0	100.0	a_g
209	0.17	a_g	210	0.1	a_g			
232	0.74	11_0^1	231	1.4	b_{1g}	229	11.2	b_{1g}
385	13.51	12_0^1	385	11.8	a_g^+	370	58.9	a_g
390	0.45	2 × 209?	396	0.2	e			
						392	1.1	b_{1g}
			421	0.2	a_g			
444	0.08	a_g	449	0.3	a_g	430	1.6	a_g
473	0.19	a_g	460	0.7	a_g	418	4.5	a_g
541	0.71	11_0^2	542	1.6	a_g	525	10.2	a_g
583	0.24	11_0^1	583	0.8	a_g	567	3.5	a_g
623	0.06	a_g	614	0.6	a_g	561	2.1	a_g
630	0.05	b_{1g}	634	0.2	b_{1g}	619	1.4	b_{1g}
678	0.03	a_g	673	0.1	a_g	649	5.7	a_g
			694	0.1	a_g			
748	0.19	a_g	742	0.5	a_g	690	2.6	a_g
755	0.45	$10_0^1, a_g$	751	1.5	a_g	720	11.8	a_g
766	0.91	12_0^2	769	2.3	a_g	743	14.5	a_g
775	0.04	a_g	778	0.1	a_g			
			832	0.2	$2a_g$			
		418 + 370				788	1.7	a_g
889	0.22	9_0^1	880	0.5	b_{1g}	791	6.7	$2b_{1g}$
895	0.08	b_{1g}	864	0.2	b_{1g}	764	1.1	b_{1g}
			884	0.5	b_{1g}			
905	0.09	a_g	899	0.1	+	804	1.7	a_g
910	0.05	a_g	904	0.2	a_g	809	2.4	a_g
			913	0.1	a_g			
			948	0.1	a_g?	917	2.1	a_g
961	0.04	a_g	959	0.1	a_g	928	0.7	e
966	0.03	a_g	966	0.2	a_g	937	1.5	+
			995	0.1	a_g^+			
1019	0.24	9_0^1	1012	0.2	a_g			
			1028	0.1	a_g			
1042	0.21	a_g	1037	0.6	a_g	829	16.5	a_g
			1073	0.1	$3b_{1g}$			
1094	0.14	a_g	1089	0.5	a_g	845	3.4	+
			1101	0.1	b_{1g}^+			
1142	0.07	$10_0^1 12_0^1$	1135	0.3	+	1092	2.9	a_g
1146	0.19	12_0^3				1114	1.6	a_g
1158	0.08	a_g						
			1160	0.7	b_{1g}	864	1.0	b_{1g}
1168	0.56	$7_0^1 8_0^1$	1167	1.1	a_g	874	5.4	a_g
			1173	1.3	+	882	8.8	a_g
			1183	0.3	+			
1184	0.15	7_0^1	1189	0.4	b_{1g}^+			
			1269	0.1	+			
			1278	0.1	+			
			1297	0.2	+			
			1304	0.2	a_g			
			1319	0.2	a_g			
1291	0.19	a_g						
						1039	1.9	a_g
						1136	1.0	+
						1162	1.2	+
		829 + 370				1197	3.8	a_g
						1235	1.5	a_g
						1307	3.5	a_g
						1339	8.6	+
						1359	1.7	a_g
						1364	3.5	+
1380	1.39	$6_0^1, a_g$	1375	3.0	a_g^+	1382	40.8	a_g
1389	0.27	a_g						
1409	0.80	$2a_g$?	1409	5.3	a_g	1450	33.2	a_g^+
1414	0.13	+	1418	0.3	+	1419	2.4	a_g
1418	0.35	+				1425	2.4	a_g^+
1420	0.73	5_0^1	1435	1.5	a_g	1440	15.2	+
			1454	0.3	a_g^+			

TABLE II (Continued)

anthracene-h_{10}			anthracene-9-d_1			anthracene-d_{10}		
energy[a]	int[b]	assgnt[c]	energy	int	sym[d]	energy	int	sym
1469	0.09	1094 + 385	1469	0.2	+	1215	1.1	+
			1480	0.2	$2b_{1g}$	1465	2.5	b_{1g}?
1501	1.03	4_0^1	1499	3.4	a_g^+	1484	17.7	+
1506	0.20	b_{1g}						
1508	0.24	b_{1g}						
1514	0.56	$\bar{4}_0^{1+}$	1509	2.2	+	1475	9.6	+
1516	0.24	b_{1g}	1520	0.3	b_{1g}	1497	3.9	b_{1g}^+
1543	0.06	+	1532	0.2	+			
1545	0.08	+	1540	0.5	+	1510	2.5	+
1548	0.09	a_g						
1550	0.14	$7/8_0^1 12_0^1$	1550	0.2	+	1241	2.7	a_g
						1249	1.6	a_g
1577	0.06	*e*	1573	0.3	+	1546	4.6	a_g
1590	0.07	*e*	1582	0.3	a_g^+	1554	4.8	+
1635	0.25	a_g^+	1629	0.4	+	1592	6.5	a_g^+
1640	0.09	+				1587	3.7	a_g
						1608	1.9	a_g^+
1715	0.07	*e*	1705	0.1	+	1641	6.3	a_g^+
		2 × 829				1658	2.8	a_g^+
		1307 + 370				1679	1.0	a_g
						1690	2.0	a_g^+
		1339 + 370				1712	2.5	+
		1359 + 370				1729	1.4	+
1767	0.23	$6_0^1 12_0^1$	1765	0.7	+	1751	7.6	+
1771	0.11	+						
1773	0.13	1389 + 385						
						1778	4.2	+
1792	0.28	1409 + 385	1792	1.2	+	1811	8.9	+
1795	0.05	1414 + 385	1803	0.1	*e*	1793	1.1	+
1798	0.05	1418 + 385						
1801	0.14	$5_0^1 12_0^1$	1820	0.1	*e*	1821	6.4	+
1883	0.04	+						
1885	0.12	$4_0^1 12_0^1$	1886	0.6	+	1852	3.6	+
1890	0.04	1506 + 385						
1895	0.04	$\bar{4}_0^1 12_0^1$				1846	3.6	+
1897	0.04	1516 + 385				1866	0.6	*e*
			1926	0.1	*e*	1920	1.5	+
						1952	1.7	+
		1592 + 370				1961	1.7	+

[a] Vibrational energy in cm^{-1}. The -h_{10} data are primarily from ref 2 and 13. The -h_{10} origin is 27 695 cm^{-1} (from ref 13), in this study the -9-d_1 and -d_{10} origins were found to be shifted 12 and 71 cm^{-1}, respectively, to higher energy. [b] Percent intensity relative to the origin of each molecule (100%), which is the most intense transition in each molecule. The -h_{10} data are primarily from ref 2 and 13. [c] A_n^m denotes the transition of mode number *A* from *n* quanta in the ground electronic state to *m* quanta in the excited state S_1, combination bands are $A_n^m B_j^l$ ... A bar over a mode number indicates a non-totally symmetric (e.g., b_{1g}) vibration. Where mode numbers have not been assigned in ref 13, combination bands are denoted by *a* + *b*, where *a* and *b* are the -h_{10} vibrational frequencies in cm^{-1} (in a few cases, combination bands in -d_{10} have no observed -h_{10} analogue; the -d_{10} frequencies are then given in this column). For levels not assigned in ref 13, vibrational symmetries from ref 2 are given (see note *d* for designations; superpositions of levels are also denoted with a comma, e.g., $10_0^1, a_g$ indicates that mode number 10 and another a_g vibration overlap). [d] Vibrational symmetries found in this study from rotational band contour analysis. Superpositions of levels are denoted variously, e.g., $2a_g$ (two a_g vibrations overlap), a_g^+ (one or more vibrations of indeterminate symmetry overlap with an a_g vibration), or just + (two or more vibrations of indeterminate symmetry overlap). *e* indicates that no symmetry analysis has been performed for this level.

was recorded from the same SVLs as in Figure 4, and some are presented in Figure 5 for anthracene-h_{10} and anthracene-9-d_1. Similar results (not shown) were obtained for anthracene-d_{10}. The difference between the single-exponential decays (convoluted with the system response function), the beating decays, and the double-exponential decays of the fluorescence is clear.

The anthracene-h_{10} data in this section have previously been published and are repeated here for the purpose of comparing it with data from the deuteriated isotopes.

D. Rotational Band Contour Analysis: Medium Resolution. At lower vibrational energies (<1100 cm^{-1}) in both deuteriated anthracenes, nearly all of the rotational band contours conformed to one of two distinct types. The much commoner contour type, exemplified by the electronic origins, exhibited well-separated P and R branches, but no Q branch, and had fwhm near 3.2 cm^{-1}. The rarer contour type (e.g., at 231 cm^{-1} in anthracene-9-d_1) showed a sharp Q branch and was narrower than the prevalent contour type (fwhm of 2.5 cm^{-1}). This situation is identical with that found in anthracene-h_{10} (prevalent contour type, fwhm of 4.0 cm^{-1}; rarer contour type, fwhm of 2.3 cm^{-1}).[2] The two types of contours of each of the three isotopic species are compared in Figure 6 (commoner labeled a_g, rarer labeled b_{1g}); the similarity of each contour type for the different analogues is evident. In the previous anthracene-h_{10} study, the prevalent contour type was associated with symmetric (a_g) vibrations, while the rarer type was due to antisymmetric (b_{1g}) vibrations. Although the same conclusion can be reached for the deuteriated compounds strictly by analogy, the arguments of the previous study, suitably modified, are given below.

Assuming anthracene to be planar, anthracene-d_{10} belongs to the point group D_{2h}. The similarity of the contours of anthracene-9-d_1 suggests that it is reasonable to use D_{2h} nomenclature to describe this species, despite the fact that it belongs to point group C_{2v}. We shall follow this convention in this paper so that

TABLE II: Comparison of S_1 Vibrational Levels in Anthracene-h_{10}, -9-d_1, and -d_{10}

anthracene-h_{10}			anthracene-9-d_1			anthracene-d_{10}		
energy[a]	int[b]	assgnt[c]	energy	int	sym[d]	energy	int	sym
0	100.00	0_0^0	0	100.0	a_g	0	100.0	a_g
209	0.17	$\underline{a_g}$	210	0.1	a_g			
232	0.74	$\overline{11}_0^1$	231	1.4	b_{1g}	229	11.2	b_{1g}
385	13.51	12_0^1	385	11.8	a_g^+	370	58.9	a_g
390	0.45	2 × 209?	396	0.2	e			
						392	1.1	b_{1g}
			421	0.2	a_g			
444	0.08	a_g	449	0.3	a_g	430	1.6	a_g
473	0.19	$\underline{a_g}$	460	0.7	a_g	418	4.5	a_g
541	0.71	$\overline{11}_0^2$	542	1.6	a_g	525	10.2	a_g
583	0.24	11_0^1	583	0.8	a_g	567	3.5	a_g
623	0.06	a_g	614	0.6	a_g	561	2.1	a_g
630	0.05	b_{1g}	634	0.2	b_{1g}	619	1.4	b_{1g}
678	0.03	a_g	673	0.1	a_g	649	5.7	a_g
			694	0.1	a_g			
748	0.19	a_g	742	0.5	a_g	690	2.6	a_g
755	0.45	$10_0^1,a_g$	751	1.5	a_g	720	11.8	a_g
766	0.91	12_0^2	769	2.3	a_g	743	14.5	a_g
775	0.04	a_g	778	0.1	a_g			
			832	0.2	$2a_g$			
		418 + 370				788	1.7	a_g
889	0.22	9_0^1	880	0.5	b_{1g}	791	6.7	$2b_{1g}$
895	0.08	b_{1g}	864	0.2	b_{1g}	764	1.1	b_{1g}
			884	0.5	b_{1g}			
905	0.09	a_g	899	0.1	+	804	1.7	a_g
910	0.05	a_g	904	0.2	a_g	809	2.4	a_g
			913	0.1	a_g			
			948	0.1	a_g?	917	2.1	a_g
961	0.04	a_g	959	0.1	a_g	928	0.7	e
966	0.03	a_g	966	0.2	a_g	937	1.5	+
			995	0.1	a_g^+			
1019	0.24	9_0^1	1012	0.2	a_g			
			1028	0.1	a_g			
1042	0.21	a_g	1037	0.6	a_g	829	16.5	a_g
			1073	0.1	$3b_{1g}$			
1094	0.14	a_g	1089	0.5	a_g	845	3.4	+
			1101	0.1	b_{1g}^+	-		
1142	0.07	$10_0^1 12_0^1$	1135	0.3	+	1092	2.9	a_g
1146	0.19	12_0^3				1114	1.6	a_g
1158	0.08	a_g						
			1160	0.7	b_{1g}	864	1.0	b_{1g}
1168	0.56	$7_0^1,8_0^1$	1167	1.1	a_g	874	5.4	a_g
			1173	1.3	+	882	8.8	a_g
			1183	0.3	+			
1184	0.15	7_0^1	1189	0.4	b_{1g}^+			
			1269	0.1	+			
			1278	0.1	+			
			1297	0.2	+			
			1304	0.2	a_g			
			1319	0.2	a_g			
1291	0.19	a_g						
						1039	1.9	a_g
						1136	1.0	+
						1162	1.2	+
		829 + 370				1197	3.8	a_g
						1235	1.5	a_g
						1307	3.5	a_g
						1339	8.6	+
						1359	1.7	a_g
						1364	3.5	+
1380	1.39	$6_0^1,a_g$	1375	3.0	a_g^+	1382	40.8	a_g
1389	0.27	a_g						
1409	0.80	$2a_g$?	1409	5.3	a_g	1450	33.2	a_g^+
1414	0.13	+	1418	0.3	+	1419	2.4	a_g
1418	0.35	+				1425	2.4	a_g^+
1420	0.73	5_0^1	1435	1.5	a_g	1440	15.2	+
			1454	0.3	a_g^+			

branch much more intense than the P branch, in having a greater fwhm, and in having a wider, deeper P–R branch gap. The coupling mechanism in this case could involve Coriolis interactions or special anharmonic forces, as discussed by us[1,5,6] and by Amirav.[25]

In anthracene-9-d_1, the S_1 + 1409 cm^{-1} level is suitable for a similar study, since (1) it is an intense, spectrally pure level, exhibiting distinct P–R structure, and (2) two types of quantum beat modulations (in-phase and out-of-phase) are observed in the fluorescence decays under certain detection conditions. Specifically, detection of emission to S_0 + 390 cm^{-1} yields in-phase quantum beats due to emission from a state that is initially populated by the laser pulse (as in the case of the previously discussed anthracene-h_{10} quantum beats). In contrast, detection of emission from a state populated indirectly through coupling to a laser-populated state, e.g., emission to S_0 + 1499 cm^{-1}, yields out-of-phase quantum beats. These two types of quantum beats differ in phase by 180°, since the population oscillates between the states producing the two types of modulation. Total detection of emission (i.e., detection of all emission except that absorbed by a laser cutoff filter) yields a typical single-exponential decay with no (or very weak) quantum beat modulations.

The frequency analogues of these temporal experiments are depicted in Figure 10. The resolved emission (=dispersed fluorescence) spectrum is shown in the upper half of the figure, trace A. The rotational band contour obtained with total detection is shown in trace B in the lower half of the figure. Detection of emission to the range S_0 + 390 (±100) cm^{-1}, shown by the interval labeled 1 in trace A, yields the contour in trace C, corresponding to in-phase quantum beats. Contour D, corresponding to out-of-phase quantum beats, was obtained through detection of interval 2 in trace A (S_0 + 1499 (±25) cm^{-1}). These three contours are somewhat similar in appearance, the differences being within the range of experimental uncertainty (as judged by spectral reproducibility). Certainly there are no dramatic differences in contour shapes as in anthracene-h_{10} S_1 + 1380 cm^{-1}. It would therefore appear that anharmonic coupling is responsible for the quantum beats in this system, consistent with the dominant extent of anharmonic coupling in S_1 anthracene-h_{10}.[1,5,6] However, we cannot rule out completely the presence of some Coriolis interactions.[5,6,25] It is important to note that even though the spectra are similar, the time-resolved data reflect entirely distinct IVR dynamics.[5]

G. Temporal Behavior. The fact that anthracene-h_{10} excited to S_1 + 1420 cm^{-1} exhibits restrictive IVR among four levels while dissipative IVR involving approximately 20 levels is observed at 1792 cm^{-1} has been justified qualitatively by a calculation of the vibrational density of states for the *ground* singlet electronic state: the density at 1792 cm^{-1} is 5 times the density at 1420 cm^{-1}, which could account for the observation of 5 times the number of coupled levels.[1b]

More information is necessary, however, to account for the redistribution more quantitatively. This is apparent when one notes that the actual number of observed coupled levels in anthracene-h_{10} is larger than the calculated ground-state density would suggest. For example, in the excitation of anthracene-h_{10} to S_1 + 1420 cm^{-1}, the molecular symmetry of the observed four coupled levels must be the same if the coupling is anharmonic. Since there are eight symmetry species for D_{2h} anthracene, there must be 32 levels in the energy region that is under investigation. Although our laser bandwidth is 2 cm^{-1}, we can detect beat frequencies only in our temporal measurements of <10 GHz. This reasoning leads to a total density of 96 states/cm^{-1} for anthracene-h_{10}, which is far different from the ground-state calculation of 25 states/cm^{-1}. The state density we calculated for S_1 agrees more closely with the number of experimentally observed coupled levels but is higher than the observed state density (see Table I). At 1420 cm^{-1} the calculated density of a_g states in S_1 is about twice that observed; at 1792 cm^{-1} it is about 4 times that observed (the number of observed coupled levels at 1792 cm^{-1} is a lower limit calculated from the ratio of the amplitudes of the fast and slow components in the biexponential decay of the unrelaxed fluorescence). This comparison of observed and calculated vibrational-state densities suggests that the number of levels observed to participate in the IVR dynamics in anthracene-h_{10} is approximately equal, within a factor of 2, to the number of levels of the proper symmetry to be anharmonically coupled and that are studied experimentally (i.e., prepared coherently and resolved temporally).

TABLE IV[a]

	ρ	$E(-h_{10})$	$E(-9\text{-}d_1)$	$E(-d_{10})$
no IVR	61	1170	1030	960
restricted IVR	120–700	1290–1640	1160–1480	1080–1380
dissipative IVR	1500	1800	1670	1530

[a] The densities are per wavenumber, and the energies are in wavenumbers.

Overall, the observed IVR in anthracene-9-d_1 is similar to the observed IVR in anthracene-h_{10}. There are, however, exceptions. The level at S_1 + 1173 cm^{-1} in anthracene-9-d_1 is involved in restricted redistribution while a level at very nearly the same excess vibrational energy in anthracene-h_{10} (S_1 + 1168 cm^{-1}) undergoes no dynamic IVR. This difference in the IVR in anthracene-9-d_1 compared to anthracene-h_{10} can be understood in terms of the effects of symmetry reduction by monodeuteriation as discussed in the Introduction. By comparing the IVR in anthracene-h_{10} with the IVR in anthracene-9-d_1 that occurs at the energy where the calculated state densities are the same, one is able to compare IVR in the two molecules. This method would circumvent the major uncertainty in all the S_1 vibrational-state density calculations: the uncertainty in all the S_1 vibrational frequencies compared to those of S_0. For example, no IVR is observed when anthracene-h_{10} is excited to S_1 + 1168 cm^{-1} or less (within our time resolution). The calculated vibrational-state density for anthracene-h_{10} at 1168 cm^{-1} in S_1 is 61 cm^{-1}. From Figure 2, anthracene-9-d_1 and anthracene-h_{10} have nearly the same total state densities at this energy. If, however, anthracene-9-d_1 is effectively C_{2v} rather than D_{2h}, the density of totally symmetric modes is $^{61}/_4$ per cm^{-1} instead of $^{61}/_8$ per cm^{-1}. Therefore, if the IVR is statistical, then no IVR is expected in anthracene-9-d_1 below 1030 cm^{-1} (where the density of totally symmetric modes is equal to that of anthracene-h_{10} at 1168 cm^{-1}). Listed in Table IV are the calculated vibrational-state densities for the energies where no, restricted, and dissipative IVR were observed in anthracene-h_{10}. Also listed are the energies where these vibrational-state densities occur in the deuteriated isotopes. This table indicates, therefore, how the redistribution might be expected to change because of isotopic substitution.

The experimental observation of restricted IVR at S_1 + 1173 cm^{-1} in anthracene-9-d_1 is in accord with these predictions. At this vibrational-state density beats are seen in the fluorescence decay of D_{2h} anthracene-h_{10} and in the fluorescence decay of C_{2v} anthracene-9-d_1. The energies where IVR is first observed in the two molecules, however, are different. Similar results regarding the different regions of IVR were also found in anthracene-d_{10}.

V. Conclusions

The highly analogous rovibronic nature of the three anthracene isotopes can be seen from the spectroscopic data. The data clearly show the similarity of the excitation spectra and rotational band contour shapes, as well as the correlation of the observed vibrational levels. Qualitatively, we can relate the comparative dynamics of IVR to the relative state density and symmetry of the molecule. But the most important finding here is that the regions of IVR identified previously for anthracene-h_{10} and *trans*-stilbene (nonexistent, restrictive, and dissipative IVR)[1,5] have also been found in all deuteriated anthracenes studied here. These regions of IVR have also recently been observed in azulene by Wallace and co-workers.[26] Both spectral and temporal studies of these

(25) Amirav, A. *J. Chem. Phys.* **1987**, *86*, 4706.

(26) Demmer, D. R.; Hager, J. W.; Leach, G. W.; Wallace, S. C. *Chem. Phys. Lett.* **1987**, *136*, 329.

molecules confirm this picture. It seems that this "division" of IVR regions in large molecules is general.

Acknowledgment. We gratefully acknowledge funding of this work by the National Science Foundation. When we started this work several years ago, Professor E. Lee was very helpful in teaching us the details of the computer program for the rotational contours. This article is dedicated, in memory of a great colleague and scholar, to Professor Ed Lee.

Registry No. Anthracene-9-d_1, 4485-03-4; anthracene-d_{10}, 1719-06-8; anthracene-h_{10}, 120-12-7.